Geotechnical Aspects of Offshore Wind Turbine Dynamics Emerging from 3D Sand-Monopile Non-Linear Simulations

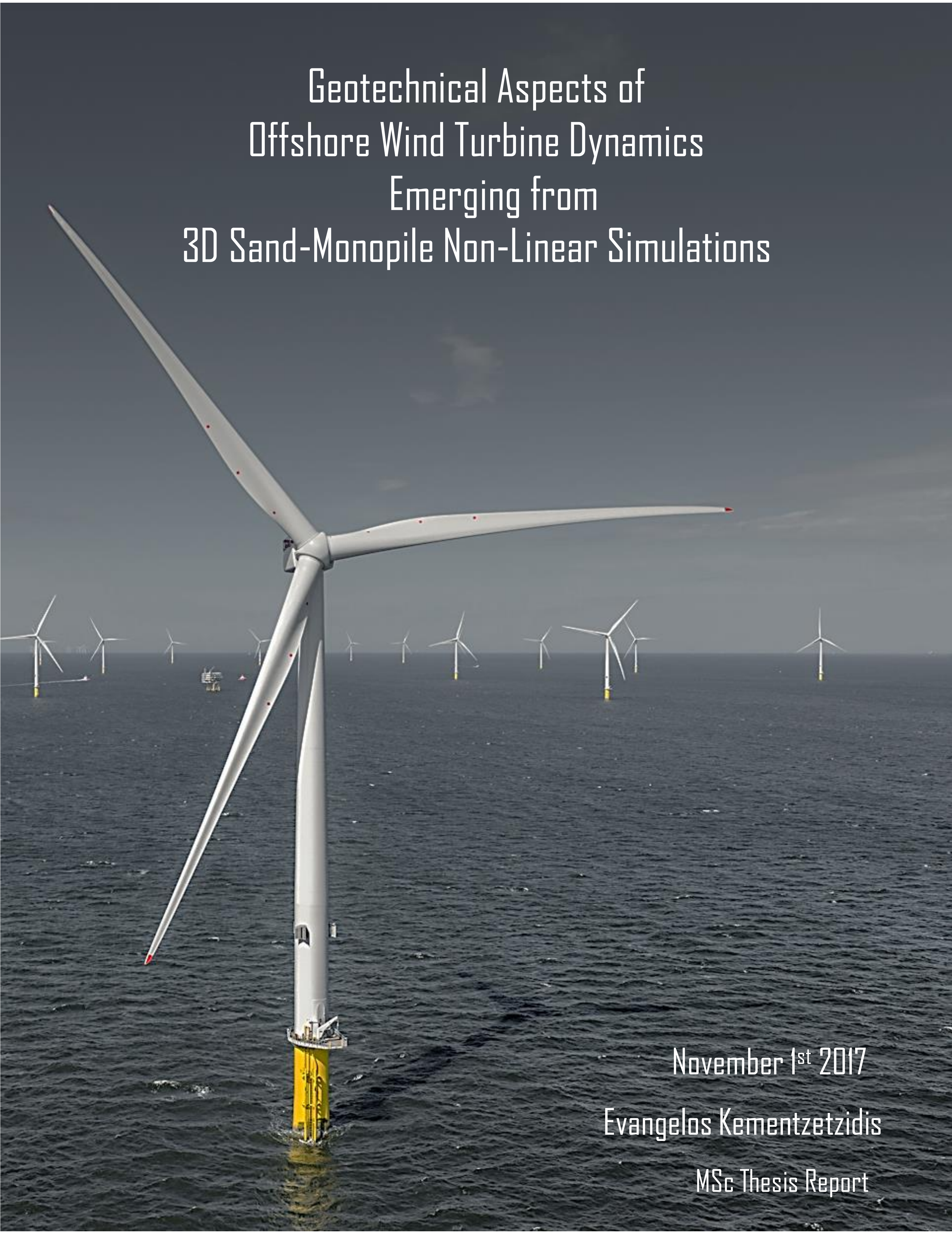

November 1st 2017

Evangelos Kementzetzidis

MSc Thesis Report

TU Delft

Geotechnical Aspects of Offshore Wind Turbine Dynamics Emerging from 3D Sand-Monopile Non-Linear Simulations

A Thesis presented for the degree of Master of Science in Civil Engineering

by

Evangelos Kementzetzidis

Committee:	Prof.dr. K.G. Gavin	TU Delft, chairman
	Dr. Federico Pisanò	TU Delft, daily supervisor
	Dr.ir. K.N. van Dalen	TU Delft, supervisor
	Ir. Willem Geert Versteijlen	Siemens Wind Power, supervisor

Department of Civil Engineering and Geosciences
Section, Geo engineering
TU Delft

November 2017

Abstract

In recent years, offshore wind is becoming an increasingly growing market in Europe. Many resources are allocated towards ensuring its sustainable progress while one of the biggest uncertainties encountered lays in the offshore wind turbine's (OWT) foundations. In Europe, monopiles are the most widely adopted solution to found such structures in the subsoil. Owing to their large diameter and small L/D ratios, the response of these stocky monopiles remains unexplored.

This work is exploiting the merits of 3D finite element (FE) modelling to shed light into the dynamic response of such structures. A detailed design of an 8MW OWT is implemented while soil description is achieved by employing a state of the art constitutive model which encompasses the critical state theory of soils. Long time histories (10mins) followed by rotor stop tests provide critical insight on the dynamic response of large OWTs. The transient evolution of frequency content of the OWTs response, the evolution of pore pressures during storm events, the role of permeability and the contribution of soil in system damping are some of the issues that are addressed in detail.

The effect of placing the monopile on soils of different capacity is examined by modelling sands of different relative density (DR=80%, 60%, 40%). Results show considerable dependence on the state of sand while for the loosest sand case, compliance of the structure to the exerted loads is recorded accompanied with severe non-linear response. Furthermore results indicate that permeability may have a non-negligible impact on the soil's contribution to damping at low loading conditions.

Acknowledgements

The research described in this thesis could not have been realized without the contribution of many people. First of all, I would like to express my special appreciation to Federico Pisanò for his expert guidance, his insightful comments, the fruitful conversations, his continuous support and interest throughout all of the steps of this work. His unending willingness to produce valuable research and his understanding during the misfortunes met, have been catalytic.

Next warm thanks to Pim Versteijlen (TU Delft/Siemens Wind Power) for the realization of the, fundamental to this work, collaboration with Siemens Wind Power (The Hague, The Netherlands) but more so for the rewarding discussions regarding soil damping and wave loading. Furthermore sincere thanks to Axel Nernheim (Siemens Wind Power) for the productive discussions and feedback on this work but also to Vasilis Michalopoulos (Siemens Wind Power) for his useful suggestions on modelling the environmental loads.

This work could not have been accomplished "in time" without the help of my friend Nikos and my sister Sophia who allowed me to abuse their personal computers for a considerable amount of time to run a number of these demanding analysis.

Last but not least, I am deeply grateful to my family for their constant encouragement and support throughout my studies.

Evangelos Kementzetzidis
Delft, November 2017

Contents

List of Figures

List of Tables

1 Introduction

In recent years, the scientific community has been increasingly investigating and reporting global climate change. While a few decades ago environmental sustainability was an unknown term to many, nowadays societies are shaped towards minimizing their footprint into the environment. Europe is advancing towards environmental sustainability by investing into wind power and other forms of green energy. Wind energy can be harvested both on and off-shore. Winds at offshore locations are stronger and generally more uniform than on land. That is attributed to the obliteration of obstacles but also to the lessened air pressure changes during a nycthemeral cycle, resulting in a more stable wind flow. These facts greatly affect power generation as wind power is related to the wind velocity cubed.

For the reasons described above, offshore wind is a booming market with 114 new grid connected wind turbines in the first half (H1) of 2016 distributed in wind farms in the North, the Baltic and the Irish Sea. Furthermore European countries that were left behind in the offshore wind industry are becoming increasing active with publications sprouting in academia assessing the viability of offshore wind with special interest in the Mediterranean Sea (Christoforaki and Tsoutsos, 2017; Bagiorgas et al., 2012; Lavagnini et al., 2003; Balog et al., 2016; Schweizer et al., 2016; Zountouridou et al., 2015).

According to WindEurope [1], formerly known as the E.W.E.A. wind accounted for 44% of all new power installations in Europe during H1[2] of 2016. All the OWTs and 97% of those installed in 2015 were founded on large monopile foundations. As Northern European countries are still investing in offshore wind, where monopile foundations are most common, plenty of research is currently undertaken to reduce uncertainties and subsequently costs. Open issues for OWTs founded on large diameter offshore monopiles would be:

- Lateral monopile stiffness and its evolution during storm events, which is affected by the development of excess pore pressures around the monopile and results in transient shifts in the system's eigen-frequencies;
- Estimation of soil damping, where according to (WindEnergie, 2005a; Versteijlen et al., 2011) soil damping is the most uncertain contributor to OWT damping;
- Long term response, after thousands of loading cycles which is dominated by soil fatigue;

1.1 This study

To address the uncertainties regarding the OWT's response during storms but also to gain further insight on the contribution of damping, this study employs state of art 3D soil-monopile simulations. In literature such studies are sparely found (Corciulo et al., 2017; Zdravković et al., 2015; Depina et al., 2015; Cuéllar et al., 2014; Barari et al., 2017; He et al., 2017) probably due to the heavy computational burden. Due to the expenses and challenges of physical modelling, 3D soil-monopile simulations is the only reliable tool in our procession to inspire and improve simplified methods seeking to pre-estimate details about the response of OWTs that influence their design (natural frequency, rotations and displacements at the monopile head).

This study is able to shed light in all the aforementioned aspects as it introduces a very realistic design of an 8-MW offshore wind turbine, escorted by loads on both sides of the threshold of a U.L.S. state. Displacement and rotation on the monopile head are monitored throughout the analysis, while an analysis time of 600s (10' is the time frame at which wind conditions can me assumed to be steady-state), which is by far the longest seen in literature so far, allows the authors

[1] `www.windeurope.org`
[2] First half of a financial year

to monitor the frequency response of the OWT and its evolution caused by the ever-changing state (stiffness and capacity) of the soil domain during loading.

Size the of OWT The offshore industry is constantly shifting towards larger OWTs (Figure 1). Almost annually the press covers stories about large OWTs setting the record for higher energy production with:

- 5-MW Gamesa turbine in Spain (2014 / monthly production record)[3] ;
- 8-MW MHI Vestas Offshore wind prototype turbine in Denmark (2014 / daily production record)[4] ;
- 9-MW MHI Vestas Offshore wind prototype turbine in Denmark (2017 / daily production record)[5] ;

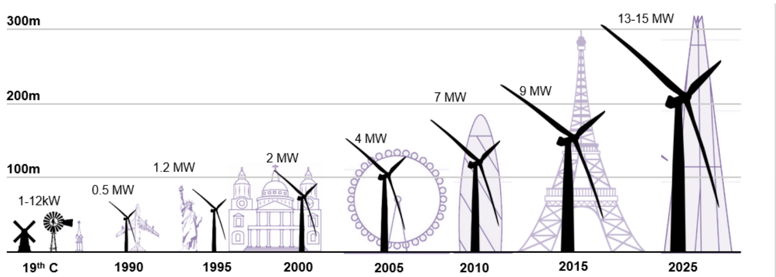

Figure 1: Evolution of wind turbine heights and output, (source: Bloomberg Finance).

For research to remain relevant it has to follow the market trends especially on such technical issues. In that context, the current study examines an 8-MW offshore wind turbine which can be seen in (Figure 4).

1.2 Current practice

To avoid unintended response of an OWT during its lifetime, (WindEnergie, 2005b) has advised rather strict design criteria describing tolerable deformations and displacements at the monopile head during the life-cycle of the offshore turbine. It also states that a 5% shift of the first eigenfrequency during the life-cycle of the turbine can be expected, which is attributed to changes in mass and foundation geometry and not directly to loading conditions.

Pile head deflections and rotations but also eigenfrequency response are dominated by the foundation stiffness. In practice foundation stiffness is estimated by the non-linear p-y curves method (API, 2000; DNV, 2014). The p-y curve formulations are deemed to be reliable for the cases for which they were conceived, which is small diameter, flexible piles on mostly monotonic loads validated to a small number of cycles. Offshore monopiles are stocky with diameters ranging up to 10m which fall way beyond the p-y curves predictive capabilities. Already the fact that the stiffness of large, stocky monopiles is under-predicted is reported by (Kallehave et al., 2012b; Doherty and Gavin, 2012). In this context the applicability of methods used to meet tolerable deformations criteria but also to estimate the natural frequency of offshore wind turbines simulating the soil with formulations intended for long flexible piles e.g. (Arany et al., 2017), become questionable.

[3] `www.offshorewind.biz`
[4] See footnote 3
[5] `www.mhivestasoffshore.com`

Table 1: Summary of natural frequencies predicted for NREL 5MW OWT in normally consolidated marine clay using different p-y models,(Senanayake et al., 2017).

p-y Model	Natural Frequency of Structure
(API, 2011)	0.217 Hz
(Matlock, 1970)	0.224 Hz
(Jeanjean et al., 2009)	0.229 Hz

Attempts to conform the existing formulations with large monopiles have been made, (Kallehave et al., 2012b) while in 2013 the Pile Soil Analysis Project (PISA) (Byrne et al., 2017) was established which resulted from a big collaboration between energy companies and the academia seeking to gain further insight on the response of large monopile foundations though numerical modelling and medium scale field testing. Furthermore, notable attempts to address the dynamic stiffness of large monopiles with field tests are found in literature (Versteijlen et al., 2017).

Prediction of natural frequency Estimation of the 1^{st} eigen-frequency of the OWT is of major importance especially when the so-called soft-stiff design approach is employed. The soft-stiff design results in a structure where load excitation frequencies surround the first natural frequency response of the structure (Figure 2).In that context, as small changes in soil stiffness could swift the natural frequency closer to the excitation frequencies resulting in unplanned resonance, the calculation of the first eigen-frequency and the estimation of its evolution during storms is of utter importance.

With only a small window of non-resonating eigen-frequencies, attempts for their estimation beforehand, have been undertaken by many. (Senanayake et al., 2017) attempted to estimate the natural frequency of the NREL 5MW offshore wind turbine in normally consolidated marine clay using the different p-y models used in practice. Discrepancy is indicated between the results obtained seen in (Table 1). (Arany et al., 2015) proposed an analytical model to predict the natural frequency of OWTs where soil is simulated by a three spring model including a lateral, a rotational and a cross-coupling spring. The methodology was applied on existing offshore turbines where acceptable agreement with the measured natural period was reported.

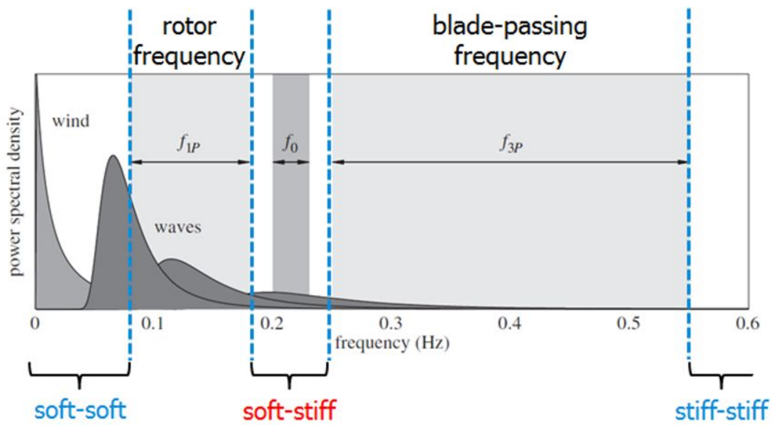

Figure 2: Loading frequencies that excite an OWT, modified from (Kallehave et al., 2015a).

2 Integrated soil-monopile-turbine 3D FE modelling

2.1 Low frequency dynamics of saturated soils

2.1.1 Governing equations and numerical solution

Following the work by Zienkiewicz and coworkers (Zienkiewicz et al., 1999), the so-called u–p formulation is here adopted to describe the dynamic HM response of the soil around the monopile. The u–p approach relies on the assumptions of (i) small soil deformations, (ii) incompressible soil grains, (iii) solid and fluid phases with constant densities and, importantly, (iv) negligible fluid acceleration. While more theoretical background can be found, for instance, in Zienkiewicz et al. (1980); Zienkiewicz and Shiomi (1984); Zienkiewicz et al. (1999), the following conceptual/practical reasons lead to adopt the u–p formulation in OWT applications:

- neglecting fluid inertia has proven accurate for low loading frequencies (Zienkiewicz et al., 1980; López-Querol et al., 2008). This limitation, widely accepted in earthquake dynamics (Zienkiewicz et al., 1999), seems still "harmless" in the presence of wind/wave loading (i.e. frequencies lower than 0.5 Hz – see Sections 3.1 and 3.3);

- compared to other mathematical formulations, the FE approximation of the u–p model features the least number of nodal unknowns (Zienkiewicz and Shiomi, 1984; Jeremić et al., 2008), positively impacting the computational costs of numerical analysis.

Using standard matrix notation (Helnwein, 2001), the u–p differential system couples the global equilibrium of the mixture (Equation (1a)) with the mass balance of the fluid phase (Equation (1b)):

$$\nabla \cdot \left(\boldsymbol{\sigma}' - p\mathbf{1}\right) + \rho\mathbf{g} - \rho\ddot{\mathbf{u}} = \mathbf{0} \tag{1a}$$

$$\dot{\varepsilon}_{vol} + \frac{n}{K_f}\dot{p} + \nabla \cdot \left[\mathbf{k}\left(-\nabla p + \rho_f \mathbf{g}\right)\right] = 0 \tag{1b}$$

where the scalar equation (1b) already includes the momentum balance and the Darcy flow of the fluid. In system (1), $\mathbf{u}$, $\boldsymbol{\sigma}'$, ε_{vol} and n are the displacement, effective stress, volumetric strain and porosity of the soil solid skeleton; ρ is the mass density of the solid–fluid mixture[6]; K_f and ρ_f are the bulk modulus and mass density of the fluid; $\mathbf{k}$ and $\mathbf{g} = [0, 0, g]^T$ represent the permeability tensor and the gravity acceleration field, respectively. Further, ∇ and $\nabla\cdot$ denote gradient and divergence operators, dots stand for time derivatives and $\mathbf{1} = [1, 1, 1, 0, 0, 0]^T$ is the vector representation of the Kronecker second–order tensor. Tensile effective stresses and compressive pore pressure are taken as positive in the analytical formulation, whereas numerical results will be plotted according to the standard Soil Mechanics convention – positive compressive stresses and pore pressure.

Isotropic permeability is assumed throughout this work, so that a single scalar permeability k value can be used:

$$\mathbf{k} = k \begin{bmatrix} 1 & 0 & 0 \\ 0 & 1 & 0 \\ 0 & 0 & 1 \end{bmatrix}, \quad k = \frac{k^{darcy}}{\rho_f g} \tag{2}$$

where the relationship between k (dimension $[\mathrm{L^3TM^{-1}}]$) and the Darcy permeability k^{darcy} employed in standard Soil Mechanics (dimension $[\mathrm{LT^{-1}}]$) is also made explicit. It should also be noted that both $\boldsymbol{\sigma}'$ and ε_{vol} are ultimately functions of the displacement field $\mathbf{u}$, so that $\mathbf{u}$ and p are the only actual unknowns in (1).

[6] $\rho = (1-n)\,\rho_s + n\rho_f$ and is obtained as the porosity–weighted average of the solid and fluid densities.

2.1.2 FE formulation and technology

The weak forms of Equations (1a)–(1b) can be discretised in space according to the standard Galerkin–FE method (Zienkiewicz and Taylor, 2000), featuring the approximations $\mathbf{u} \approx \mathbf{N}_u\mathbf{d}$ and $p \approx \mathbf{N}_p\mathbf{p}$ for the displacement and the pore pressure fields ($\mathbf{N}_u$ and $\mathbf{N}_p$ are arrays of interpolation functions). The space–discretisation process leads to the following discrete form of system (1) (Zienkiewicz and Shiomi, 1984):

$$\overbrace{\mathbf{M}\ddot{\mathbf{d}}}^{\text{mixture inertiae}} + \overbrace{\int_\Omega \mathbf{B}^T\boldsymbol{\sigma}' d\Omega}^{\text{soil internal forces}} - \overbrace{\mathbf{Q}\mathbf{p}}^{\text{pore pressure forces}} = \overbrace{\mathbf{f}^{ext}_{u,\Omega} + \mathbf{f}^{ext}_{u,\Gamma}}^{\text{mixture external forces}} \tag{3a}$$

$$\overbrace{\mathbf{Q}^T\dot{\mathbf{d}}}^{\text{soil dilation/compaction}} + \overbrace{\mathbf{S}\dot{\mathbf{p}}}^{\text{fluid compressibility}} + \overbrace{\mathbf{H}\mathbf{p}}^{\text{seepage}} = \overbrace{\mathbf{f}^{ext}_{p,\Gamma} + \mathbf{f}^{ext}_{p,\Omega}}^{\text{fluid external fluxes}} \tag{3b}$$

where the relevant matrices/vectors are defined as:

$$\mathbf{M} = \mathop{\mathsf{A}}_{m=1}^{N_{el}} \left(\int_{\Omega^e} \mathbf{N}_u^T \rho \mathbf{N}_u d\Omega^e \right) : \text{mixture mass matrix} \tag{4a}$$

$$\mathbf{Q} = \mathop{\mathsf{A}}_{m=1}^{N_{el}} \left(\int_{\Omega^e} \mathbf{B}^T \mathbf{1} \mathbf{N}_p d\Omega^e \right) : \text{HM coupling matrix} \tag{4b}$$

$$\mathbf{S} = \mathop{\mathsf{A}}_{m=1}^{N_{el}} \left(\int_{\Omega^e} \mathbf{N}_p^T \frac{n}{K_f} \mathbf{N}_p d\Omega^e \right) : \text{fluid compressibility matrix} \tag{4c}$$

$$\mathbf{H} = \mathop{\mathsf{A}}_{m=1}^{N_{el}} \left(\int_{\Omega^e} \boldsymbol{\nabla}\mathbf{N}_p^T \mathbf{k} \nabla \mathbf{N}_p d\Omega^e \right) : \text{permeability matrix} \tag{4d}$$

$$\mathbf{f}^{ext}_u = \mathbf{f}^{ext}_{u,\Omega} + \mathbf{f}^{ext}_{u,\Gamma} = \mathop{\mathsf{A}}_{m=1}^{N_{el}} \left(\int_{\Omega^e} \mathbf{N}_u^T \rho \mathbf{g} d\Omega^e \right) + \mathop{\mathsf{A}}_{m=1}^{N_{el}} \left(\int_{\Gamma^e} \mathbf{N}_u^T \mathbf{t} d\Gamma^e \right) : \text{mixture external force vector} \tag{4e}$$

$$\mathbf{f}^{ext}_p = \mathbf{f}^{ext}_{p,\Omega} + \mathbf{f}^{ext}_{p,\Gamma} = -\mathop{\mathsf{A}}_{m=1}^{N_{el}} \left(\int_{\Omega^e} \boldsymbol{\nabla}\mathbf{N}_p^T \rho_f \mathbf{k} \mathbf{g} d\Omega^e \right) + \mathop{\mathsf{A}}_{m=1}^{N_{el}} \left(\int_{\Gamma^e} \mathbf{N}_p^T \mathbf{q} d\Gamma^e \right) : \text{fluid external flux vector} \tag{4f}$$

In the above definitions, $\mathbf{t}$ and $\mathbf{q}$ denote the vectors of surface traction and flux for the solid and the fluid phases, respectively, $\mathbf{B}$ is the standard matrix of solid compatibility, and A is the matrix/vector assembly operator (Hughes, 1987). In Equation (3a), the internal force term is implicitly associated with the global (tangent) stiffness matrix, while additional viscous damping could be generated either at the constitutive level (viscous soil behaviour) or through numerical Rayleigh damping (Chopra, 1995; Zienkiewicz et al., 1999).

As for the FE technology, the interpolation functions in $\mathbf{N}_u$ and $\mathbf{N}_p$ cannot be chosen arbitrarily, but have to fulfil the so-called *inf–sup* condition (Babuška, 1973; Brezzi, 1974; Pastor et al., 1999). In particular, if the fluid compressibility and the skeleton permeability are small, then "checkerboard" oscillation modes and locking in the pressure field may arise, and thus jeopardise the accuracy/reliability of numerical predictions. Unfortunately, the *inf–sup* condition is not satisfied by elements allowing for equal-order interpolation of $\mathbf{u}$ and p, unless *ad hoc* stabilisation techniques are adopted. The need for reduced computational costs in 3D computations motivated significant research efforts on the search for stabilised low–order FEs, as documented by Zienkiewicz et al. (1999) and, more recently, Preisig and Prévost (2011); McGann et al. (2012, 2015); Zhang et al. (2016). It should also be recalled that – quoting Preisig and Prévost (2011) – "methods that work well for incompressible elasticity, such as Bbar (Hughes, 1987) or elements that satisfy the LBB-condition, do not guarantee oscillation-free results in the case of poromechanics".

In this work, the low-order eight-node hexahedral element with single-point quadrature (H1-P1ssp) recently proposed by McGann et al. (2015), implemented in OpenSees framework as SSP-BrickUP element, is adopted. H1-P1ssp brick elements feature:

- reduced integration and stabilisation of spurious hourglass modes;
- enhanced assumed strain field for remedying volumetric and shear locking;
- analytical pre–integration for the terms stabilising the solid phase response, resulting in increased computational efficiency;
- linear interpolation functions for both $\mathbf{u}$ and p, and non-residual–based stabilization scheme to cope with undrained/incompressible responses in dynamic HM problems (Huang et al., 2004).

All the items in the above list contribute to the stability, accuracy and efficiency of H1-P1ssp elements, which may be now regarded as a low–order alternative to H2-P1 elements for larger and/or more refined discrete models. The FE results presented in the following will demonstrate the suitability of the H1-P1ssp element formulation, here applied for the first time to the analysis of offshore wind systems.

The aforementioned non-residual–based stabilization produces an additional laplacian term in Equation (3a) (McGann et al., 2015):

$$\mathbf{Q}^T\dot{\mathbf{d}} + \left(\mathbf{S} + \tilde{\mathbf{H}}\right)\dot{\mathbf{p}} + \mathbf{H}\mathbf{p} = \mathbf{f}^{ext}_{p,\Gamma} + \mathbf{f}^{ext}_{p,\Omega}, \quad \text{where:} \quad \tilde{\mathbf{H}} = \mathop{\mathsf{A}}_{m=1}^{N_{el}} \left(\int_{\Omega^e} \nabla\mathbf{N}_p^T \alpha \nabla\mathbf{N}_p d\Omega^e\right) \tag{5}$$

preventing the well-known numerical issues associated with vanishing compressibility and permeability matrices ($\mathbf{S}$ and $\mathbf{H}$ in (4)). On the practical side, setting the numerical coefficient α in (5) corresponds with deciding on the "amount of stabilisation" injected into the discrete system (3): too low or too high α values would result in either ineffective or excessive[7] stabilisation. In what follows, the suggestion by Huang et al. (2004); McGann et al. (2012, 2015) will be taken as a reference:

$$\alpha = \frac{\alpha_0 h_{el}^2}{G_s + \frac{4}{3}K_s} \tag{6}$$

where h_{el} is, heuristically, the average element size within the FE mesh, G_s and K_s are the bulk and shear moduli of the soil skeleton, whilst α_0 is a scalar coefficient in the range of 0.1–0.5.

2.2 Elastic-plastic modelling of cyclic sand behaviour

The numerical analysis of environmentally loaded OWT systems is strictly connected to the modelling of cyclic soil behaviour. In the last decades, numerous cyclic soil models have been formulated in the framework of different plasticity theories, including *multi-surface plasticity*, *bounding*

[7]Excessive stabilisation is meant as an unrealistic/unphysical attenuation of the pore pressure field, due to the laplacian/diffusive nature of the stabilising term (5).

surface plasticity, *generalized plasticity*, *hypoplasticity* and *hyperplasticity*. A number of valuable contributions are here worth citing, such as – to mention only a few – Mróz et al. (1978); Prévost (1985); Zienkiewicz et al. (1985); Pastor et al. (1985); Wang et al. (1990); Borja and Amies (1994); Manzari and Dafalias (1997); Gajo and Wood (1999); Puzrin and Houlsby (2001); Papadimitriou and Bouckovalas (2002); Elgamal et al. (2003); Houlsby and Mortara (2004); Dafalias and Manzari (2004); Dafalias et al. (2006); Taiebat and Dafalias (2008); Yang and Elgamal (2008); Andrianopoulos et al. (2010); Pisanò and Jeremić (2014); Taborda et al. (2014); Seidalinov and Taiebat (2014); Tasiopoulou and Gerolymos (2016). Comprehensive overviews on cyclic soil modelling are given, for instance, by Prévost and Popescu (1996), Zienkiewicz et al. (1999), di Prisco and Wood (2012) and (Corti et al., 2016).

2.2.1 CSSM modelling of cyclic sand behaviour

The present study relies on the bounding surface plasticity model of (Dafalias and Manzari, 2004) building up on their previous work (Manzari and Dafalias, 1997) which was extended to account for the effect of fabric changes in sand during shear loading.

The main features included in the constitutive model are hereafter summarized, see (Figure 3):

- a stress ratio ($\boldsymbol{r}$), deviatoric ($\boldsymbol{s}$) over hydrostatic (p), controlled formulation, with no "hydrostatic" yield loci present as in (Wang et al., 1990), which is assumed valid in sands as long as no crushing of grains takes place;
- kinematic hardening formulated upon the back-stress ratio ($\boldsymbol{\alpha}$);
- an independent of J_3 deviatoric stress invariant, very small in size and circular on the π plane yield surface;
- the critical state theory of soils is included though the *state parameter* ψ , originally proposed by (Been and Jefferies, 1985; Wood et al., 1994) to account for effective confinement stress level and void ratio effects on sand response;
- bounding M^b surface formulation (Li and Dafalias, 2000; Manzari and Dafalias, 1997) which allows to model the softening response of dense samples but also reverse and cyclic modelling response simulation by moving into stress space as a function of *state parameter* ψ;
- phase transformation surface M^d (Tatsuoka and Ishihara, 1974; Ishihara et al., 1975) introduced to distinguish dilative and compactive soil response, which moves in stress space with reference to the critical state line M according to the *state parameter* ψ;
- softening response is modelled by a stress ratio related hardening modulus which depends on the distance of back stress ratio tensor $\boldsymbol{\alpha}$ and the back stress ratio of the projection of the normal to the yield surface upon the bounding surface $\boldsymbol{\alpha}^b_\theta$;
- a fabric dilatancy tensor $\boldsymbol{z}$ which allows for enhanced contractile response upon reversal of loading after a loading phase which induces dilatancy , due to changes in the fabric of non-cohesive soils, which agrees with observations made by (Nemat-Nasser and Tobita, 1982; Nasser, 1980);

By incorporating CSSM, the model of Manzari and Dafalias, hereafter refereed to as SaniSand2004, is able to describe the response of sands in a variety of effective confinement stresses and states. Accounting for the long time histories analysed in this study, the involvement of CSSM ensures realistic modelling of response in regions around the monopile where high stress ratios ($\boldsymbol{s}$) will be an agent for non-negligible plastic volumetric strains. The performance of the model in cyclic 2-way loading conditions can be seen in (Appendix A.1).

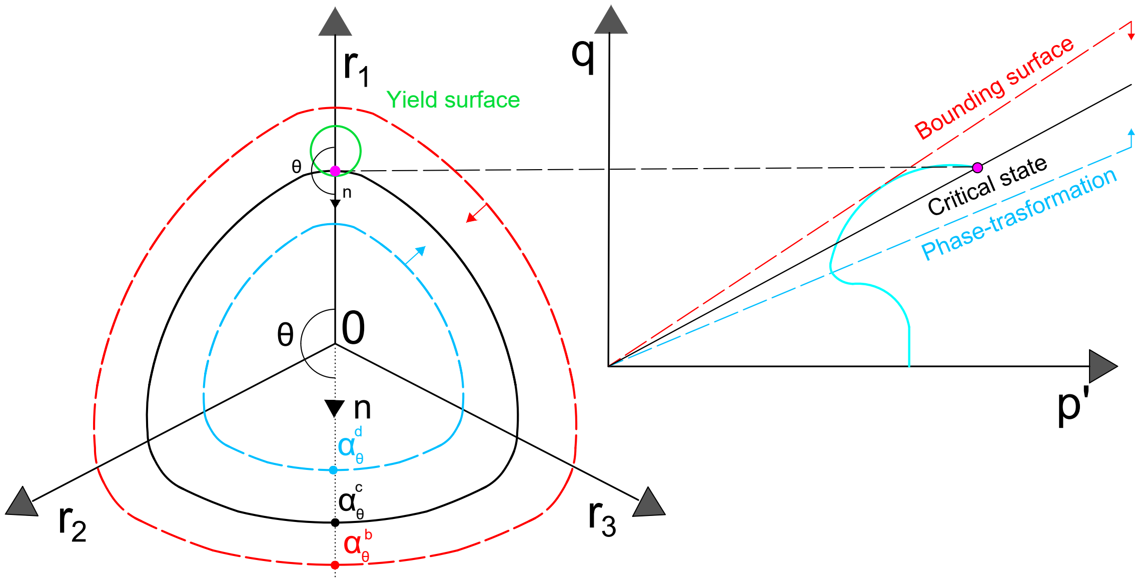

Figure 3: a) Schematic of yield, critical, dilatancy and bounding surfaces on the stress ratio π plane b) a representation of a stress path from an undrained triaxial compression. In the latter, the main effect of dilatancy and bounding surfaces can be seen which in reality are mobile in stress space while in both figures both surface positions do not correspond to the stress state depicted.

Constitutive parameters/ Model calibration An attempt to calibrate the SaniSand2004 model upon a certain sand type would require the calibration of 15 parameters (Table2). The determination of such parameters is based ideally in triaxial drained and undrained tests (static and cyclic) over a range of relative densities and confinement stresses.

Besides the constitutive parameters, OpenSees allows the user to interfere in the solution process by choosing between explicit and implicit algorithms in the return-mapping process of stress on the yield surface and even allows for specification of the allowable drift from the yield surface. SaniSand2004 implementation in OpenSees was undertaken by Prof. Pedro Arduino and other researchers from the university of Washington.

For this analysis, the Toyoura sand was chosen to describe the soil, while the calibration of this sand to the SaniSand2004 model was published along the model in (Dafalias and Manzari, 2004). By changing the void ratio, the authors were able to simulate the OWT response on 3 different relative densities, 40%, 60% and 80%.

2.3 Monopile and wind turbine

Structure For research to remain relevant it has to follow the market trends especially on such technical issues. In that context, the current study examines an 8-MW offshore wind turbine (Figure 4). The design was provided by Siemens Wind Power A/S with some details being highly confidential. The implementation of the structure was quite intricate including detailed description

Table 2: Sand calibration parameters for (1) the soil domain and (2) the pile-soil interface. Toyoura sand was calibrated and published in(Dafalias and Manzari, 2004)

Variable		Value	
		Toyoura sand (1)	Pile-Soil interface (2)
Elasticity	G_0	125	83.3
	ν	0.05	0.05
Critical state	M	1.25	0.938
	c	0.712	0.712
	λ_c	0.019	0.019
	e_0	0.934	0.934
	ξ	0.7	0.7
Yield surface	m	0.01	0.01
Plastic modulus	h_0	7.05	7.05
	c_h	0.968	0.968
	n^b	1.1	1.1
Dilatancy	A_0	0.704	0.704
	n^d	3.5	3.5
Fabric-dilatancy tensor	z_{max}	4	4
	c_z	600	600

of the evolution of stiffness across its height.

The structure above the mudline (tower and a part of the monopile) was simulated with approximately 160 elastic Timoshenko beam elements with consistent mass matrices describing the mass of the tower shell. Such elements incorporate the Timoshenko beam theory which accounts for shear deformations. The foundation part was modelled with 8-node hexahedral *SSpBrick*, Stabilized Single point integration elements ($H1ssp$) implemented in OpenSees by Chris McGann, Pedro Arduino, and Peter Mackenzie-Helnwein at the University of Washington. $H1ssp$ elements are stabilized by the inclusion of an enhanced strain field which results in an element free of volumetric and shear locking. Elimination of shear locking allows the user to implement a coarser mesh by improving accuracy in bending dominated problems as in this study.

Local concentrated masses were simulated as lumped modelling equipment and structural masses (flanges, transition piece, boat landing and working platforms, ladders etc.) The RNA (rotor-nacelle assembly) mass was modelled by including the total mass as lumped and the rotational inertia I_M associated with nacelle mass imbalances.

Pile-soil interface The sharp discontinuity in hydro-mechanical properties at the soil-foundation interface needs to be carefully handled in most geotechnical problems, including the numerical analysis of laterally loaded piles. As done by Cuéllar et al. (2014) in the context of OWTs, zero-thickness interface elements (also termed joint elements) (Goodman et al., 1968; Zienkiewicz et al., 1970) can be introduced at the soil-monopile contact in combination with a suitable shear/tensile behaviour, possibly allowing for soil-steel sliding/detachment. In this work, the soil-monopile interface is treated according to the simpler approach by Griffiths (1985), i.e. by using thin continuum (SSP) elements to model the physical steel-to-soil transition. As this work intends to simulate heavy lateral loading in which the zero-toe kick condition, which was proposed by (WindEnergie, 2005b) and critised by (Achmus et al., 2009), is expected to be breached, interface on the pile tip was introduced to simulate a band of intensely plastified soil operating under residual strength. The interface layer lateral to the pile has a thickness of 4% the monopile diameter while the pile tip layer is double that width at 8%. A weaker and thus more deformable soil material was assigned for the interface layer by reducing parameters as the elastic stiffness G_0 and

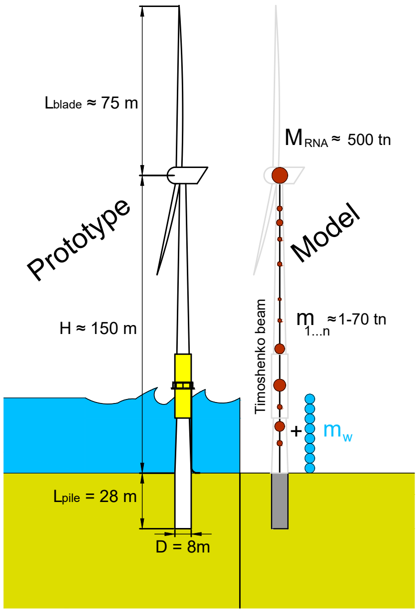

Figure 4: Important information about the OWT simulated in this study (left), along with a depiction of how its was simulated in this numerical analysis (right).

the stress ratio of the critical state line by 2/3 and 3/4 respectively Table 2.

Damping Viscous damping was introduced into the simulation solely on the structural members (monopile foundation and tower), more analytically:

- Soil's contribution to damping is either though radiation damping (dissipation of waves in an ever-increasing continuum) or hysteretic damping which is an intrinsic material property of the soil. Both damping sources do not require direct implementation as they are introduced either from the geometry and the constitutive model respectively.

- Material damping (steel) was implemented following the premises of (En, 1991). A damping ratio $\zeta_{steel} = 0.19\%$ is attributed to all steel sections in frequencies between 0.1 and 80 Hz via the rayleigh damping approach.

- Aerodynamic damping is a dominant source of damping in the fore-aft direction during power production. However it is far less significant for parked and feathered rotors (Tarp-Johansen et al., 2009; Valamanesh and Myers, 2014; Shirzadeh et al., 2013). In the examined cases, wind speeds exceed by far the cut-off speed of the turbine rendering aerodynamic damping insignificant. In that context aerodynamic damping was not accounted for in this study.

- Hydrodynamic damping was added according to (Leblanc and Tarp-Johansen, 2010) which in turn was based on (Tarp-Johansen et al., 2009). This study renders the dominant source of water-induced damping is wave radiation. Furthermore they deduct that an offshore wind turbine with a natural frequency of 0.3 Hz pile diameter of 4.7m located at 20m water depth would approximately have 0.12% critical damping induced from wave radiation. These numbers differ from the OWT examined in this study, but in the lack of further information a critical damping of $\zeta_w = 0.12\%$ was given to the water mass nodes below the seabed.

The inertial influence of the water was implemented by inserting nodal lumped masses following Newman (1977), by introducing an additional water mass (added mass) equal to:

$$m_w = 2\rho_w \frac{\pi D^2}{4} h \tag{7}$$

that is equal to twice the water mass occupying the submerged OWT volume (ρ_w is the water mass density, h is the height between two consequent water mass nodes). As shown in Figure 4, m_w is then evenly distributed as lumped masses along the underwater beam nodes of the OWT.

2.4 Space/time discretisation and solution algorithms

The time integration of the non-linear equation system (3) requires suitable algorithms for (i) global time marching, (ii) step increment solution, and (iii) stress-point integration.

Global time marching Time marching relates to the update of all the relevant field variables from their (known) value at time t_n to time t_{n+1}, over the step increment Δt. Here, the most widespread algorithm in Solid Dynamics – the Newmark integration method (Newmark, 1959) – is been employed. The required integration parameters are set to $\beta = 0.6$ and $\gamma = (\beta + 1/2)^2 /4 = 0.3025$, yielding unconditionally stable time integration (in linear problems) and high-frequency dissipation Hughes (1987).

Step increment solution The implicit Newmark algorithm along with the non-linear equations (3a)–(3b) require an iterative solution scheme for each step increment, usually belonging to the Newton–Raphson family (De Borst et al., 2012). The accelerated Krylov–Newton algorithm described by Scott and Fenves (2003) is here fruitfully exploited, resulting in faster convergence by greatly decreasing the number of Jacobian evaluations per step increment (Carlson and Miller, 1998).

Stress-point integration In the presence of non-linear constitutive equations, a numerical integration scheme is needed to update stresses, strains and hardening variables over the step increment Δt. The selection of a suitable time step size Δt is discussed by Jeremić et al. (2009); Watanabe et al. (2016), also in relation to the use of highly non-linear soil models. The soil model adopted in this study (see Section 2.2) is integrated via the standard forward Euler explicit algorithm (Sloan, 1987).

Space/time discretization Suitable domain size and mesh density must be chosen wisely to ensure the proper description of the pore pressure and the displacement fields in space. A proper mesh has been chosen via a mesh sensitivity analysis which can be found in (Appendix A.2). The resultant mesh can be seen in (Figure 5). A timestep sensitivity analysis was undertaken as well (Appendix A.3).

2.5 S-transform and frequency shifts

In order to estimate the eigen frequencies of the response of the OWT, it is of common practise to look into the displacement time history of the hub. There are many ways to express a displacement time history in terms of its frequency content. Most usually the Fourier amplitude spectrum is utilized, which is calculated among the entire motion time-history under the assumption of periodicity. That is directly related to the fact that the FT represents data as a sum of sinusoidal waves which oscillate indefinitely, not localized in either in time nor space. Thus evolution of the amplitude spectrum over time is neglected in such an approach. Besides neglecting information

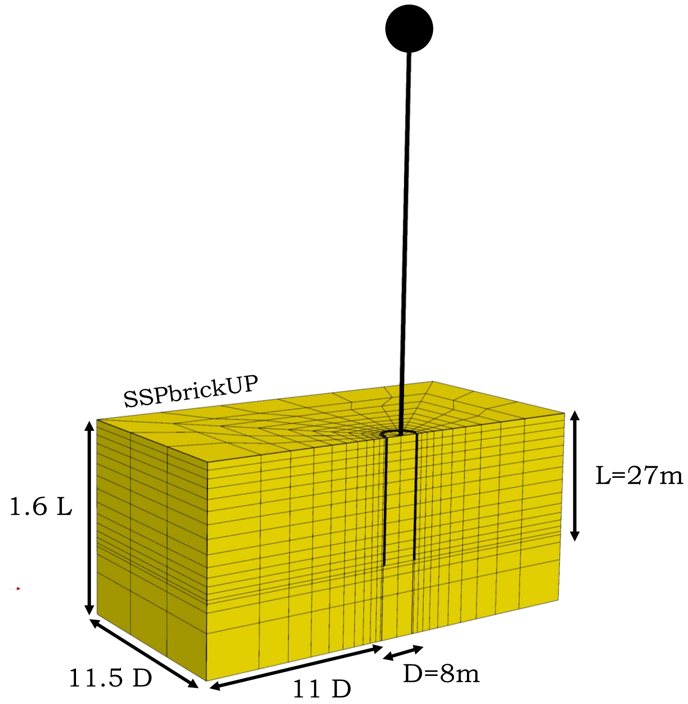

Figure 5: FE discretization of the soil domain.

regarding the timing of frequency shifts, having a signal whose frequency content changes in time, results in a "noisy[8]" FT. That effect is substantially amplified for the cases at which the frequency content of the signal varies greatly over time. As seen in (Figure 19) for the 80% relative density a small range of frequencies is observed while for the loosest soil examined, a wide range of frequencies with almost equal amplitudes can be seen. By using the FT we observe all the frequencies with significant content throughout the analysis with no information about their duration or the time at which they were acting.

The authors wanted a tool that would allow for capturing abrupt changes of frequency content over time, so that frequency shifts related to either changes of excitation frequencies or changes in soil stiffness, could be recorded. In that perspective the short time Fourier transform (STFT) could have been utilized, which results from a series of FTs applied upon a moving window on the signal. The STFT results in good resolution in the frequency domain but time resolution is rather poor. Wavelets are wave like oscillations with finite duration that can be fixed both in time and space by scaling and shifting the wavelets in the time domain. While the wavelet transform could be suitable for the task, they offer a poorer frequency resolution than the S (Stockwell)-transforms (Kramer et al., 2016) utilized in this study. The S-transform, (Equation 8) (Stockwell et al., 1996), was introduced as an extension of the continuous wavelet transform and is based on shifting a frequency-dependent Gaussian window in time (Equation 9). Thus, S-transforms are able to provide frequency dependent resolution for better capturing of the lower and the higher harmonics of a signal.

$$S(\tau, f) = \int_{-\infty}^{\infty} u(t) w(t-\tau, f) e^{-2i\pi f t} dt \tag{8}$$

[8]As a result of the evolution of the frequency content over time, a range of frequency peaks, without a dominant one, are obtained in the FT, (Figure 19, DR=40%).

As described, the most usual window w is Gaussian one which seen below:

$$w(\tau, f) = \frac{|f|}{k\sqrt{2\pi}} e^{-\frac{f^2 t^2}{2k^2}} \tag{9}$$

where f is the frequency, t is time, τ is the time at which the window is fixed and k is a scaling factor greater than zero that controls the number of oscillations in a window. Higher values of k result in higher frequency but a poorer time resolution. In this study the depicted S-transforms are produced with k=0.2. After numerous attempts, for this specific case, it was realized that such a value corresponds to the most desired trade-off that results in a discrete frequency resolution (narrow S-transform width in the frequency domain) but also allows capturing abrupt changes of frequency over time.

3 Non-linear performance under storm loading

3.1 Storm scenarios and analysis program

The analysis program of this study included three different loading scenarios (Figure 6). Two of the scenarios where provided by Siemens Wind while the third one resulted from manipulating one of the loading cases provided.

The first loading scenario, *Case A*, represents a storm with a 50-year return period, having an average wind velocity of 47 m/s. At approximately 70 seconds of analysis the turbine is hit by a rogue wave ($\approx 10m$ tall). *Case B* represents a heavy storm with an average wind velocity of 24 m/s. For both cases, as wind speed surpasses by far the cut off wind speed, the blades of the turbine are pitched out, resulting in wave load dominated load histories. Both *Cases A* and *B* are analysed to examine the response of a large OWT on extreme and strong loading conditions respectively.

Case C was conceived by dividing *Case B* loads by five and serves as a control analysis in which the effects of considerably lower load amplitudes are examined. As the frequency content of the environmental loading does change when wind velocities and thus load excitations are lower, this is a rather non-physically realistic case.

After each analysis load history was analysed, the so called in literature "rotor-stop" test was implemented, while in this case a more precise description would be "load-stop". To achieve this, all loads were removed from the domain to allow the turbine perform a free vibration. The purpose behind this setting is to calculate the soil's contribution to damping through the logarithmic decrement method but also to gain further insight on the OWT's natural frequency.

Load application The load time-histories provided included specifications regarding the load application points. As such, the wave loads were distributed across the length of the submerged part of the OWT, while wave height was accounted for, by loading the structure above MSL [9] during a wave impact. The importance of distributing the wave loading became evident during the rogue wave impact. In that instant, nodes ranging up to 10 meters above the mean sea level were loaded to ensure a realistic simulation. As during these loading cases, the OWT's blades are pitched off, the wind loads are almost evenly distributed across the tower. These were simulated by the application of a lateral load time history near the tower's base (Figure 7).

3.1.1 Analysis program

As described in 2.2.1, this analysis explores the response of an offshore wind turbine on three different soil densities. The foundation design provided by Siemens Wind Power A/S was conceived according to offshore standards and norms, for an OWT located on a layered sandy soil

[9] Mean Sea Level

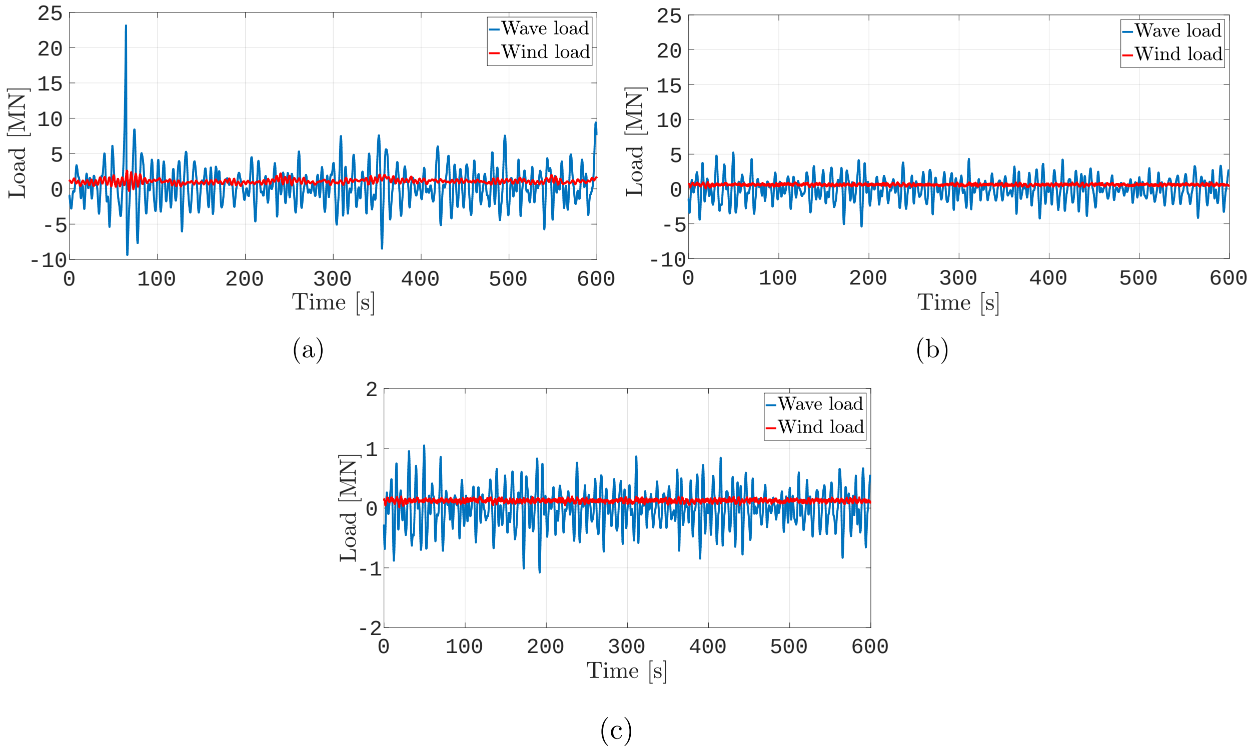

Figure 6: Examined loading scenarios (a) *Case A*: Rogue wave, 50-years storm, (b) *Case B*: heavy storm, (C) *Case C*: low loading scenario.

with densities varying from 70-80%. Furthermore in all analysis the same foundation design was implemented, regardless of the soil density examined, so that conclusions could be drawn from this study without the interference of further variables. It should be highlighted that by using the Toyoura sand parameters, one neglects characteristics of the specific sand this foundation was designed upon. Relative density can reliably indicate the state of the sand and thus describe up to a certain degree its response but it still remains a simple index which neglects various aspects of the overall very complicated response of sands especially when considering cyclic loading. For further details with focus on the SaniSand2004 model one should consult (Zahmatkesh and Janalizadeh Choobbasti, 2017).

A set of analysis was created, where mainly the effect of changing the relative density was considered. Furthermore for specific cases, the soil permeability was altered by an order of magnitude, from the considered permeability which was $k = 10^{-5} m/s$ to estimate its effect. The nominal value of chosen permeability relates to poorly graded sands, gravelly sands with little or no fines obtained from [10] and published by (Swiss Standard, 1999; Carter et al., 1991; Leonards, 1962; Dysli and Steiner, 2011).
The analysis program can be seen in (Table 3).

3.2 Dynamic sand-monopile interaction

3.2.1 Sand hydro-mechanical response and void ratio effects

In order to examine and discuss the behaviour of the soil during the examined load histories, 6 control points were chosen ($A_{L,R}$, $B_{L,R}$, $C_{L,R}$) located at depths close to the mudline, near the middle of the monopile embedment length and in the vicinity of the tip (Figure 7). In this section, the hydro-mechanical response of sand is depicted via plots of stress-strain response, deviatoric

[10] www.geotechdata.info

Table 3: Analysis program specifying the range of permeabilities examined.

Sand relative density		40%	60%	80%
Loading scenario	Case A	$k = 10^{-5} m/s$	$k = 10^{-4,-5,-6} m/s$	$k = 10^{-5} m/s$
	Case B	$k = 10^{-5} m/s$	$k = 10^{-4,-5,-6} m/s$	$k = 10^{-5} m/s$
	Case C	$k = 10^{-5} m/s$	$k = 10^{-4,-5,-6} m/s$	$k = 10^{-5} m/s$

versus mean effective stress and pore pressure over mean confining stress (u/p) versus time for *Case A*. Furthermore void ratio effects will be examined by presenting relative density evolution over time.

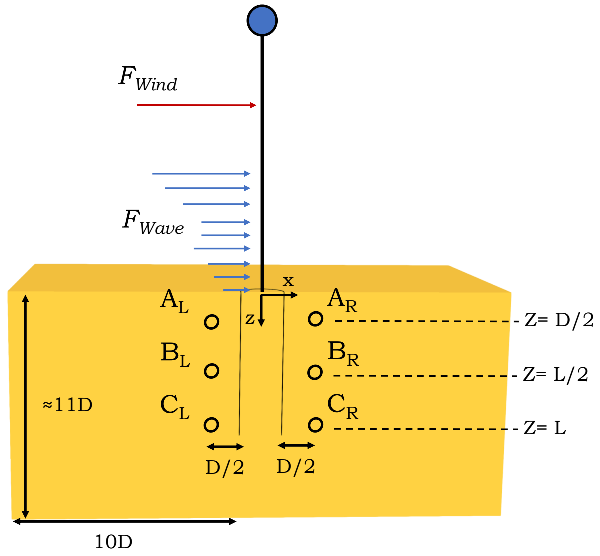

Figure 7: Depiction of the analysed domain with specification of the location for control points ($A_{L,R}$, $B_{L,R}$, $C_{L,R}$).

Excess pore pressure By employing the 'U-P' formulation and the SaniSand2004 model, pore pressure evolves due to (i) changes of the mean stress p, (ii) drainage conditions, (iii) change of soil volume occurring under plastic shear loading controlled by a non-associative flow rule. In (Figure 8) plots of pore pressure over mean confinement stress versus time at all control points are presented. All control points experience an increase of pore pressure while, as expected, the loosest soil has the most contractile tendency resulting in an enhanced excess pore pressure accumulation. Furthermore a plateau indicating liquefaction ($u = p$) is reached after a short time of strong loading in all of the examined points, for DR=40%. For 80% relative density liquefaction is never reached indicating a more "restless" response while in the case with DR=60% pore pressure evolution displays characteristics of both the loosest and the densest sand configurations. Incapability to increase pore pressures beyond liquefaction($u > p$), is attributed to the fact that during liquefaction, sand shear strength is zero leading to inability to produce further plastic volumetric shear strains as stress ratio remains almost immobile moving upon the critical state line.

As discussed in 3.1 *Case A* is a heavy storm case examining also a rogue wave impact. The effect of the rogue wave becomes evident as at approximately 70 seconds of analysis where an abrupt decrease of both u/p and pore pressure is observed in all soil densities and all control points highlighting the excessive shearing introduced in the domain. It is interesting to note that control points at both sides of the foundation experience a drop in u/p. For the right side which is the "passive side" of the soil, this is attributed to excessive shearing, which surpasses the contractile response due to the increase of mean stress, giving a dilative tendency to the soil. On the left side of the domain, dilative tendency is explained by drop of the mean effective stress but also due to shearing, as a stress state similar to triaxial extension occurs in the soil. Soil dilation is observed for all relative densities while as expected the highest pore pressure drop is experienced by the densest soil.

It is interesting to note that the on the left side of the monopile, for the top A_L and middle B_L control points a sharper drop of u/p is observed compared to the right side while this is not true for the lowest control points C_L and C_R. That effect can be attributed to the sharp decrease of mean confining stress on the "active" side compared to the sharp increase on the passive side of the foundation attributed to the monopile movement. The fact that the lower point $C_{L,R}$ behaviour differs is attributed to the rotation of the monopile, which for this loading case, takes place at a point located in-between control points B and C.

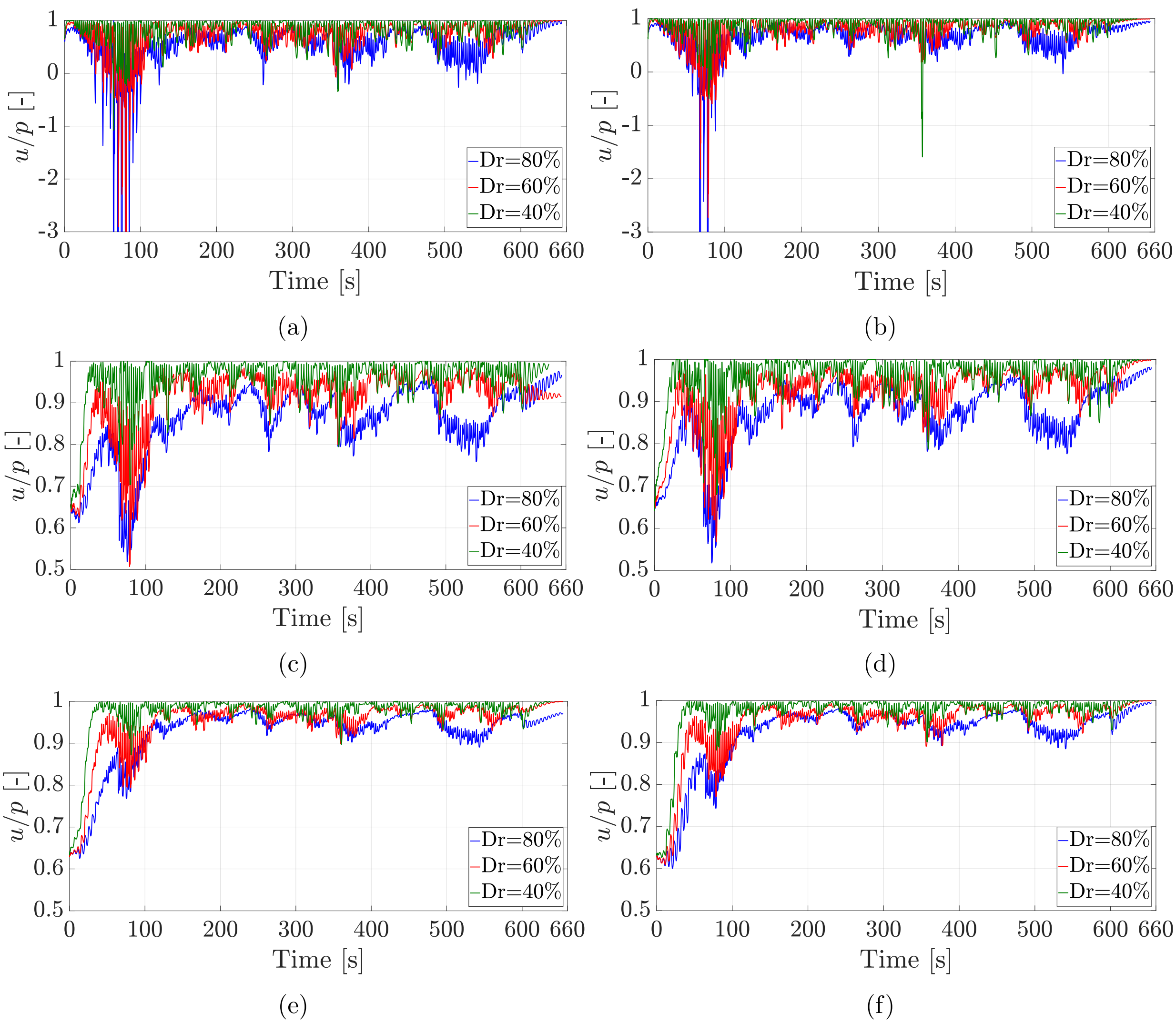

Figure 8: Pore pressure over mean confinement stress versus time in all control points for all relative densities for $CaseA$: (a) A_L, (b) A_R, (c)B_L, (d) B_R, (e)C_L, (f) C_R.

Spatial distribution of pore pressures The transient evolution of pore pressures appears similar across all relative densities at the control points considered. The control points where located approximately half a monopile diameter away from the monopile and thus experience heavy loading during these extreme loading scenarios. In order to obtain a cleared picture of the pore pressure distribution during the analysis, the pore pressure field is depicted in (Figure 9) at 150 and 300 seconds of analysis time for all relative densities. It becomes evident that the pore pressure field is significantly affected by the sand void ratio. The isolines depict excess pore pressures ranging from 150-300 kPa in 5 increments. In the dense sand case, high excess pore pressures are localized only on the pile tip and form a narrow "butterfly-shaped" pore pressure field across the pile length, while for the loosest sand case high excess pore pressures are spread in the whole domain still presenting a "butterfly shaped" pore pressure field which in this case is wider and significantly more enhanced. The narrowness and wideness of the butterfly-looking pore pressure field should not be attributed to the tendency to produce higher excess pore pressures found in the loosest soils, but it can be attributed to their capacity and stiffness. Excess pore pressures are mostly agitated through plastic volumetric strains in SaniSand 2004 which in turn are produced solely by plastic shear strains. A looser medium, in this case the soil, owing it to its lower capacity and stiffness, will tend to distribute in a larger area the stresses caused by the loads to reach equilibrium. This results in an enhanced shear loading in a wider and less sharply inclined region around the monopile, as seen in (Figure 9).

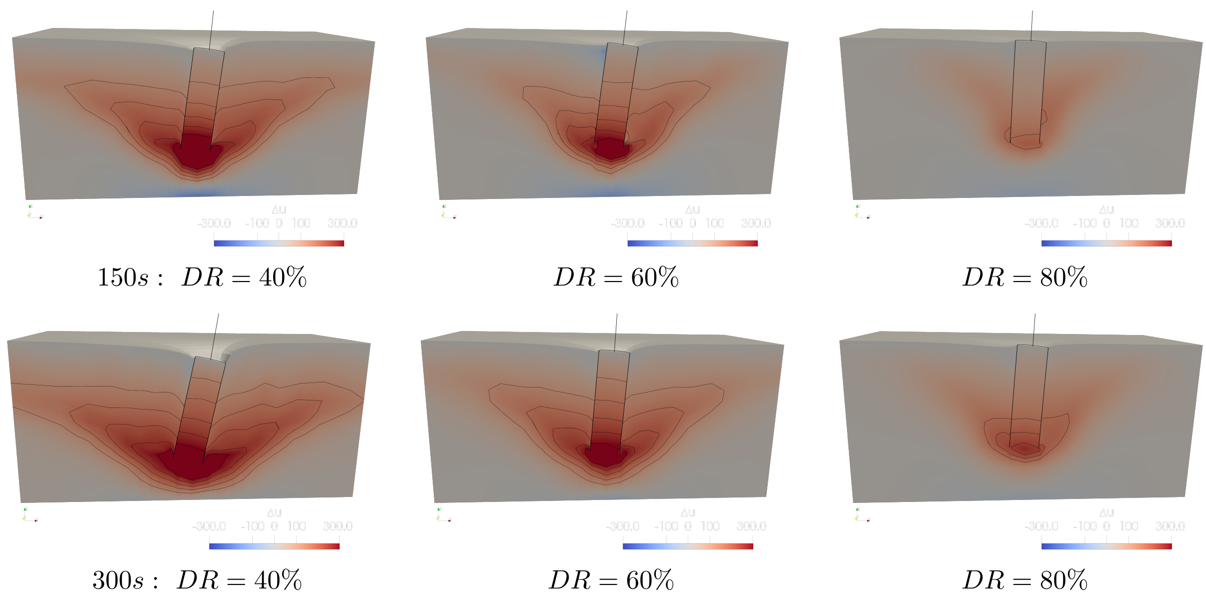

Figure 9: Excess pore pressure depiction at 150s and 300s of analysis: $Case A$, 40%, 60% and 80% relative density. Five contour lines are plotted, Δu = [100kPa-300kPa] split in equal increments.

Stress paths The stress response of soil for *Case A*, in terms of $\tau_{xz} - \gamma_{xz}$ plots for DR=40% and 80% can can be seen in (Figures 10, 11) while the response for DR=60% can be seen in the Appendix (Figure 41). The high level of induced non-linearity is clearly evident as in all control points for DR= 40%, the soil liquefies at some point during the analysis while afterwards shear stress is carried by sand cyclic mobility. The loosest soil (Figure 10), seems to liquefy after a very small amount of cycles while for the densest one 11 shear stress during the analysis is mostly undertaken by the so-called butterfly orbits without ever reaching liquefaction. For the top control points $A_{L,R}$ a burst of mean effective stress and subsequently shear stress capacity is observed which is related to the rogue wave impact.

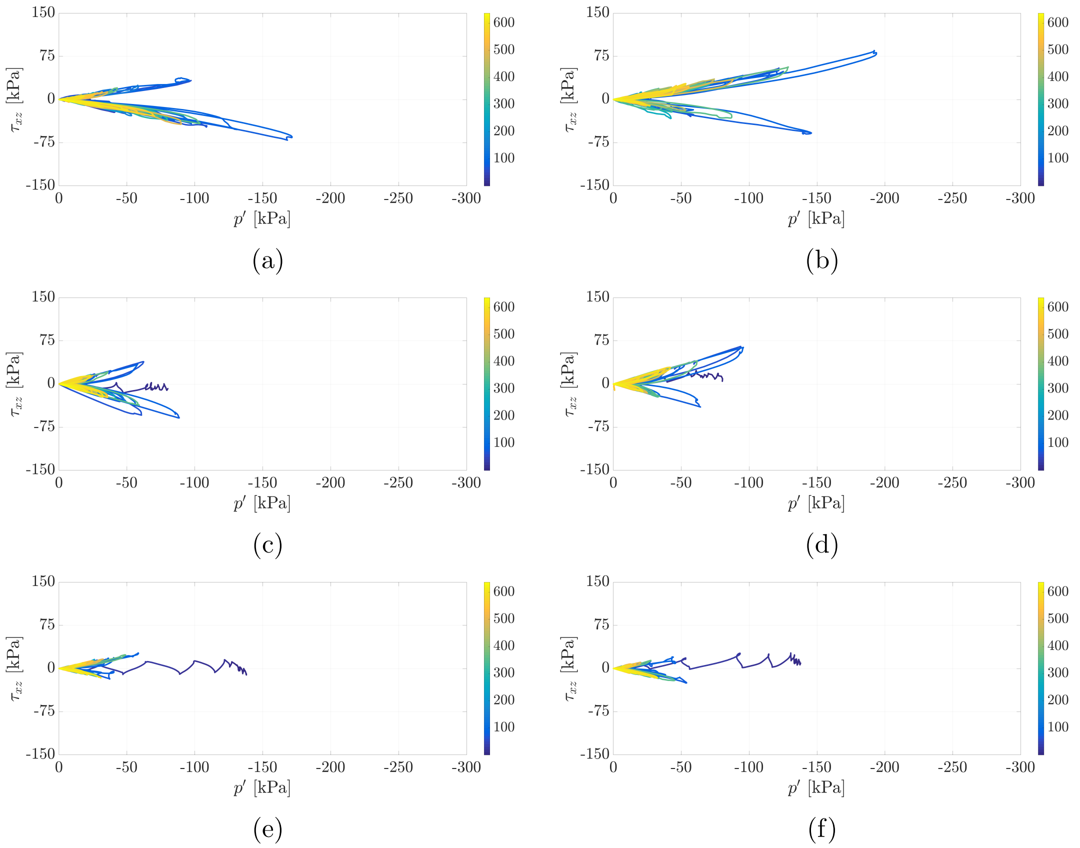

Figure 10: Stress paths of $\tau_{xz} - p'$ for all control points, DR=40% : (a) A_L, (b) A_R, (c)B_L, (d) B_R, (e)C_L, (f) C_R. The colorbars indicate time.

Stress-strain Stress strain response of the soil at the control point is depicted by $\tau_{xz} - \gamma_{xz}$ plots seen in (Figures 12 , 13), DR=60% is located in the Appendix (Figure 42). It can be seen that the soil with 40% relative density accumulates more than double the strain the soil of 80% relative density does at the control points. This is attributed to the soil being less stiff during the loading part of a cycle but also by accumulating more strains throughout the whole unloading reloading process. The extensive accumulation of strains observed in the loosest soil results in high pile-head deflections and rotations.

Void ratio effects for Case A, do not present special interest as undrained conditions are dominant for that level of permeability and loading. They are further discussed in (Appendix A.6)

3.2.2 Monopile head response

During the analysis, the monopile head displacement was recorded which can be seen in (Figure 14). Wide differences can be seen between *Cases* $A - B$ which examine heavy storm response. Although loads are higher for *Case* A, monopile head displacement is much more pronounced relative to the load difference, exposing the fact that the stiffness of the monopile is reaching the plateau of its non-linear regime. In all cases the 40% relative density soil results in bigger displacements accompanied with larger amplitude oscillations around the mean displacement reached. In case B a slow but progressive increase in monopile head displacement is observed.

For $CaseA$ the displacement plot resembles a sawtooth with peaks located at times of strong loading e.g. rogue wave at ($\approx 70'$) and other big wave impacts at ($\approx 260'$), ($\approx 350'$) etc. That effect

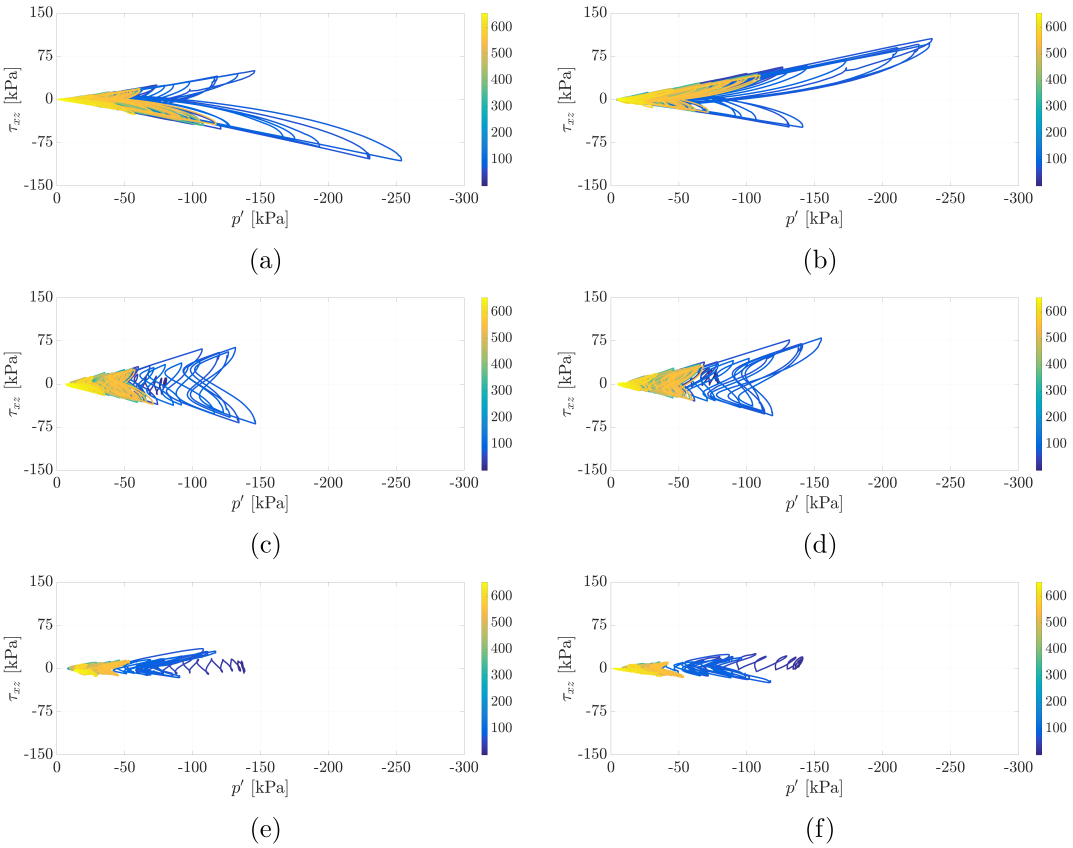

Figure 11: Stress paths of $\tau_{xz} - p'$ for all control points, DR=80% : (a) A_L, (b) A_R, (c)B_L, (d) B_R, (e)C_L, (f) C_R. The colorbars indicate time.

could be justified by considering that a during a strong wave impact, an increasingly bigger part of the rightward side of the mesh is plastified resulting in larger displacements. Subsequent loading of lower amplitude does not suffice to cause further plasticity while monopile head displacement does not return to its previous level due to non-recoverable plastic strains achieved during the impact but also due to the fact that the damping applied, does not suffice to consume the energy inserted into the system by the impact in the small time frame between two consequent strong wave impacts.

Lateral (K_L) and rotational (K_R) stiffness. Moment rotation response at the monopile head for *Cases A*, *B* can be seen in (Figure 15) along with an estimation of initial stiffness but also at approximately 600s of analysis. The added flexibility for the loosest soil is obvious from the slope inclination of dashed lines (Figure 15) which indicate stiffness, but also from the overall response. The plots for the loosest soils are much wider indicating an accumulation of rotation, but also shorter indicating lower stress on the structure which is expected.

Higher loss of stiffness is recorder throughout an analysis on looser soils than on dense ones. During the estimation of initial stiffness $K_{L-R,0}$ the pore pressure field is not fully developed and thus this effect can be attributed to the pronounced tendency of loose soils to accumulate pore pressures relative to the dense ones. Comparing soils with 60% and 80% relative densities we observe that although rotational stiffness is slightly degraded from the densest to the looser soil, lateral stiffness displays a 50% drop, (Table4). As through such an analysis, we cannot isolate the effect of moment and force on displacement and rotation to obtain the cross-coupling spring stiffness, that difference could be attributed to a second order effect of the rotational stiffness on

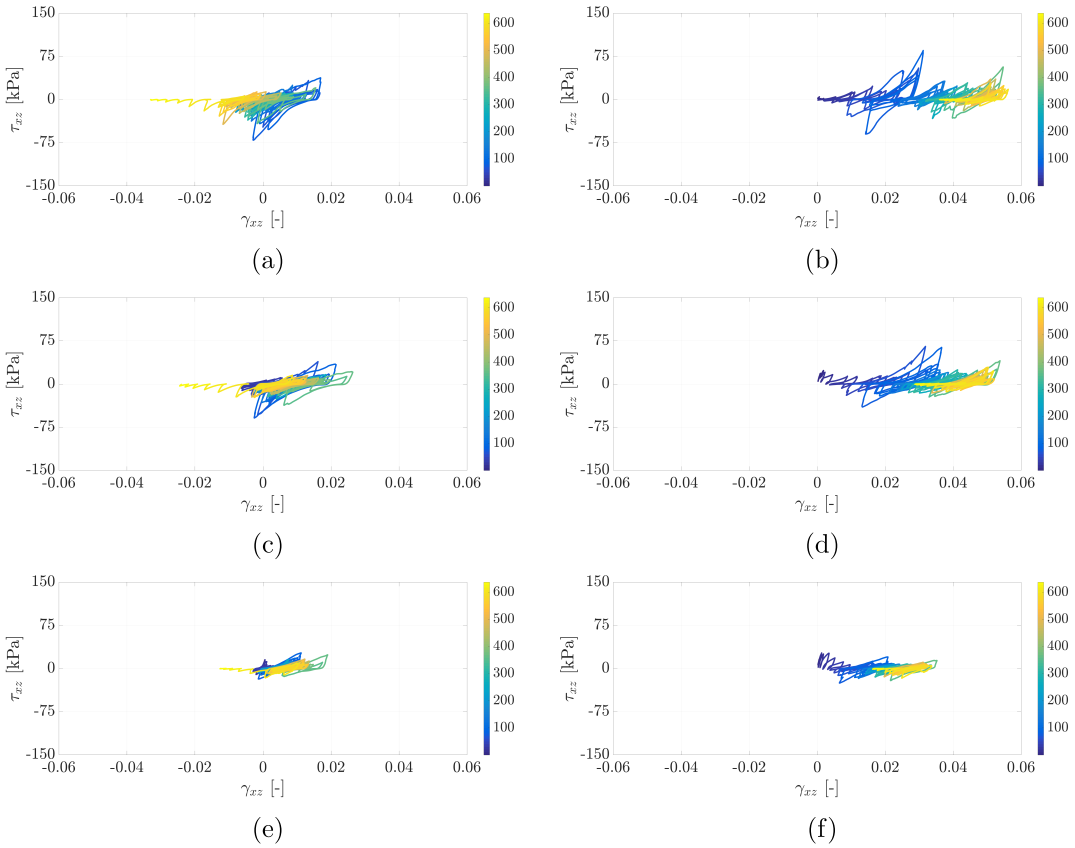

Figure 12: Stress-strain $\tau_{xz} - \gamma_{xz}$ for all control points, DR=40% : (a) A_L, (b) A_R, (c)B_L, (d) B_R, (e)C_L, (f) C_R. The colorbars indicate time.

lateral displacement.

3.3 OWT natural frequency

3.3.1 Simplified analytical models

The work of (Arany et al., 2015) was incorporated in (Arany et al., 2017) and it resulted in an process for estimating the OWT's structural dimensions (tower and monopile) but also its expected frequency response. In this study, that procedure was utilized to extract the OWT's first natural frequency. The biggest part of the process is focused on predetermining the frequency response of the tower but also the added flexibility of the part of the monopile submerged into the sea (above the mudline). Since there was already a numerical representation of the structure, the fixed base natural frequency of the structure above the mudline was obtained though an eigen-analysis and was given as a direct input in the procedure proposed. In other words only the part that describes the soil's contribution was utilized.

To estimate the foundation stiffness, (Arany et al., 2017) suggests various formulations suggested by other researchers (Randolph, 1981; Shadlou and Bhattacharya, 2016; Gazetas, 1984; Pender, 1993; Poulos and Davis, 1980; Barber, 1953) while the results presented in (Table 5) are based on the first three. These formulations require input parameters to describe the soil and monopile stiffness. Soil is described by its stiffness at depth equal to 1 pile diameter, measured from the mudline, which was obtained by calculating the initial stiffness E_0 at the corresponding stress level. Preliminary tests conducted with the so-called E_{50} stiffness, which was obtained by performing trixial tests in *OpenSees* displayed higher discrepancy with the response which resulted

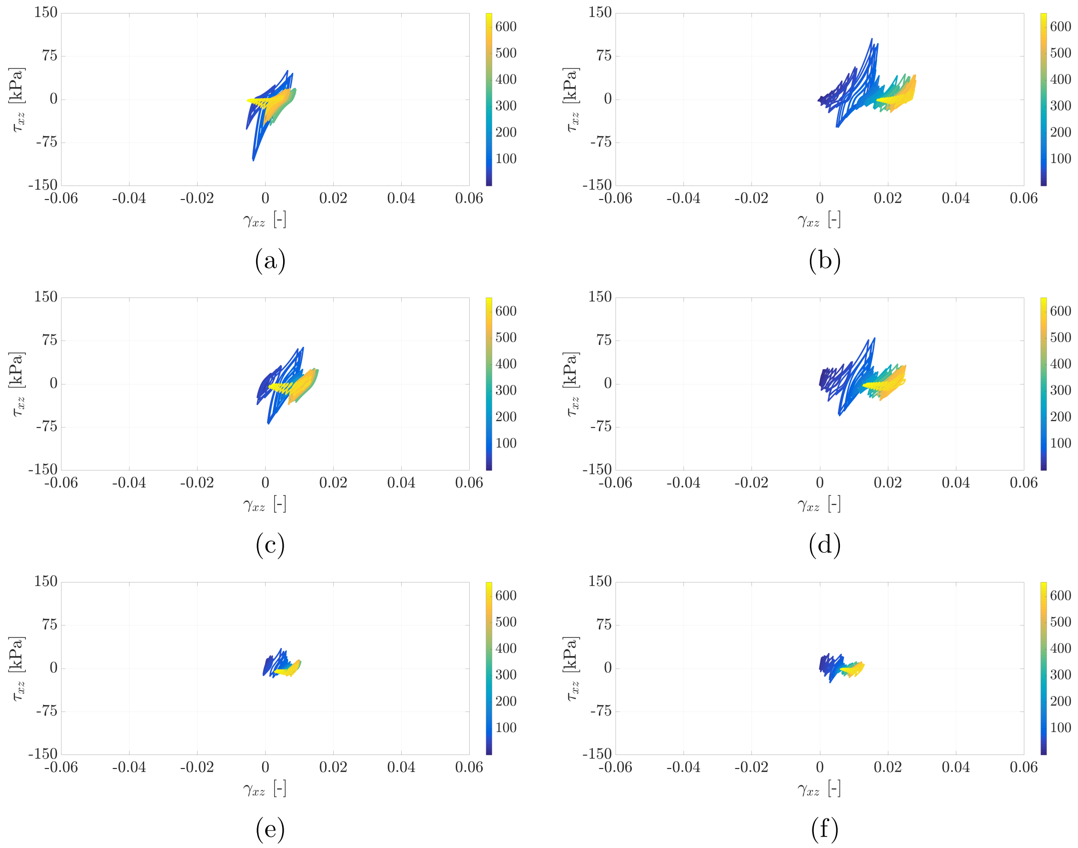

Figure 13: Stress-strain $\tau_{xz} - \gamma_{xz}$ for all control points, DR=80% : (a) A_L, (b) A_R, (c)B_L, (d) B_R, (e)C_L, (f) C_R. The colorbars indicate time.

from the analysis and thus are being neglected. The estimated frequencies can be seen in (Table 5).

Although such methodologies have undisputed value, they are based on oversimplified approximations of the soil which is the biggest source of uncertainty. Furthermore such models are unable to distinguish between different loading conditions (ambient excitation, production and storm loads) or predict shifts in natural frequency during storms whose effect on the lifetime of the offshore turbines is not yet well understood. All these uncertainties can be addressed by a 3D FEM simulation where the frequency response does not depend upon calibrating soil springs or p-y curves but results from solving the equations that describe the problem. This way the applicability of simplified solutions can be examined.

3.3.2 Stockwell transforms

As discussed in 2.5, in this study the S-transforms are employed so that the frequency content of the OWT's response over time could be estimated. The examined variable was the displacement of the hub over time where the amplitude of the harmonics was normalized over time to clear the figures from the unnecessary effects resulting from the varying displacement amplitude. The S-transform of the hub displacement time history can be seen for *Case A* in (Figure 16), *Case B* in (Figure 17) and for *Case C* in (Figure 18).

The results indicate a strong dependence of average frequency response on: (i) soil density, (ii) force frequency content and (iii) force amplitude. Overall for all cases the OWT resting on the densest soil (DR=80%) responds more rigidly with very few shifts in frequency content. For the DR=40% case, the frequency content of the response can be described as very unstable

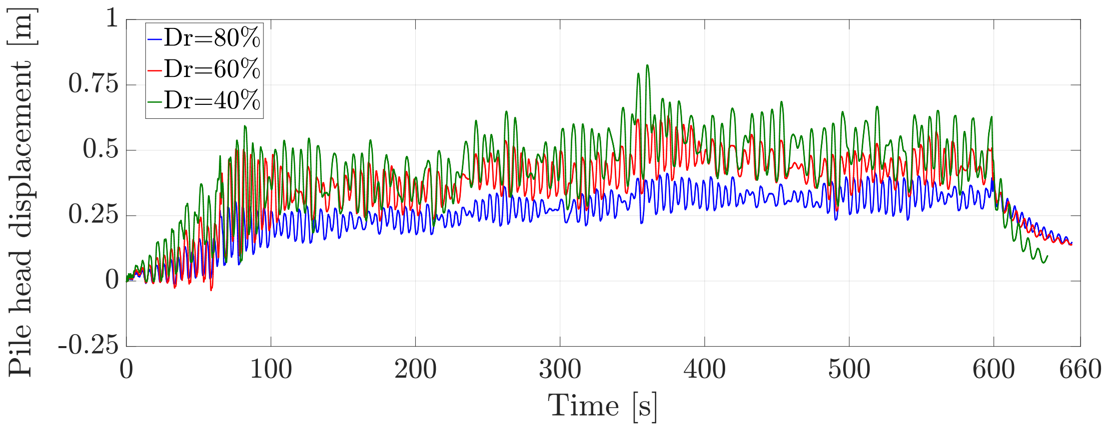

(a) *Case A*

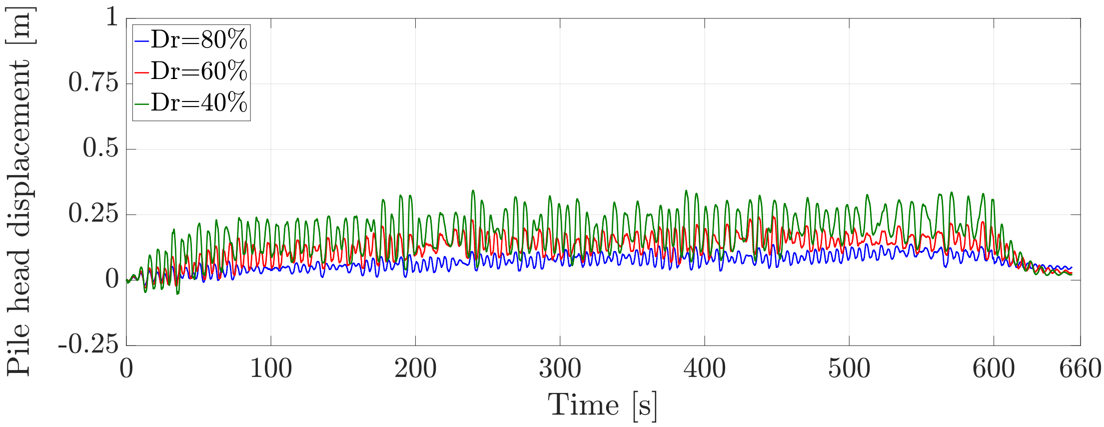

(b) *Case B*

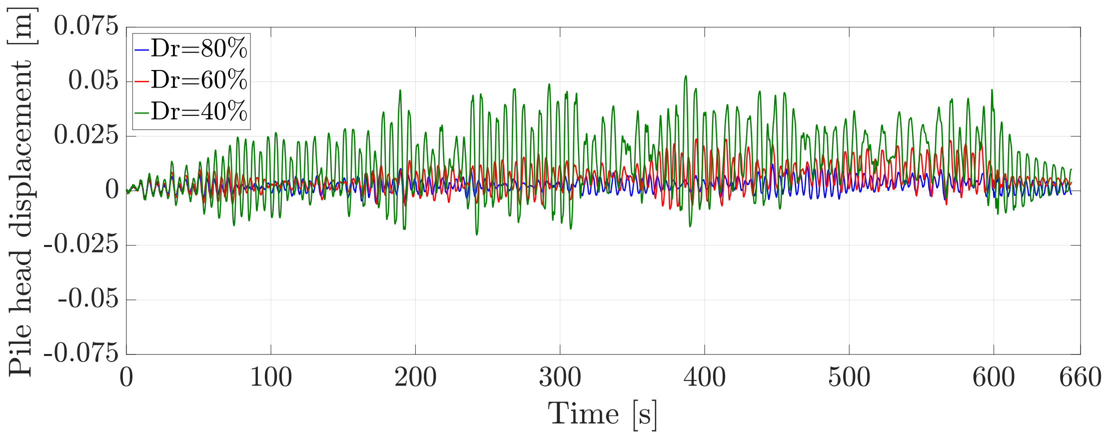

(c) *Case C*

Figure 14: Displacement of monopile head for: (a) *CaseA*, (b) *CaseB*, (C) *CaseC*.

with abrupt changes of frequency content. The case for DR=60% displays characteristics from both the aforementioned cases leaning closer to a more stable response. The abrupt changes in frequency content of the response match the frequency content of the force signal and result from an enhanced compliance of the foundation as soon as liquefaction in all control points is observed. Comparing the load signal from *Case A* (Figure 16a) with the response signal for the loosest soil (Figure 16d), we observe that for all sudden drops of frequency, strong loads with the exact same

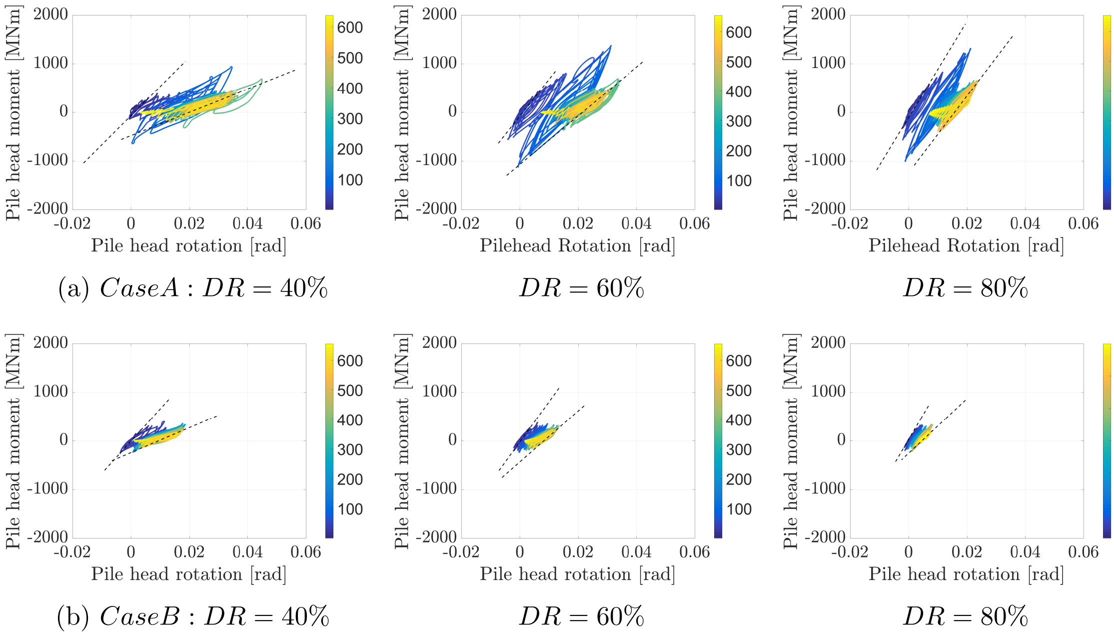

(a) $CaseA : DR = 40\%$ $DR = 60\%$ $DR = 80\%$

(b) $CaseB : DR = 40\%$ $DR = 60\%$ $DR = 80\%$

Figure 15: Moment-rotation plots for *Cases A, B* at the pile head: colorbars indicate time while dashed lines indicate rotational (K_R) stiffness at approximately 600s of analysis.

frequency content at the exact same time are applied to the structure. One could say that there is an imprint of the S-transform of the loads upon the response for the loosest soil. That effect is strongly highlighted for t=200, 300 and 450 seconds.

The effect of loading amplitude can be isolated by examining the differences between *Case B* (Figure 17) and *Case C* (Figure 18). In those cases the same loads were applied with the only difference being the amplitude. For *Case C* the loads applied were divided by five. It can be seen that overall stronger load amplitude results in lower response frequencies. The effect is more profound for the loosest soil case where even though a decreasing trend is observed, it seems that the hub starts to obey the frequency of the loads applied after approximately 300s. During the first part of the analysis, although soil plasticity is increasing, the stiffness of the soil domain is not that low to render the structure compliant with the excitation.

Very interesting remarks can be made by looking at the excess pore pressure evolution at the control points for *Case C* (Figure 20). It can be seen that the aforementioned non stable state coincides with the time that $u \approx p$ at control points $C_{L,R}$. From that moment the soil around the monopile and across all of its embedment depth is operating under very low shear strength and stiffness resulting in very flexible and compliant foundation. To obtain further insight on this matter, the pore pressure field for DR=40% for *Cases B, C* is depicted in (Figure 21). The figure depicts the excess pore pressure at 150s and 300s to visualize globally the pore pressure field. It can be seen that at 300s high excess pore pressures are manifesting close to the monopile tip. Comparing the global outlook of the pore pressures and the control point behaviour it can be deducted that foundation instability is reached as soon as the whole foundation, including the tip of the monopile, operates under low stiffness and capacity caused by transient excess pore pressures. This point is in agreement with scepticism around neglecting the monopile's tip contribution to the overall capacity. It is also worth mentioning that in contrast with the stronger load cases, in *Case C*, all the control points experience an increase in pore pressure due to the low amount of shearing experienced by the soil.

Another interesting remark has to do with the observed declining trend of the 1^{st} eigen-frequency for the DR=40% sand seen in (Figure 18). The declining trend points to a softer soil

Table 4: Lateral (K_L) and rotational (K_R) pile head stiffness at t≈ $0s$ and t≈ $600s$ of analysis for *Cases A, B*.

		Sand relative density		
Case	Property	40%	60%	80%
Case A	$K_{L,0}$ $[MNm^{-1}]$	44.53	63.74	114.81
	$K_{R,0}$ $[MNmrad^{-1}]$	60346.21	74443.56	98894.34
	K_L $[MNm^{-1}]$	35.51	45.11	95.22
	K_R $[MNmrad^{-1}]$	34411.21	48011.33	79057.36
Case B	$K_{L,0}$ $[MNm^{-1}]$	84.78	139.25	167.93
	$K_{R,0}$ $[MNmrad^{-1}]$	67168.11	83516.49	10443.05
	K_L $[MNm^{-1}]$	26.13	46.97	93.63
	K_R $[MNmrad^{-1}]$	25674.52	50934.32	59726.39

Table 5: Estimation of the 1^{st} natural frequency following (Arany et al., 2017) along with the soils stiffness parameters used. **S**, **R** stand for slender and rigid monopiles.

Property	Values			Soil formulae
Relative density	40%	60%	80%	
$E_{0,z=Dp}$	56.9 MPa	63.4MPa	71.3 MPa	
Soil stiffness formulation	0.194 Hz	0.195 Hz	0.196 Hz	(Randolph, 1981), **S**
	0.197 Hz	0.198 Hz	0.199 Hz	(Gazetas, 1984), **S**
	0.189 Hz	0.190 Hz	0.192 Hz	(Shadlou and Bhattacharya, 2016), **S**
	0.208 Hz	0.21 Hz	0.213 Hz	(Shadlou and Bhattacharya, 2016), **R**

medium as the structure is elastic and remains unaffected from the loads applied. The change of relative density during this analysis at the control points was negligible. Furthermore, in case change of relative density was recorded, such a loose sand under the loads applied would only get denser resulting in a denser medium. The only component that transient loading is affecting and can have an impact on the stiffness of the medium is the pore pressure. As such pore pressure evolution can be regarded as an agent of momentary drops of the fundamental frequency which was also hypothesised by (Kallehave et al., 2012a).

3.3.3 Natural frequency: comparing analysis results with simplified formulas predictions

Comparison between the analytical model's predictions and the frequency response calculated from the analysis can be seen in (Figures 16, 17, 18, 19). The red dashed lines depicting the compliant base response $CB_{analytical}$ were drawn based on the formulation that provided the closest fit on the observed response. As such it seems that the formulation of (Gazetas, 1984) is the most applicable for the cases examined especially for the low loading *Case C*. One should note that estimating the frequency response during low loading is important as fatigue damage takes place at low wind speeds.

Good agreement can be seen also with the predictions made using the formulations of (Randolph, 1981) which along with the formulation from (Poulos and Davis, 1980) were deemed as most applicable by (Arany et al., 2017). Furthermore in the same work it was argued that the

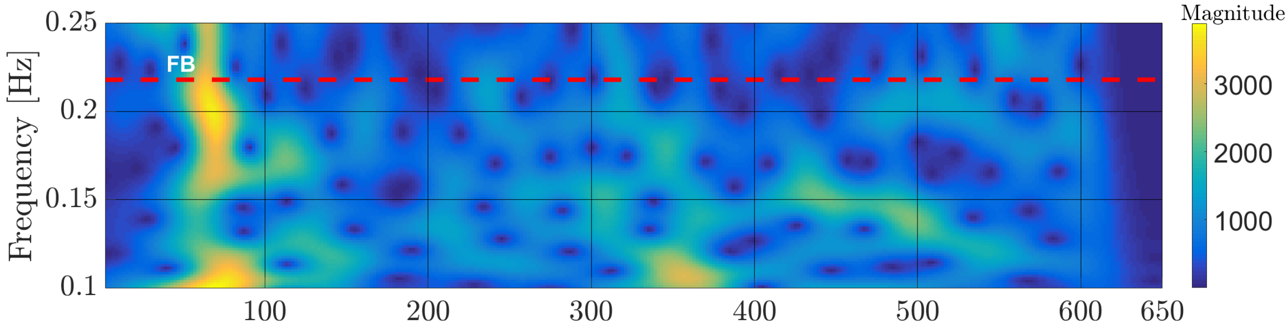

(a) *Loading*

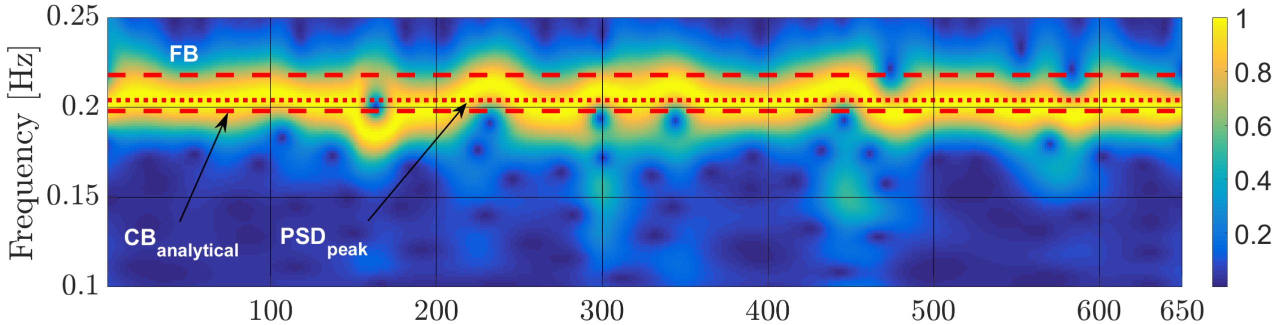

(b) $Dr = 80\%,\ PSD_{peak} = 0.203\ [Hz],\ CB_{analytical} = 0.199\ [Hz]$ by (Gazetas, 1984).

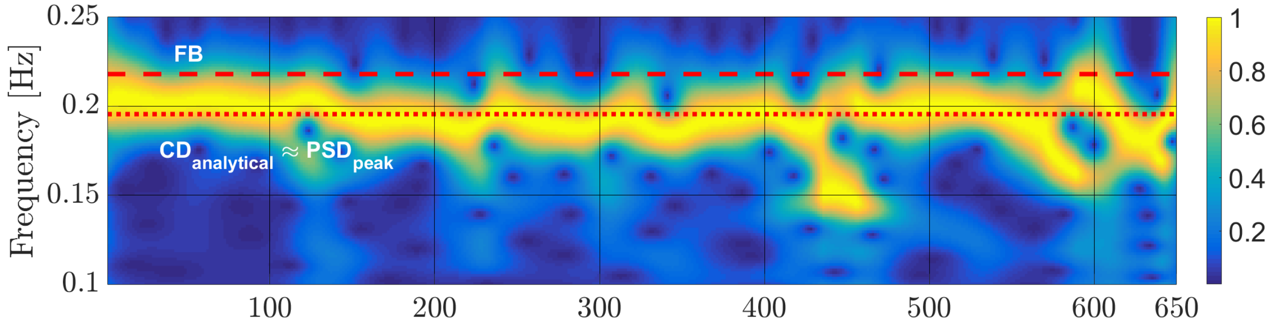

(c) $Dr = 60\%,\ PSD_{peak} = 0.196\ [Hz],\ CB_{analytical} = 0.195\ [Hz]$ by (Randolph, 1981).

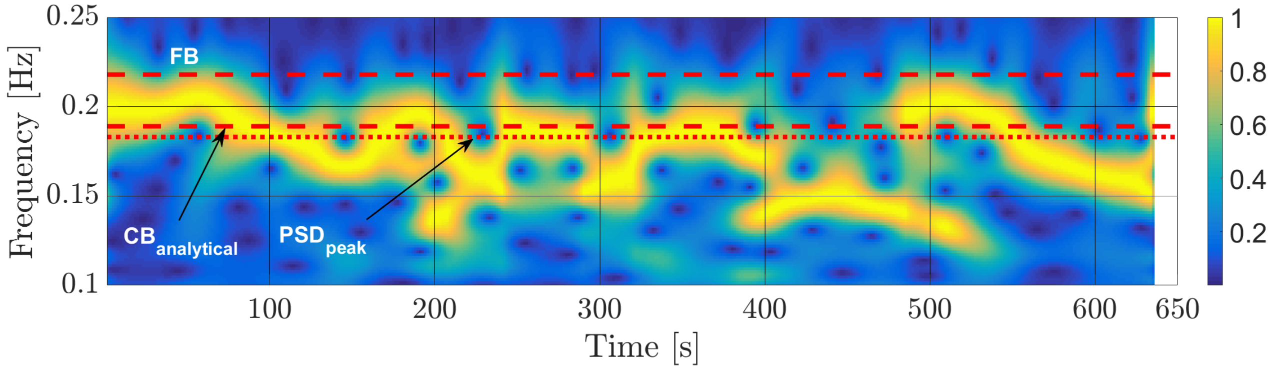

(d) $Dr = 40\%,\ PSD_{peak} = 0.183\ [Hz],\ CB_{analytical} = 0.189\ [Hz]$ by (Shadlou and Bhattacharya, 2016).

Figure 16: S-transforms of hub displacement time history for *Case A*: Plots (a) DR=40%, (b) DR=60%, (c) DR=80% are normalized and (d) represents the non-normalized frequency content of the loads. $FB = 0.218\ [Hz]$, $= 1^{st}$ natural frequency for fixed base structure, $CB_{analytical} =$ predicted frequency using the work of (Arany et al., 2017) and stands for compliant base. The foundation stiffness for each prediction was based on studies seen under each plot, the best prediction is shown. $PSD_{peak} =$ the frequency at which the peak power spectral density of the signal is found seen in (Figure 19). Colorbars indicate magnitude of each signal's harmonics.

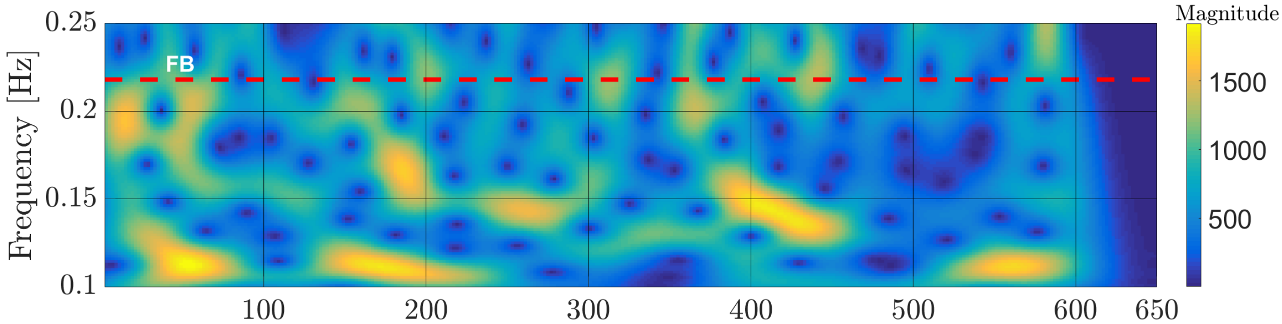

(a) *Loading*

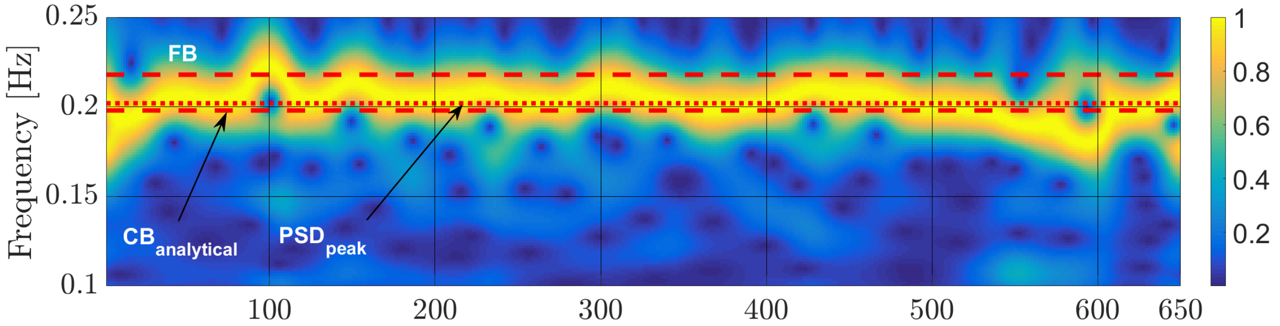

(b) $Dr = 80\%,\ PSD_{peak} = 0.202\ [Hz],\ CB_{analytical} = 0.199\ [Hz]$ by (Gazetas, 1984).

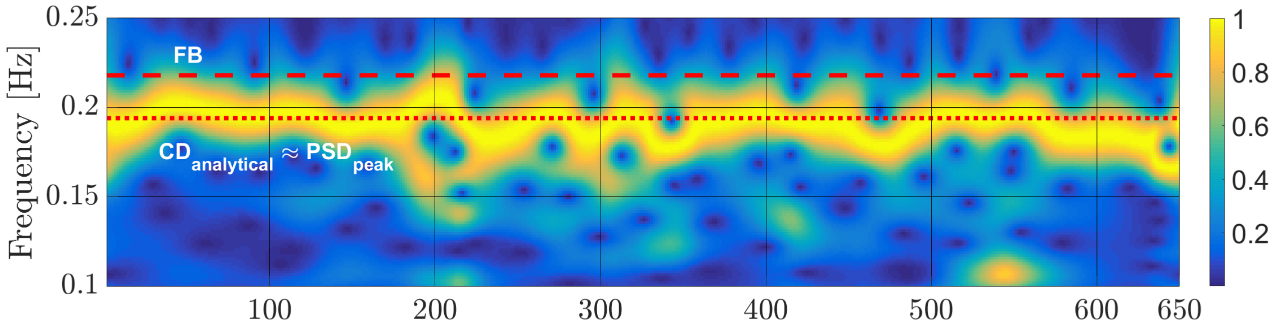

(c) $Dr = 60\%,\ PSD_{peak} = 0.192\ [Hz],\ CB_{analytical} = 0.195\ [Hz]$ by (Randolph, 1981).

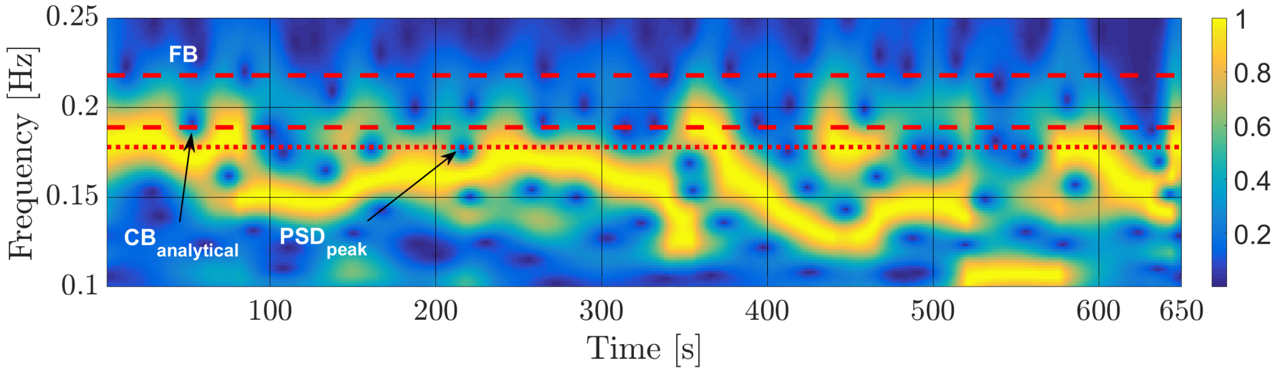

(d) $Dr = 40\%,\ PSD_{peak} = 0.178\ [Hz],\ CB_{analytical} = 0.189\ [Hz]$ by (Shadlou and Bhattacharya, 2016).

Figure 17: S-transforms of hub displacement time history for *Case B*: Plots (a) DR=40%, (b) DR=60%, (c) DR=80% are normalized and (d) represents the non-normalized frequency content of the loads. $FB = 0.218\ [Hz],\ = 1^{st}$ natural frequency for fixed base structure, $CB_{analytical}$ = predicted frequency using the work of (Arany et al., 2017) and stands for compliant base. The foundation stiffness for each prediction was based on studies seen under each plot, the best prediction is shown. PSD_{peak} = the frequency at which the peak power spectral density of the signal is found seen in (Figure 19). Colorbars indicate magnitude of each signal's harmonics.

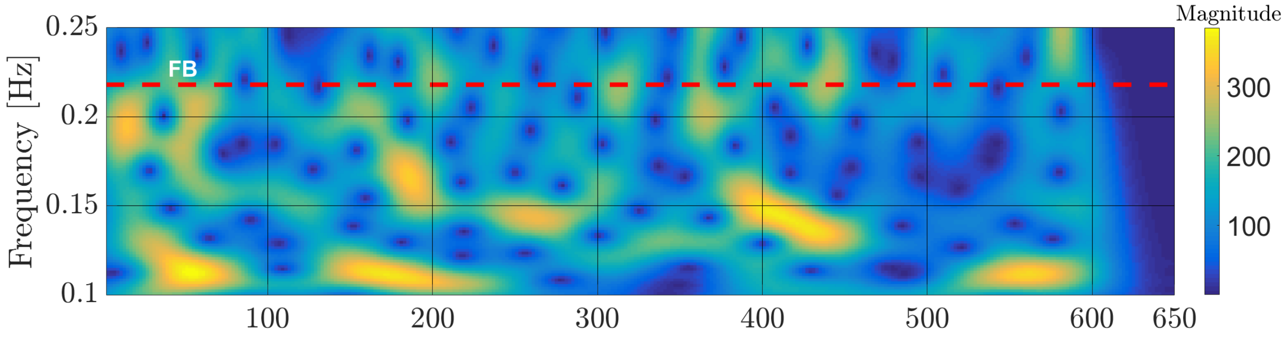

(a) *Loading*

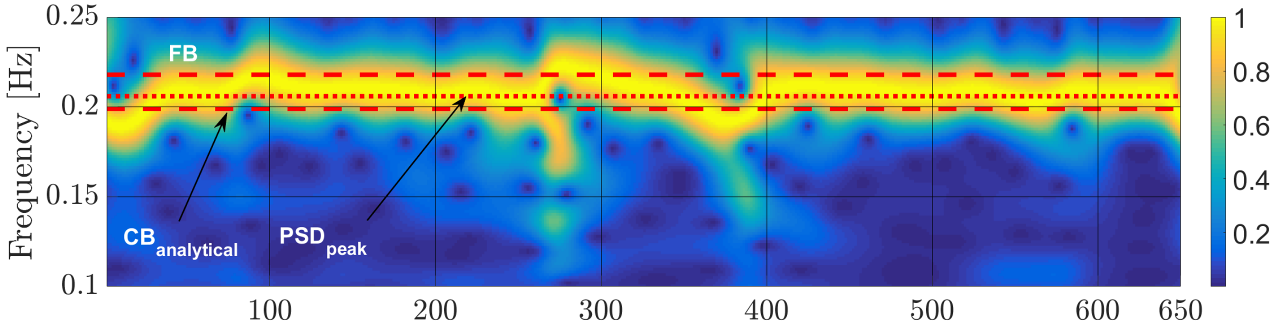

(b) $Dr = 80\%,\ PSD_{peak} = 0.206\ [Hz],\ CB_{analytical} = 0.199\ [Hz]$ by (Gazetas, 1984).

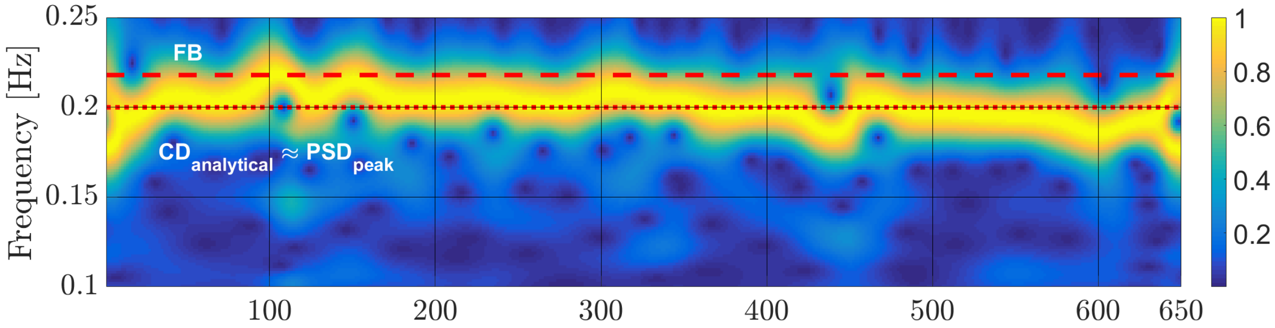

(c) $Dr = 60\%,\ PSD_{peak} = 0.201\ [Hz],\ CB_{analytical} = 0.198\ [Hz]$ by (Gazetas, 1984).

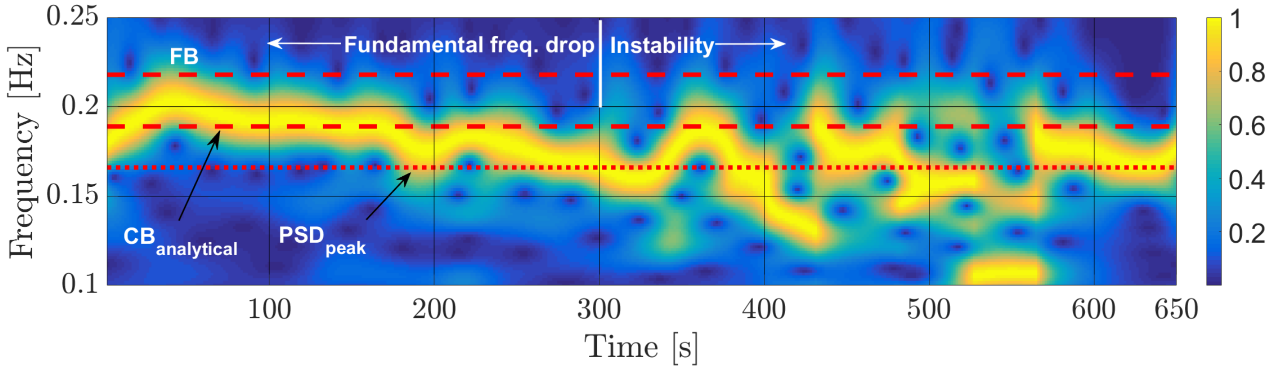

(d) $Dr = 40\%,\ PSD_{peak} = 0.166\ [Hz],\ CB_{analytical} = 0.189\ [Hz]$ by (Shadlou and Bhattacharya, 2016).

Figure 18: S-transforms of hub displacement time history for *Case C*: Plots (a) DR=40%, (b) DR=60%, (c) DR=80% are normalized and (d) represents the non-normalized frequency content of the loads. $FB = 0.218\ [Hz]$, $= 1^{st}$ natural frequency for fixed base structure, $CB_{analytical} =$ predicted frequency using the work of (Arany et al., 2017) and stands for compliant base. The foundation stiffness for each prediction was based on studies seen under each plot, the best prediction is shown. $PSD_{peak} =$ the frequency at which the peak power spectral density of the signal is found seen in (Figure 19). Colorbars indicate magnitude of each signal's harmonics.

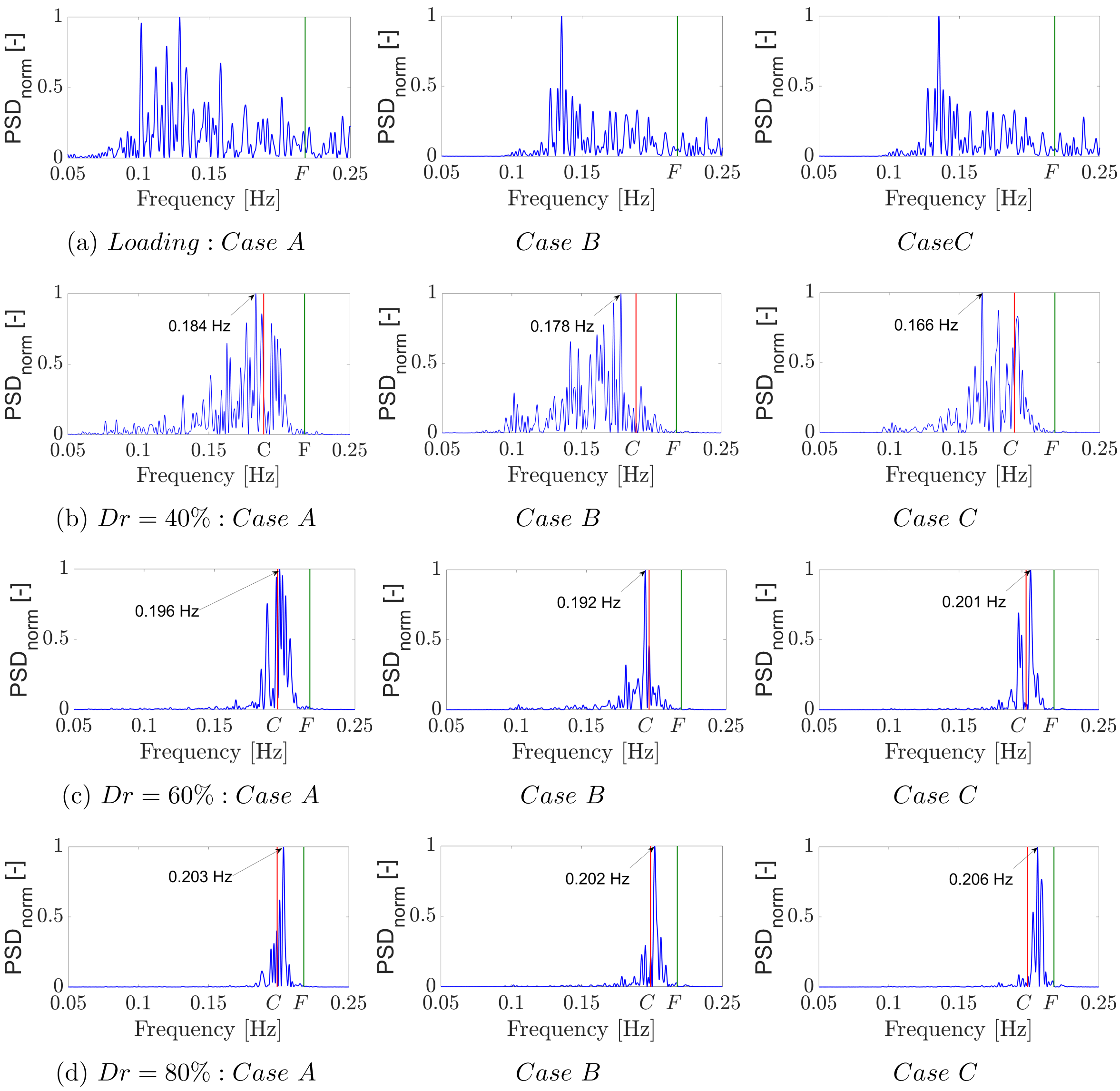

Figure 19: Normalized Power Spectral Density: (a) Loading, (b) Dr=40%, (c) Dr=60%,(d) Dr=80%. $F = 0.218\ [Hz], = 1^{st}$ natural frequency for fixed base structure, C = estimated frequency according to (Arany et al., 2017) and stands for compliant base. Soil was introduced into the predictions based on the work of (Gazetas, 1984; Shadlou and Bhattacharya, 2016; Randolph, 1981). For more details see (Figures 16, 17, 18).

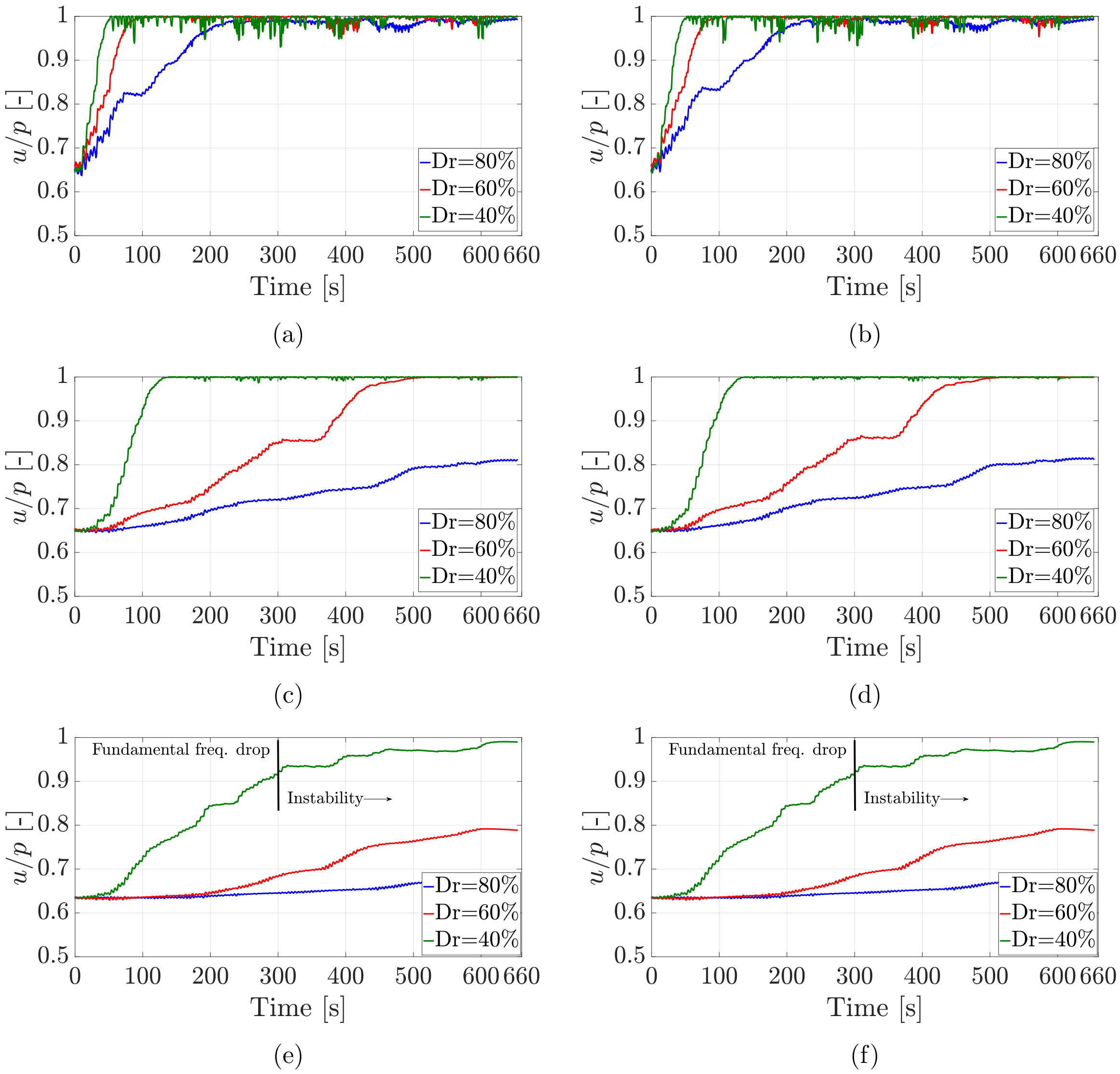

Figure 20: Pore pressure over mean confinement stress versus time in all control points for all relative densities for $CaseC$: (a) A_L, (b) A_R, (c)B_L, (d) B_R, (e)C_L, (f) C_R. Instability and frequency drop comments refer to the Dr=40% case.

slender pile formulations produce better approximations of the structure's eigen-frequency than the formulae for stocky piles, which is in complete agreement in what was found through this study as seen in (Table 5) compared with (Figures 16, 17, 18, 19). An overview of the calculations needed to estimate the natural frequency can be seen in the Appendix (A.5).

Very satisfactory results seem to be obtained when comparing the predictions of these simplified formulations versus the actual frequency content of the response. The best fit predictions are achieved for the soils with DR = 60% and 80% which are the most realistic designs. In those cases it seems that the simplified formulations serve as a lower bound prediction for the overall response.

Fourier Transforms The averaged frequency content of the hub displacement is displayed via the Fourier transform, (Figure 19). As observed the loads applied are rich frequency content exciting a wide band of frequencies. The profound effect of soil density on the frequency content of the response is undeniable. While for DR=80% the response seems unaffected by the lower

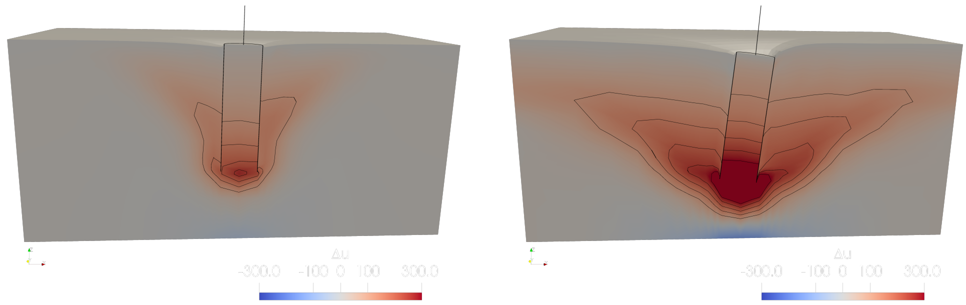

(a) $150s$: $Case A$ $Case B$

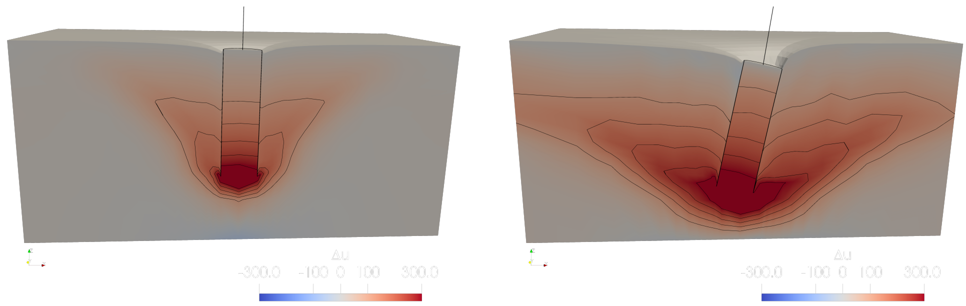

(b) $300s$: $Case A$ $Case B$

Figure 21: Excess pore pressure depiction at 150s and 300s of analysis: *Cases B*, *C*, and 40% relative density. Five contour lines are plotted, Δu = [100kPa-300kPa] split in equal increments.

frequency content of the loads that is clearly not the case for the loosest soil configuration where high harmonics amplitude is to be found in lower frequencies. The information that we can see in such a plot could also be provided by ploting the frequency response function which is the ratio between the acceleration PSD and the force excitation PSD. While such figures where constructed they seemed harder to interpret and where not shared.

It becomes clear by interpreting the input's frequency content versus the output's, that the frequency recorded, for the DR=60% and 80% is the resonance frequency. The input signal poses an anemic excitation on the frequencies that most of the output content is located which implies the existence of dynamic magnification which is indicative of resonance response.

3.4 Frequency drops

During a storm, pore pressures build up and soil behaves less stiff. That results in a more flexible foundation which should lead in a drop of the system's 1_{st} eigen-frequency. A few attempts are found in literature shedding light into the matter by monitoring an OWT's response over a long period of time. (Kallehave et al., 2015b) presents and discusses the observed dynamic behaviour of a 2.3MW OWT located in dense to very dense sand deposits, which was monitored for a period of 2.5 years subjected to normal operating conditions and one large storm event. The OWT is resting upon a 18.4m length monopile with a diameter of 3.9m.

In the same study, the fundamental frequency was estimated by converting the time signal of the recorded acceleration on the rotor-nacelle-assembly (RNA) into the frequency domain in order to obtain the peak spectral density in the computed time. The authors consider the natural frequency of the first mode of the OWT by averaging the peaks of spectral density plots obtained over a 2.5 month-period where, according to the authors, normal operating conditions applied.

In *Case C* the loads of *Case B* were divided by five to constitute a low loading case. It is rather vague to compare the level of non-linearity of the 2.5 month period on which the 1_{st} natural period seen in (Figure 22) was estimated with *Case C* as differences in soil conditions and load composition are found. Furthermore foundation sizes vary in terms of L/D ratio, 4.72 for (Kallehave et al., 2015b) to 3.38 found in this study. What it can be said is, that these cases (2.5 month period of normal operating conditions and *Case C*) constitute two loading conditions where low level of non-linearity is induced. As the S-trasforms for all loading cases are calculated, there was the possibility to extract the outcrop of the maximum normalized amplitude of the harmonics seen in (Figures 16, 17, 18) and obtain its mean. As the configuration with 80% relative density fits best to the soil conditions discussed by (Kallehave et al., 2015b) but also is the one less affected by the loading frequency content in this study, the mean of the peak amplitude was calculated to estimate an average natural frequency following a similar approach as discussed by (Kallehave et al., 2015b) and refereed to, in (Figure 22) as $f_{0.Int.P1}$. The base natural frequency for this study f_0 was obtained by averaging the frequency of the peak amplitude of the response for *Case C*.

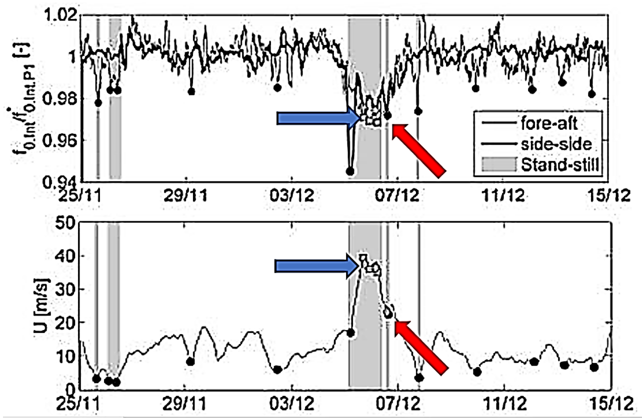

Figure 22: Obtained from (Kallehave et al., 2015b): Short term observations during the strong storm event. Top figure: the fundamental frequency in the fore-aft and side-side direction normalized to the mean observed frequency under normal operating conditions, bottom figure: the wind speed. The arrows indicate the points (frequency drop and wind velocity) at which the strong wind measurements compared in (Figure 23) are estimated. The gray area indicates that the rotor is feathered.

The same practise was followed for *Cases A, B*. As such the reference f_0 under low loading conditions was obtained from *Case C* and then it was compared with the average peak frequency content of the strong loading Cases A and B. In both these cases the rotor is feathered which is in agreement with (Figure 22) at the times analysed (red and blue arrows). It can be seen that the wind speed at the time of the measurements averaged a 23.3 m/s during the lower wind excitation (red arrow) and a 36 m/s wind speed during the stronger wind case, (blue arrow). Respectively at *Cases A, B* the average wind speed is 24 and 47 m/s. The calculated frequency drop of this study compared to the one from (Kallehave et al., 2015b) can be seen in (Figure 23). What we can observe is that in general frequency drops do not constitute a great risk with the current design practices. Under heavy storm loading, a mild effect on the frequency content is observed for well designed foundations. Furthermore, as seen, the drop of frequency that was estimated numerically in this study is very close to what is observed in the field prescribing further confidence that one is able to reliably estimate the response of such structures numerically.

The conclusion that can be drawn from the comparison of the frequency drops between the two studies is that:

- The expected frequency drop, in a well designed foundation, during a strong storm event is in the order of 2-3% and is mostly attributed to transient pore pressures as in these cases the void ratio was merely affected ;
- Frequency drops of the same order of magnitude were recorder numerically and by field

measurements for two separate occasions;

- It is pointless to judge formulations and methodologies like the one of (Arany et al., 2017) for not accounting the effect of storm events and cyclic loading as the 1-3% frequency drop observed, is way beyond their prescribed accuracy;

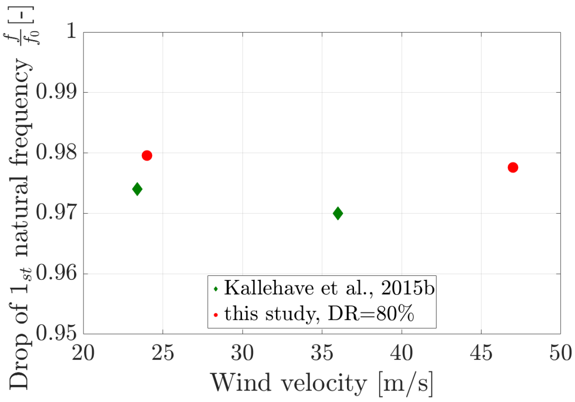

Figure 23: Frequency drop versus wind speed for parked OWTs (feathered rotors), comparing field test results obtained by (Kallehave et al., 2015b) for a 2.3 MW OWT and this study which examines an 8MW OWT.

3.5 Damping estimation

As mentioned according to (WindEnergie, 2005a; Versteijlen et al., 2011) soil damping is the most uncertain contributor to OWT damping. Although that is the case, estimation of soil damping is crucial to realize a cost effective design by accurate estimation of expected fatigue damage and response of OWTs during storm events. According to (Shirzadeh et al., 2013), the amplitude of vibrations at resonance are inversely proportional to the damping ratios. For that reason numerous studies have been undertaken seeking to evaluate soil contribution to damping mostly by performing emergency shut-downs refereed as the ′rotor-stop′ tests, (Versteijlen et al., 2011; Tarp-Johansen et al., 2009; Damgaard et al., 2012, 2013; Shirzadeh et al., 2013; Carswell et al., 2014).

(Shirzadeh et al., 2013) measured the frequencies and the damping values of fundamental modes for OWTs by performing both ambient excitation and overspeed stop tests. Ambient excitation tests are performed at wind speeds below the cut-in speed ($\approx 4.5\ m/s$) where the rotor is slowly rotating , while overspeed stops occurred at wind speeds in the threshold after the cut in speed allowing the wind turbine to start rotating. As in both test types, the damping was estimated at low wind conditions, where soil non-linearity and thus soil's contibution to damping was limited. The same methodology was reported by Devriendt et al. (2013) where the scope of the study was to estimate the so called offshore-damping. That is the overall damping excluding damping sources that exist onshore (aerodynamic damping, damping due to vortex shedding or damping form installed dampers).

(Damgaard et al., 2012) conducted 'rotor-stop' tests at wind velocities ranging between 3-13m/s. Furthermore it was reported that a decreasing total system damping with increasing wind speed was observed, which was attributed to higher contribution of the tower oscillation damper at higher accelerations.

In the work of (Versteijlen et al., 2011), the rotor stop tests were conducted in two phases. Wind speeds occurring prior the rotor stop were 11 m/s and 19.7 m/s respectively. During the second phase, due to the high wind velocity, the blades were partly pitched out to reduce loads on the structure. That small difference in the pitch angle resulted in lower blade excitation for the second phase even though the wind speeds were lower. One though should consider that lower hub wind loads do not constitute a milder loading case, as the wave loads for the higher wind velocity case are expected to be augmented.

It is clear that most rotor stop tests recorded in literature have occurred at low wind speeds, except from (Versteijlen et al., 2011), where the turbine is either under power production or feathered. There are no measurements of soil damping available through heavy storm conditions where soil damping is expected to be at its peak though enhanced hysteretic response. It can be understood that experimentally rotor stops are non feasible under such conditions as the wind speeds have already surpassed the cut-off speed resulting in parked turbines. Rotor-stops throughout storms though, can be achieved by numerical modelling as loads are a direct input of the user. As such this study is tailored to fill that void by investigating soil damping values under extreme non-linear soil behaviour. Rotor stops have been numerically performed by removing all applied loads after 600 seconds of analysis. Afterwards the turbine performed a free vibration for 60 seconds. The artificial damping applied to the structure during the analysis can be seen in 2.3 and is expected to have a minor impact on the results.

Total system damping was estimated by fitting the logarithmic decrement on the acceleration of the hub during the free vibration regime. The acceleration signal was filtered from the effects of higher modes with a low pass filter set at 0.35 Hz. Both acceleration and displacement signals were employed to estimate damping. Plots of displacement are a superposition of a decaying trend of the hub returning towards its initial position and the oscillations around that trend. As the logarithmic decrement method is applied on the decaying oscillations the non-oscillating trend of the response was removed in order to fit the exponential function. Finally the results where based on the acceleration response as the way of filtering that returning trend of displacements had a great effect on the calculated values.

Results can be seen in (Table 6). *Cases A*, *B* are displayed together as there was a minor difference in the estimated damping. It must be noted that for the loosest soil examined, the response was quite different from the familiar response of the elastic 1-dof system under free vibration in contrast to the case of DR=60% and 80% (Figure 24). Keeping in mind that the foundation was designed for soil conditions in between 60%-80% relative density the values of critical damping obtained are well within what is estimated in literature (Table 7). Assuming that total damping is a linear combination of independently modelled damping sources (Tarp-Johansen et al., 2009; Shirzadeh et al., 2013; Damgaard et al., 2012; Carswell et al., 2014) one should subtract a value of approximately 0.2% to obtain the soil critical damping. This approach though is rather questionable and ambiguous as in this study damping was subscribed at the affected members (material damping only in steel sections) specifically and not on the whole analysis domain where it would have been more relevant.

Load level effect The effect of loading level is evident, as in *Case C* damping values drastically decrease. As in *Case C* the load creation process was not based on wind records, we are unable to directly prescribe a wind speed that would cause such non-linearity but it should be considered as a soft loading case. Besides the cases examined in this study, the load effect can also be distinguished in (Table 7) between all cases reported in literature. Wind velocity can serve as a control point for a rough comparison between the loads applied. This study which examines rotor stop at wind speeds of 24m/s and higher, estimated the highest contribution of soil to damping, followed by (Versteijlen et al., 2011), (Damgaard et al., 2012) and (Shirzadeh et al., 2013). In all the aforementioned cases lower wind speeds resulted in lower foundation damping.

It must be noted that the observed soil damping is mostly attributed to the hysteretic soil behaviour as radiation damping is deemed negligible for frequencies lower than 1Hz (Tarp-Johansen et al., 2009; Damgaard et al., 2013; WindEnergie, 2005a). Furthermore a strong dependency of

Table 6: Total critical damping estimated from applying the logarithmic decrement on hub acceleration after load-stop. To obtain a lower bound for soil's contribution to critical damping one must subtract 0.19% from the displayed values.

Sand relative density		40%	60%			80%
Permeability (m/s)		10^{-5}	10^{-4}	10^{-5}	10^{-6}	10^{-5}
Loading	Case A-B	$\zeta \approx 7.7\%$	$\zeta \approx 5.4\%$	$\zeta \approx 5.15\%$	$\zeta \approx 5.9\%$	$\zeta \approx 2.2\%$
Scenario	Case C	$\zeta \approx 2.9\%$	$\zeta \approx 0.79\%$	$\zeta \approx 1.3\%$	$\zeta \approx 2.3\%$	$\zeta \approx 0.76\%$

soil damping on permeability exclusively for *Case C* is observed. This will be discussed in detail in the next section.

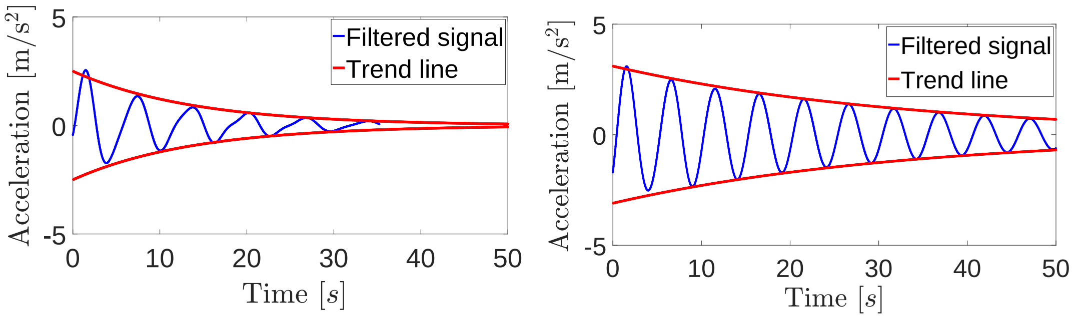

(a) DR=40% (b) DR=80%

Figure 24: Critical damping estimation by fitting of logarithmic decrement upon hub acceleration over time for *Case A*, Dr=40% and 80%.

3.6 Permeability effects

A set of analysis were conducted to establish the effect of permeability on the total system response (Table 3). No significant effect on global response has been reported by (Corciulo et al., 2017), who performed, similar to this study, 3D FEM analysis on the transient response of OWTs. It was reported that, although there was a difference locally on the build up of pore pressures, the global response displayed a very similar trend, where due to dilatancy induced suction, in the less permeable sands the turbine displayed less displacements overall.

The reported trend can be seen also in this analysis for *Cases A*, *B* where due to the strong loading regime, pore pressures reach the aforementioned plateau regardless of the sand permeability. As such, pile-head displacements for *Cases A*, *B*, see (Figure 25a) for *Case A*, do not vary drastically where as expected, for the most impermeable case, the displacements are the lowest ones recorded.

That is not exactly the case though for *Case C*. During a low loading regime, the level of shear loading exerted to the soils does not suffice to produce dilatant volumetric effects and thus sands operated constantly under a contractile regime. In the case of high permeability, excess pore pressures dissipate and sand densifies which can be clearly seen in (Figure 26) at the mudline in the soil adjacent to the monopile but also at (Figure 27) which displays the void ratio evolution at the control points $A_{L,R}$. What this means is that the agitated pore pressure field of the case with the lowest permeability causes a drop of effective confinement in the soil in the vicinity of the foundation and thus causing a less stiff response. That is translated into enhanced displacements and rotations of the foundation and is highly depicted on the calculated soil damping (Table 6).

Table 7: Summary of damping estimations for monopile supported offshore wind turbines from literature, modified table obtained from (Carswell et al., 2014). For this study the results only for DR=60% and 80% are displayed.

	(Tarp-Johansen et al., 2009)	(Versteijlen et al., 2011)	(Damgaard et al., 2012)	(Damgaard et al., 2013)
Method	Exprerimental	Exprerimental	Exprerimental	Exprerimental
Analysis	3D FEM	Modified p-y	Hysteretic p-y	Hysteretic p-y
Turbine	3.5 MW (Scaled NREL 5 MW)	Siemens 3.6 MW	-	Vestas
Soil	Generalized sandy or clayey North Sea	Medium dense sand and clay	Top layer loose sand,very stiff to very hard clay	Medium dense sand and soft clay
Monopile (L/D)	4.26	4.68	5.38	-
Wind velocity	-	11-19.7 m/s	3-13 m/s	-
$\zeta_{foundation}$	0.56%-0.80%	1.5%	0.58%	0.8%-1.3%
ζ_{struct}	0.19%	1.5%	0.19%	-
ζ_{total}	0.75%-0.99%	3%	0.77%	0.8%-1.3%

	(Shirzadeh et al., 2013)	(Carswell et al., 2014)	This study	
Method	Exprerimental	Numerical	Numerical	
Analysis	HAWC2, Rayleigh	2D and 3D FEM	3D FEM	
Turbine	Vestas	NREL 5 MW	Siemens 8 MW	
Soil	Dense sand with layer of stiff clay	Soft, stiff and hard clay	Medium dense and dense sand	
Monopile (L/D)	4.12	5.67	3.38	
Wind velocity	4.5-6.5 m/s	-	Low	24-47 m/s
$\zeta_{foundation}$	0.25%	0.17%-0.28%	0.56%-2.1%	2%-5.7%
ζ_{struct}	0.6%	1.00%	0.19%	
ζ_{total}	0.85%	1.17%-1.28%	0.76%-2.3%	2.2%-5.9%

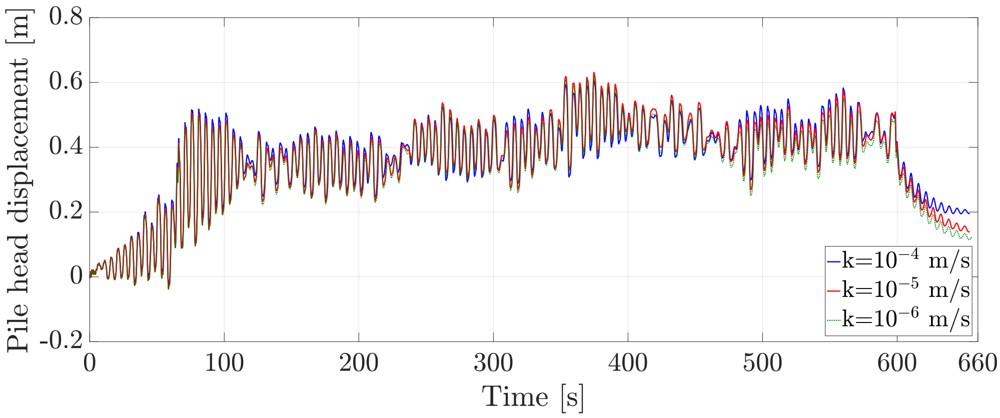

(a) *Case A*

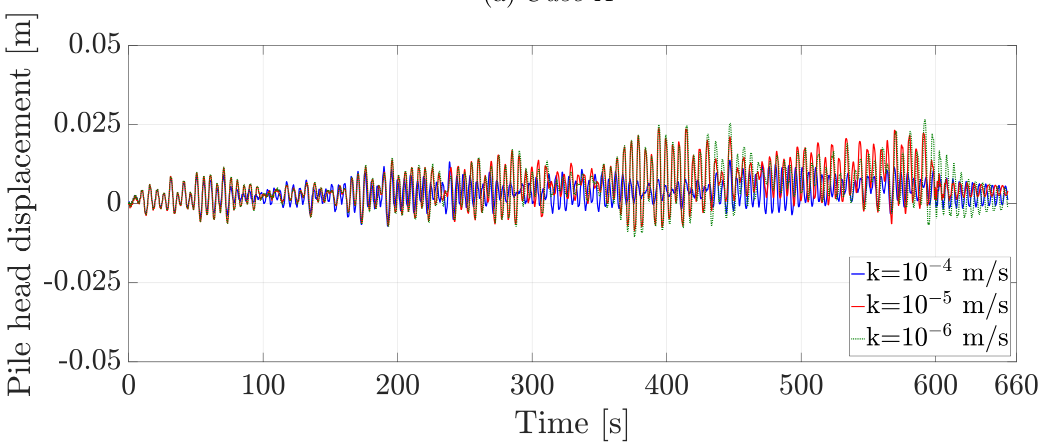

(b) *Case C*

Figure 25: Effect of permeability: Displacement at mudline for *Cases A*, *C*.

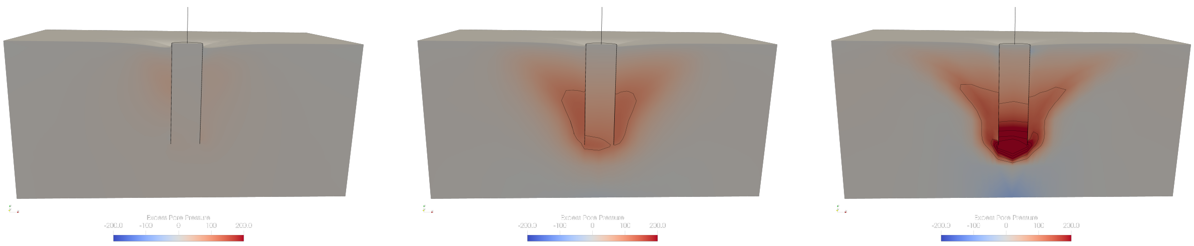

$600s: \ k = 10^{-4}$ $k = 10^{-5}$ $k = 10^{-6}$

Figure 26: Excess pore pressure depiction at 600s of analysis for all examined permeabilities: *Case C*, five contour lines are plotted, Δu = [100kPa-350kPa] split in equal increments.

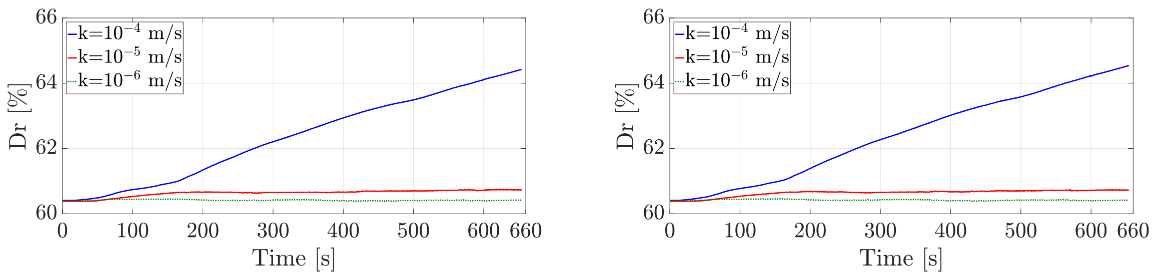

(a) A_L (b) A_R

Figure 27: Void ratio effects for *Case C*, DR=60% for all examined permeabilities.

4 Concluding Remarks

In this study an advanced 3D FEM analysis was undertaken to explore the response of an 8-MW offshore wind turbine during extreme storm events. The state of the art constitutive model of Manzari and Dafalias was exploited which endorses the critical state theory of soils and allows for cyclic loading simulation. Three types of soil configurations were examined with 40%-80% relative densities highlighting the effects of sand density and foundation size underestimation on the total system response. This study was able to address issues and reach to conclusions not yet seen in literature, namely:

- Response of an OWT during a rogue wave impact;
- Connected foundation size underestimation to OWT compliance with the applied loads;
- Both structural compliance to exerted loads and frequency drops recorded during storms have been linked with transient pore pressure evolution;
- Estimation of soil's contribution to damping during major storm events;
- Insight on damping evolution with increase of wind velocity;
- Effect of permeability on response during low loading amplitude. As damping seems to be severely affected by permeability when low amount of loading is applied, fatigue damage estimations might need to involve permeability as an affecting variable;

Most of these results could not have been obtained without a 600s analysis which is the longest analysis time seen in 3D FEM OWT simulations so far. The results obtained are in agreement with what has been published so far, giving further confidence to the validity of this work.

References

Achmus, M., Kuo, Y.-S., and Abdel-Rahman, K. (2009). Behavior of monopile foundations under cyclic lateral load. *Computers and Geotechnics*, 36(5):725–735.

Andrianopoulos, K. I., Papadimitriou, A. G., and Bouckovalas, G. D. (2010). Bounding surface plasticity model for the seismic liquefaction analysis of geostructures. *Soil Dynamics and Earthquake Engineering*, 30(10):895–911.

API, R. (2000). 2a-wsd. *Recommended practice for planning, designing and constructing fixed offshore platforms-working stress design*, 21.

API, R. (2011). 2geo (2011). *Recommended Practice for Geotechnical Foundation Design Consideration.*

Arany, L., Bhattacharya, S., Adhikari, S., Hogan, S., and Macdonald, J. (2015). An analytical model to predict the natural frequency of offshore wind turbines on three-spring flexible foundations using two different beam models. *Soil Dynamics and Earthquake Engineering*, 74:40–45.

Arany, L., Bhattacharya, S., Macdonald, J., and Hogan, S. (2017). Design of monopiles for offshore wind turbines in 10 steps. *Soil Dynamics and Earthquake Engineering*, 92:126–152.

Arany, L., Bhattacharya, S., Macdonald, J. H., and Hogan, S. J. (2016). Closed form solution of eigen frequency of monopile supported offshore wind turbines in deeper waters incorporating stiffness of substructure and ssi. *Soil Dynamics and Earthquake Engineering*, 83:18–32.

Babuška, I. (1973). The finite element method with Lagrangian multipliers. *Numerische Mathematik*, 20(3):179–192.

Bagiorgas, H. S., Mihalakakou, G., Rehman, S., and Al-Hadhrami, L. M. (2012). Offshore wind speed and wind power characteristics for ten locations in aegean and ionian seas. *Journal of earth system science*, 121(4):975–987.

Balog, I., Ruti, P. M., Tobin, I., Armenio, V., and Vautard, R. (2016). A numerical approach for planning offshore wind farms from regional to local scales over the mediterranean. *Renewable Energy*, 85:395–405.

Barari, A., Bagheri, M., Rouainia, M., and Ibsen, L. B. (2017). Deformation mechanisms for offshore monopile foundations accounting for cyclic mobility effects. *Soil Dynamics and Earthquake Engineering*, 97:439–453.

Barber, E. (1953). Discussion to paper by sm gleser. *ASTM, STP*, 154:96–99.

Been, K. and Jefferies, M. (1985). A state parameter for sands. *Géotechnique*, 35(2):99–112.

Borja, R. and Amies, A. (1994). Multiaxial cyclic plasticity model for clays. *Journal of Geotechnical Engineering*, 120(6):1051–1070.

Brezzi, F. (1974). On the existence, uniqueness and approximation of saddle-point problems arising from Lagrangian multipliers. *Revue française d'automatique, informatique, recherche opérationnelle. Analyse numérique*, 8(2):129–151.

Byrne, B., McAdam, R., Burd, H., Houlsby, G., Martin, C., Beuckelaers, W., Zdravkovic, L., Tabora, D., Potts, D., Jardine, R., Ushev, E., Liu, T., Abadias, D., Gavin, K., Igoe, D., Doherty, P., Skov Gretlund, J., Pacheco Andeade, M., Muir Wood, A., Schroeder, F., Turner, S., and Plummer, M. (2017). Pisa: New design methods for offshore wind tutbine monopiles. In *Offshore Site Investigation and Geotechnics: Smarter Solutions for Future Offshore Developments*. Society of Underwater Technology.

Carlson, N. N. and Miller, K. (1998). Design and application of a gradient-weighted moving finite element code. *SIAM Journal on Scientific Computing*, 19(3):728–798.

Carswell, W., Johansson, J., Løvholt, F., Arwade, S. R., and DeGroot, D. J. (2014). Dynamic mudline damping for offshore wind turbine monopiles. In *Proceedings of the ASME 2014 33rd international conference on ocean, offshore and arctic engineering OMAE2014 June*, volume 8, page 13.

Carter, M., Bentley, S. P., et al. (1991). *Correlations of soil properties.* Pentech press publishers.

Chopra, A. K. (1995). *Dynamics of Structures*, volume 3. Prentice Hall New Jersey.

Christoforaki, M. and Tsoutsos, T. (2017). Sustainable siting of an offshore wind park a case in chania, crete. *Renewable Energy*, 109:624–633.

Corciulo, S., Zanoli, O., and Pisanò, F. (2017). Transient response of offshore wind turbines on monopiles in sand: role of cyclic hydro–mechanical soil behaviour. *Computers and Geotechnics*, 83:221–238.

Corti, R., Diambra, A., Wood, D. M., Escribano, D. E., and Nash, D. F. (2016). Memory surface hardening model for granular soils under repeated loading conditions. *Journal of Engineering Mechanics*, 142(12):04016102.

Cuéllar, P., Mira, P., Pastor, M., Fernández-Merodo, J. A., Baeßler, M., and Rücker, W. (2014). A numerical model for the transient analysis of offshore foundations under cyclic loading. *Computers and Geotechnics*, 59:75–86.

Dafalias, Y. F. and Manzari, M. T. (2004). Simple plasticity sand model accounting for fabric change effects. *Journal of Engineering mechanics*, 130(6):622–634.

Dafalias, Y. F., Manzari, M. T., and Papadimitriou, A. G. (2006). SANICLAY: simple anisotropic clay plasticity model. *International Journal for Numerical and Analytical Methods in Geomechanics*, 30(12):1231–1257.

Damgaard, M., Andersen, J., Ibsen, L., and Andersen, L. (2013). Time-varying dynamic properties of offshore wind turbines evaluated by modal testing. In *Proceedings of the 18th international conference on soil mechanics and geotechnical engineering*, page 234.

Damgaard, M., Andersen, J. K., et al. (2012). Natural frequency and damping estimation of an offshore wind turbine structure. In *The Twenty-second International Offshore and Polar Engineering Conference*. International Society of Offshore and Polar Engineers.

De Borst, R., Crisfield, M. A., Remmers, J. J., and Verhoosel, C. V. (2012). *Nonlinear finite element analysis of solids and structures*. John Wiley & Sons.

Depina, I., Le, T. M. H., Eiksund, G., and Benz, T. (2015). Behavior of cyclically loaded monopile foundations for offshore wind turbines in heterogeneous sands. *Computers and Geotechnics*, 65:266–277.

Devriendt, C., Jordaens, P. J., De Sitter, G., and Guillaume, P. (2013). Damping estimation of an offshore wind turbine on a monopile foundation. *IET Renewable Power Generation*, 7(4):401–412.

di Prisco, C. G. and Wood, D. M. (2012). *Mechanical Behaviour of Soils Under Environmentally-Induced Cyclic Loads*. Springer.

DNV, D. N. V. (2014). Dnv-os-j101 offshore standard: Design of offshore wind turbine structures. *DNV AS, Høvik, Norway*.

Doherty, P. and Gavin, K. (2012). Laterally loaded monopile design for offshore wind farms. *Proceedings of the Institution of Civil Engineers - Energy*, 165(1):7–17.

Dysli, M. and Steiner, W. (2011). *Correlations in soil mechanics*. PPUR Presses polytechniques.

Elgamal, A., Yang, Z., Parra, E., and Ragheb, A. (2003). Modeling of cyclic mobility in saturated cohesionless soils. *International Journal of Plasticity*, 19(6):883–905.

En, B. (1991). 1-4: 2005 eurocode 1: Actions on structuresgeneral actionswind actions.

Gajo, A. and Wood, D. M. (1999). A kinematic hardening consitutive model for sands: the multiaxial formulation. *International Journal for Numerical and Analytical methods in Geomechanics*, 23:925 – 965.

Gazetas, G. (1984). Seismic response of end-bearing single piles. *International Journal of Soil Dynamics and Earthquake Engineering*, 3(2):82–93.

Goodman, R. E., Taylor, R. L., and Brekke, T. L. (1968). A model for the mechanics of jointed rock. *Journal of Soil Mechanics & Foundations Division*, 94(3):637–659.

Griffiths, D. V. (1985). Numerical modeling of interfaces using conventional finite elements. In *Proceedings of 5th International Conference on Numerical Methods in Geomechanics. Nagoya, Japan*, pages 837–844.

He, Y., Byrne, B., and Burd, H. (2017). Application of a numerical-based design method for laterally loaded monopiles in layered soils. In *Offshore Site Investigation and Geotechnics: Smarter Solutions for Future Offshore Developments*. Society of Underwater Technology.

Helnwein, P. (2001). Some remarks on the compressed matrix representation of symmetric second-order and fourth-order tensors. *Computer methods in applied mechanics and engineering*, 190(22):2753–2770.

Houlsby, G. T. and Mortara, G. (2004). A continuous hyperplasticity model for sands under cyclic loading. In *Proceedings of the International Conference on Cyclic Behaviour of Soils and Liquefaction Phenomena. Bochum, Germany*, volume 31, pages 21–26.

Huang, M., Yue, Z. Q., Tham, L. G., and Zienkiewicz, O. C. (2004). On the stable finite element procedures for dynamic problems of saturated porous media. *International Journal for Numerical Methods in Engineering*, 61(9):1421–1450.

Hughes, T. J. R. (1987). *The Finite Element Method: linear static and dynamic finite element analysis*. Prentice-Hall.

Ishihara, K., Tatsuoka, F., and Yasuda, S. (1975). Undrained deformation and liquefaction of sand under cyclic stresses. *Soils and Foundations - Japanese Society of Soil Mechanics and Foundation Engineering*, 15(1):29–44.

Jeanjean, P. et al. (2009). Re-assessment of py curves for soft clays from centrifuge testing and finite element modeling. In *Offshore Technology Conference*. Offshore Technology Conference.

Jeremić, B., Cheng, Z., Taiebat, M., and Dafalias, Y. F. (2008). Numerical simulation of fully saturated porous materials. *International Journal for Numerical and Analytical Methods in Geomechanics*, 32(13):1635–1660.

Jeremić, B., Jie, G., Preisig, M., and Tafazzoli, N. (2009). Time domain simulation of soil–foundation–structure interaction in non–uniform soils. *Earthquake Engineering and Structural Dynamics*, 38(5):699–718.

Kallehave, D., Byrne, B. W., Thilsted, C. L., and Mikkelsen, K. K. (2015a). Optimization of monopiles for offshore wind turbines. *Philosophical Transactions of the Royal Society of London A: Mathematical, Physical and Engineering Sciences*, 373(2035):1–15.

Kallehave, D., Thilsted, C., and Diaz, A. T. (2015b). Observed variations of monopile foundation stiffness. In *The 3rd Internationl symposium on Frontiers in offshore Geotechnics*, pages 717–722. CRC Press LLC.

Kallehave, D., Thilsted, C. L., and Liingaard, M. (2012a). Modification of the API p-y formulation of initial stiffness of sand. In *Proceedings of Offshore Site Investigation and Geotechnics: Integrated Technologies - Present and Future. London, UK*, pages 465–472. Society of Underwater Technology.

Kallehave, D., Thilsted, C. L., Liingaard, M., et al. (2012b). Modification of the api py formulation of initial stiffness of sand. In *Offshore Site Investigation and Geotechnics: Integrated Technologies-Present and Future*. Society of Underwater Technology.

Kramer, S., Sideras, S., and Greenfield, M. (2016). The timing of liquefaction and its utility in liquefaction hazard evaluation. *Soil Dynamics and Earthquake Engineering*, 91:133–146.

Lavagnini, A., Sempreviva, A. M., and Barthelmie, R. J. (2003). Estimating wind energy potential offshore in mediterranean areas. *Wind Energy*, 6(1):23–34.

Leblanc, C. and Tarp-Johansen, N. J. (2010). Monopiles in sand. stiffness and damping.

Leonards, G. A. (1962). Foundation engineering.

Li, X. and Dafalias, Y. F. (2000). Dilatancy for cohesionless soils. *Geotechnique*, 50(4):449–460.

López-Querol, S., Fernández-Merodo, J. A., Mira, P., and Pastor, M. (2008). Numerical modelling of dynamic consolidation on granular soils. *International journal for numerical and analytical methods in geomechanics*, 32(12):1431–1457.

Manzari, M. T. and Dafalias, Y. F. (1997). A critical state two-surface plasticity model for sands. *Geotechnique*, 47(2):255–272.

Matlock, H. (1970). Correlations for design of laterally loaded piles in soft clay. *Offshore Technology in Civil Engineerings Hall of Fame Papers from the Early Years*, pages 77–94.

McGann, C. R., Arduino, P., and Mackenzie-Helnwein, P. (2012). Stabilized single-point 4-node quadrilateral element for dynamic analysis of fluid saturated porous media. *Acta Geotechnica*, 7(4):297–311.

McGann, C. R., Arduino, P., and Mackenzie-Helnwein, P. (2015). A stabilized single-point finite element formulation for three-dimensional dynamic analysis of saturated soils. *Computers and Geotechnics*, 66:126–141.

Mróz, Z., Norris, V. A., and Zienkiewicz, O. C. (1978). An anisotropic hardening model for soils and its application to cyclic loading. *International Journal for Numerical and Analytical Methods in Geomechanics*, 2:203–221.

Nasser, S. (1980). On behavior of granular materials in simple shear. *SOILS AND FOUNDATIONS*, 20(3):59–73.

Nemat-Nasser, S. and Tobita, Y. (1982). Influence of fabric on liquefaction and densification potential of cohesionless sand. *Mechanics of Materials*, 1(1):43 – 62.

Newman, J. N. (1977). *Marine hydrodynamics*. MIT press.

Newmark, N. M. (1959). A method of computation for structural dynamics. *ASCE Journal of Engineering Mechanics Division*, 85(3):67–94.

Papadimitriou, A. G. and Bouckovalas, G. D. (2002). Plasticity model for sand under small and large cyclic strains: a multiaxial formulation. *Soil Dynamics and Earthquake Engineering*, 22(3):191–204.

Pastor, M., Zienkiewicz, O. C., and Leung, K. H. (1985). Simple model for transient soil loading in earthquake analysis. II: Non-associative models for sands. *International journal for numerical and analytical methods in geomechanics*, 9(5):477–498.

Pastor, M., Zienkiewicz, O. C., Li, T., Xiaoqing, L., and Huang, M. (1999). Stabilized finite elements with equal order of interpolation for soil dynamics problems. *Archives of Computational Methods in Engineering*, 6(1):3–33.

Pender, M. (1993). Aseismic pile foundation design analysis. *Bulletin of the New Zealand National Society for Earthquake Engineering*, 26(1):49–160.

Pisanò, F. and Jeremić, B. (2014). Simulating stiffness degradation and damping in soils via a simple visco-elastic–plastic model. *Soil Dynamics and Earthquake Engineering*, 63:98–109.

Poulos, H. G. and Davis, E. H. (1980). *Pile foundation analysis and design*. Number Monograph.

Preisig, M. and Prévost, J. H. (2011). Stabilization procedures in coupled poromechanics problems: A critical assessment. *International Journal for Numerical and Analytical Methods in Geomechanics*, 35(11):1207–1225.

Prévost, J. H. (1985). A simple plasticity theory for frictional cohesionless soils. *International Journal of Soil Dynamics and Earthquake Engineering*, 4(1):9–17.

Prévost, J. H. and Popescu, R. (1996). Constitutive relations for soil materials. *Electronic Journal of Geotechnical Engineering*.

Puzrin, A. M. and Houlsby, G. T. (2001). Fundamentals of kinematic hardening hyperplasticity. *International journal of solids and structures*, 38(21):3771–3794.

Randolph, M. F. (1981). The response of flexible piles to lateral loading. *Geotechnique*, 31(2):247–259.

Schweizer, J., Antonini, A., Govoni, L., Gottardi, G., Archetti, R., Supino, E., Berretta, C., Casadei, C., and Ozzi, C. (2016). Investigating the potential and feasibility of an offshore wind farm in the northern adriatic sea. *Applied Energy*, 177:449–463.

Scott, M. H. and Fenves, G. L. (2003). A Krylov subspace accelerated Newton algorithm. In *Proceedings of 2003 ASCE Structures Congress. Seattle, Washington, USA*.

Seidalinov, G. and Taiebat, M. (2014). Bounding surface SANICLAY plasticity model for cyclic clay behavior. *International Journal for Numerical and Analytical Methods in Geomechanics*, 38(7):702–724.

Senanayake, A., Gilbert, R. B., Manuel, L., et al. (2017). Estimating natural frequencies of monopile supported offshore wind turbines using alternative py models. In *Offshore Technology Conference*. Offshore Technology Conference.

Shadlou, M. and Bhattacharya, S. (2016). Dynamic stiffness of monopiles supporting offshore wind turbine generators. *Soil Dynamics and Earthquake Engineering*, 88:15–32.

Shirzadeh, R., Devriendt, C., Bidakhvidi, M. A., and Guillaume, P. (2013). Experimental and computational damping estimation of an offshore wind turbine on a monopile foundation. *Journal of Wind Engineering and Industrial Aerodynamics*, 120:96–106.

Sloan, S. W. (1987). Substepping schemes for the numerical integration of elastoplastic stress–strain relations. *International Journal for Numerical Methods in Engineering*, 24(5):893–911.

Stockwell, R. G., Mansinha, L., and Lowe, R. (1996). Localization of the complex spectrum: the s transform. *IEEE transactions on signal processing*, 44(4):998–1001.

Swiss Standard, S. (1999). 670 010b. *Characteristic Coefficients of soils, Association of Swiss Road and Traffic Engineers*.

Taborda, D. M. G., Zdravković, L., Kontoe, S., and Potts, D. M. (2014). Computational study on the modification of a bounding surface plasticity model for sands. *Computers and Geotechnics*, 59:145–160.

Taiebat, M. and Dafalias, Y. F. (2008). SANISAND: Simple anisotropic sand plasticity model. *International Journal for Numerical and Analytical Methods in Geomechanics*, 32(8):915–948.

Tarp-Johansen, N. J., Andersen, L., Christensen, E. D., Mørch, C., Frandsen, S., and Kallesøe, B. (2009). Comparing sources of damping of cross-wind motion. In *The European Offshore Wind Conference & Exhibition*. The European Wind Energy Association.

Tasiopoulou, P. and Gerolymos, N. (2016). Constitutive modeling of sand: Formulation of a new plasticity approach. *Soil Dynamics and Earthquake Engineering*, 82:205–221.

Tatsuoka, F. and Ishihara, K. (1974). Drained deformation of sand under cyclic stresses reversing direction. *Soils and Foundations - Japanese Society of Soil Mechanics and Foundation Engineering*, 14(3):51–65.

Valamanesh, V. and Myers, A. (2014). Aerodynamic damping and seismic response of horizontal axis wind turbine towers. *Journal of Structural Engineering*, 140(11):04014090.

Versteijlen, W., De Vries, W., Metrikine, A., Hoving, J., and Smidt, E. (2011). Estimation of the vibration decrement of an offshore wind turbine support structure caused by its interaction with soil. In *Proceedings of the EWEA Offshore 2011 Conference, Amsterdam, The Netherlands, 29 November-1 December 2011*. European Wind Energy Association.

Versteijlen, W., Renting, F., van der Valk, P., Bongers, J., van Dalen, K., and Metrikine, A. (2017). Effective soil-stiffness validation: Shaker excitation of an in-situ monopile foundation. *Soil Dynamics and Earthquake Engineering*, 102:241 – 262.

Wang, Z.-L., Dafalias, Y. F., and Shen, C.-K. (1990). Bounding surface hypoplasticity model for sand. *Journal of engineering mechanics*, 116(5):983–1001.

Watanabe, K., Pisanò, F., and Jeremić, B. (2016). Discretization effects in the finite element simulation of seismic waves in elastic and elastic-plastic media. *Engineering with Computers*, pages 1–27.

WindEnergie, G. (2005a). Overall damping for piled offshore support structures, guideline for the certification of offshore wind turbines. *Germanischer Lloyd WindEnergie*.

WindEnergie, G. L. (2005b). Guideline for the certification of offshore wind turbines. *Germanischer Lloyd Rules and Guidelines, IVIndustrial Services, Part*.

Wood, D. M., Belkheir, K., and Liu, D. F. (1994). Strain softening and state parameter for sand modelling. *Géotechnique*, 44(2):335–339.

Yang, Z. and Elgamal, A. (2008). Multi-surface cyclic plasticity sand model with Lode angle effect. *Geotechnical and Geological Engineering*, 26(3):335–348.

Zahmatkesh, A. and Janalizadeh Choobbasti, A. (2017). Calibration of an advanced constitutive model for babolsar sand accompanied by liquefaction analysis. *Journal of Earthquake Engineering*, 21(4):679–699.

Zdravković, L., Taborda, D., Potts, D., Jardine, R., Sideri, M., Schroeder, F., Byrne, B., McAdam, R., Burd, H., Houlsby, G., et al. (2015). Numerical modelling of large diameter piles under lateral loading for offshore wind applications. In *Proceeding 3rd International Symposium on Frontiers in Offshore Geotechnics. Norway:[sn]*.

Zhang, Y., Pedroso, D. M., and Li, L. (2016). FDM and FEM solutions to linear dynamics of porous media: stabilised, monolithic and fractional schemes. *International Journal for Numerical Methods in Engineering.*

Zienkiewicz, O. C., Best, B., Dullage, C., and Stagg, K. G. (1970). Analysis of non-linear problems in Rock Mechanics with particular reference to jointed rock systems. In *Proceedings of 2nd Congress of the International Society for Rock Mechanics. Belgrad, Yugoslavia*, pages 501–509.

Zienkiewicz, O. C., Chan, A. H. C., Pastor, M., Schrefler, B. A., and Shiomi, T. (1999). *Computational geomechanics*. Wiley Chichester.

Zienkiewicz, O. C., Chang, C. T., and Bettess, P. (1980). Drained, undrained, consolidating and dynamic behaviour assumptions in soils. *Géotechnique*, 30(4):385–395.

Zienkiewicz, O. C., Leung, K. H., and Pastor, M. (1985). Simple model for transient soil loading in earthquake analysis. I. Basic model and its application. *International Journal for Numerical and Analytical Methods in Geomechanics*, 9(5):453–476.

Zienkiewicz, O. C. and Shiomi, T. (1984). Dynamic behaviour of saturated porous media; the generalized Biot formulation and its numerical solution. *International Journal for Numerical and Analytical Methods in Geomechanics*, 8(1):71–96.

Zienkiewicz, O. C. and Taylor, R. L. (2000). *The Finite Element Method. Volume 1: The Basis.* Butterworth-Heinemann, fifth edition.

Zountouridou, E., Kiokes, G., Chakalis, S., Georgilakis, P., and Hatziargyriou, N. (2015). Offshore floating wind parks in the deep waters of mediterranean sea. *Renewable and Sustainable Energy Reviews*, 51:433–448.

A Appendix

A.1 Manzari and Dafalias

In (Figure 28) the performance of SaniSand2004 under cyclic triaxial conditions can be seen.

A.2 Mesh sensitivity

This study, from its origin was intended to examine long time-histories. Accordingly time was invested into the implementation of an algorithm which, with limited effort could produce scripts with different mesh characteristics. The most appropriate size and mesh discretization was selected based on mesh and time sensitivity tests. In total the comparison between four different meshes will be displayed here. Useful information about the mesh size and densities is provided in (Table 8). The different meshes examined can be seen in (Figure30).

As the loading histories provided are expected to induce a highly non-linear response from the soil, the mesh sensitivity time-history should provide an equal amount of non-linearity. In that context the hub was loaded up to $9MN$ within 2.5 seconds (Figures 29 and 31a) and then the load was removed so that the turbine would oscillate with its natural frequency. Allowing the system to oscillate freely, gives further insight on the applicability of the mesh and timestep size to meet accuracy criteria regarding capturing wave propagation related to element size relative to the timestep size analysed.

The results of the mesh sensitivity analysis were examined based on the global response time-history (hub and pile head displacement) but also locally through the response of 2 control points seen in 29. Results indicate that although local response might slightly vary between meshes A-D

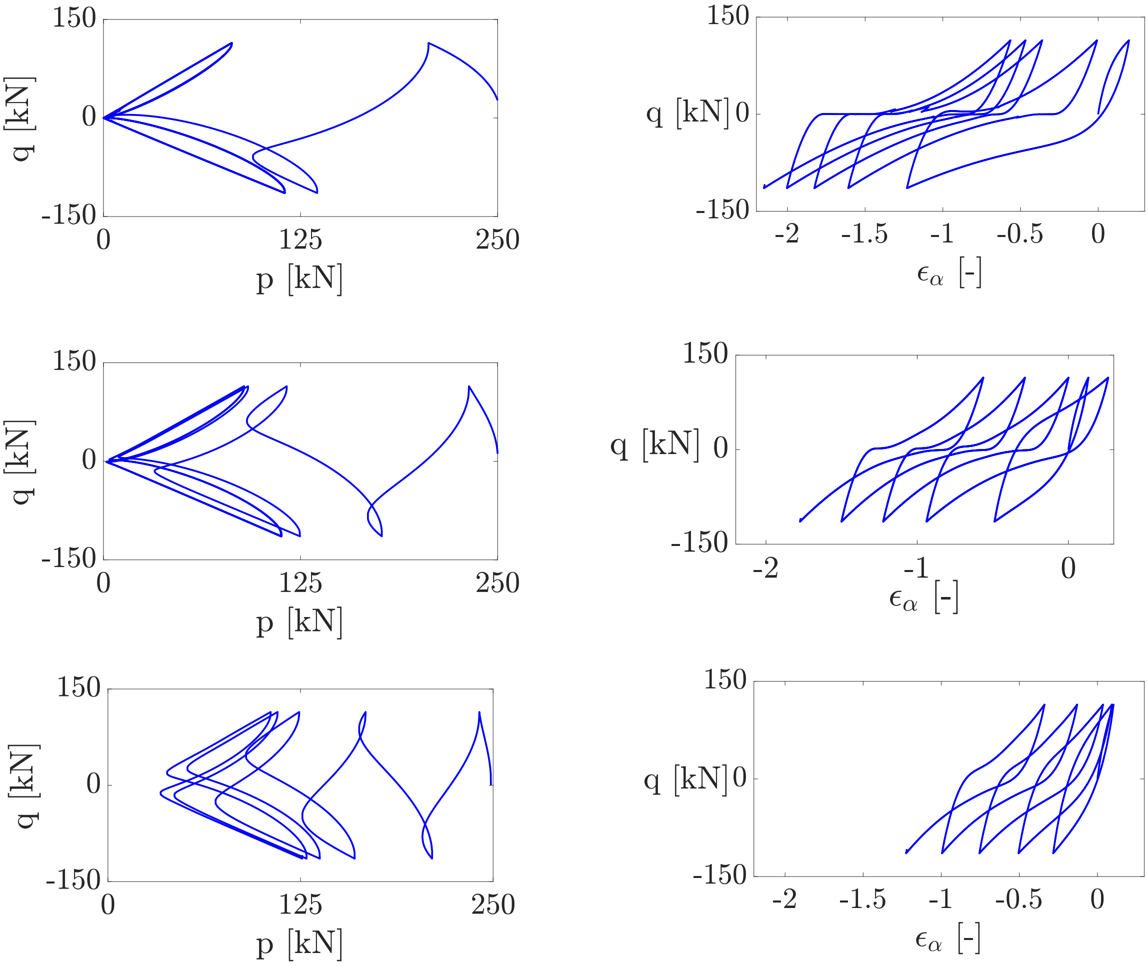

Figure 28: Cyclic response of sand on a 2-way stress controlled cyclic triaxial test according to SaniSand2004 model: Toyoura sand with 40% (top), 60% (middle) and 80% (bottom) relative density. Left side plots display deviatoric versus mean effective stress, right side plots display deviatoric stress versus axial strain.

Table 8: Size of the soil domain and the computing time for a 20 sec highly non-linear sensitivity analysis. Analysis where calculated on a i7-4790 4.00GHz CPU.

	Mesh A	Mesh B	Mesh C	Mesh D
Elements (SSpbrickUP)	2000	2600	4000	5800
Nodes (4 dof)	2400	3100	4700	5000
Mesh size [m] (W - L - H)	80 - 40 - 43	90 - 46 - 43	127 - 64 - 43	90 - 46 - 43
Analysis time [hrs]	$\approx 4\,\frac{1}{2}$	$\approx 7\,\frac{1}{2}$	≈ 17	≈ 28

(Figure 33), global response remains unaffected (Figure 31). Depictions of the meshes examined (excess pore pressure) at 10′ of analysis can be seen in (Figure 32). The aforementioned results indicate that all four meshes examined could be considered as viable candidates for the final analysis. More precisely slight deterrences are observed in pore pressure development on the control points while globally the distribution of excess pore pressures though the mesh seem almost identical in all four meshes. Furthermore stress-strain plots in the plane most affected by loading (xz), indicate that all mesh options are applicable.

The computational burden avoided (Table 8) by choosing a coarser mesh is non-negligible. Mesh D requires more than 600% additional running time from mesh A, 400% more from mesh B and 60% more than mesh C. In that context, mesh B was chosen to avoid unforeseen effects from the prolonged analysis time (600′) examined in this study.

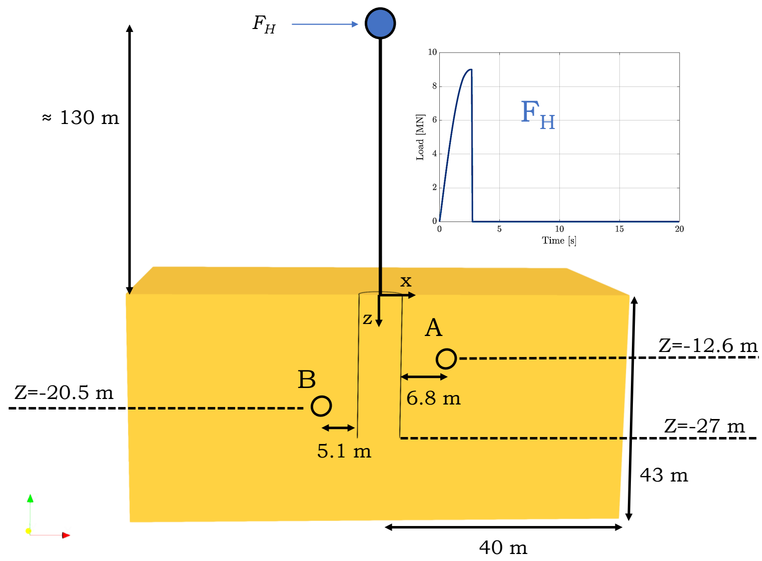

Figure 29: Depiction of the mesh with specification of the location for control points A and B. (Tower structure not to scale).

A.3 Time step sensitivity

A sensitivity analysis was undertaken to examine the effect of the chosen time step. By calibrating the time marching algorithm with adaptive timestepping, the user is able to specify a range of timesteps for time marching. That said, the user specifies a preferred time step size but if the solution algorithm determines that convergence is hardly or even very easily achieved, is able to alter the time step within the pre-specified range.

The sensitivity analysis was undertaken on a smaller mesh due to time limitations. A milder load time history (Figure 34) was chosen which still ensures a high degree of non-linearity inside the soil. Results indicate (Figure 35d) that the effect of the chosen timestep on the solution is negligible. Both global but also local (element) responses are non-distinguishable from each other for the timestep range examined. That can be attributed to the fact that, as described above, when converge is hard to achieve, OpenSees integral algorithm alters the timestep to ease the solution process.

That effect becomes obvious from the non-linear effect time step has on the analysis time (Table 8). As seen in each analysis the time step width is reduced by five times. Reducing the time step from dt=1×10^{-2} to dt=5×10^{-3}, [5×], results in an increase of analysis time of only [1.3×], while a further [5×] decrease of time step reduces analysis time by [4.2×]. That is attributed to the

Table 9: Timestep and stabilization parameter α sensitivity analysis: Timestep size and stabilization parameters explored along with required computing time for the load case considered. Analysis where calculated on a i7-4790 4.00GHz CPU.

Timestep	dt=1×10^{-2}	dt=5×10^{-3}	dt=1×10^{-3}	
Analysis time [mins]	39 mins	51 mins	215 mins	

Stabilization parameter α	$\alpha = 3 \times 10^{-5}$	$\alpha = 3 \times 10^{-6}$	$\alpha = 3 \times 10^{-7}$	$\alpha = 3 \times 10^{-8}$
Analysis time [mins]	36 mins	41 mins	47 mins	48 mins

increased number of iterations needed to achieve convergence when time step is bigger but also due to the continuous attempts of OpenSees to decrease timestep so that convergence is possible.

Since the chosen load time histories, but also the different soil densities to be considered in the final analysis of this study result in a variety of non linear responses, time step widths were analysis-specific. The sensitivity analysis gave the authors the luxury of confidence for using timestep widths within the examined range.

A.4 Stabilization parameter α sensitivity

The utilization of the H1-P1ssp brick elements proposed by McGann et al. (2015) and discussed in (Section 2.1.2), requires the specification of the stabilization parameter α. This parameter controls the extent of the enhanced strain field (amount of fictitious compressibility). The parameter can be calculated once the mesh size has been chosen by using an approximate element size as seen in (Equation 6). As size of elements varies though the mesh, locations where incompressibility might be critical were identified (large shear due to loading combined with large drainage paths). According to (Equation 6) a suitable choice for this analysis would be in the range of ($\alpha = 10^{-5}$ - $\alpha = 10^{-6}$). It is evident, from (Table 8) that an increase of the α parameter eases convergence as analysis time is shorter for higher α. An increase in the level of fictitious compressibility renders the solution less stiff thus reducing computational effort.

Results from the sensitivity analysis can be seen in (Figure 36). Results indicate minuscule effect on global system response while locally negligible influence is observed. Dynamic simulations were finally performed with an SSP stabilization parameter $\alpha = 8 \times 10^{-6}$.

A.5 Calculation of fundamental frequency according to simplified analytical models

The calculations following the work of (Arany et al., 2017) will be presented here. Foundation stiffness in this example is calculated following (Shadlou and Bhattacharya, 2016). It must be noted that as most details regarding the structural design are highly confidential, the worked example will shortly differ than the one examined in this study and thus the calculated frequency will differ as well.

It was described at (Section 3.3.1), the natural frequency of the tower including the substructure were obtained numerically. That would mean that all the calculations regarding estimating the fixed base natural frequency of the tower and accounting of the effect of the flexibility of the substructure (structure above the mudline and below the transition piece, (Figure 37)) were avoided. The final estimation of the natural frequency is given by (Equation 10).

$$f_0 = C_L C_R C_S f_{FB} \tag{10}$$

Where f_0 is the natural frequency of the system, C_L and C_R are the lateral and rotational foundation flexibility coefficients, which describe the foundation, C_S is the substructure flexibility

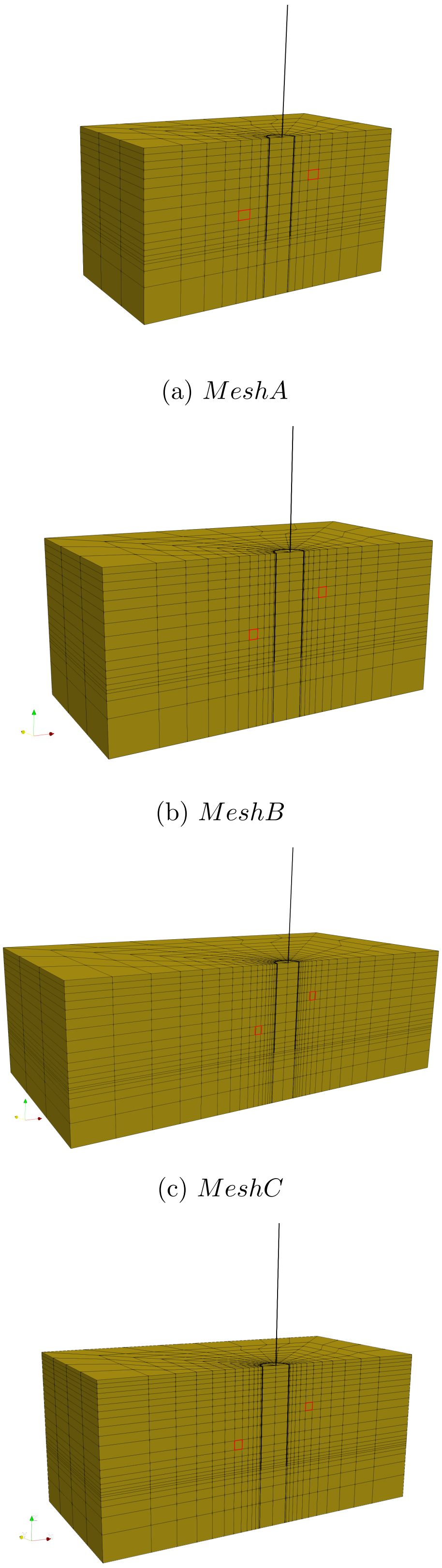

(a) $MeshA$

(b) $MeshB$

(c) $MeshC$

(d) $MeshD$

Figure 30: Mesh discretization sensitivity: Mesh A ($\approx$ 10000 $dofs\,for\,soil$), Mesh B ($\approx$ 12000 $dofs\,for\,soil$), Mesh C ($\approx$ 18000 $dofs\,for\,soil$), Mesh D ($\approx$ 20000 $dofs\,for\,soil$).

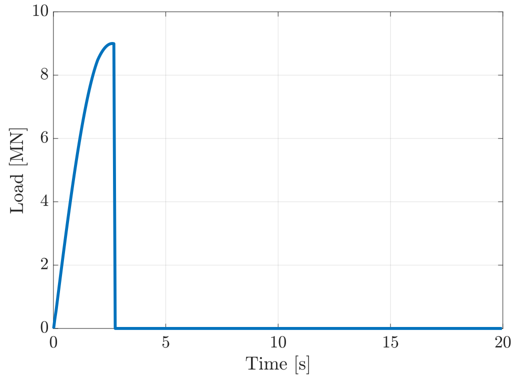

(a) $MeshB$

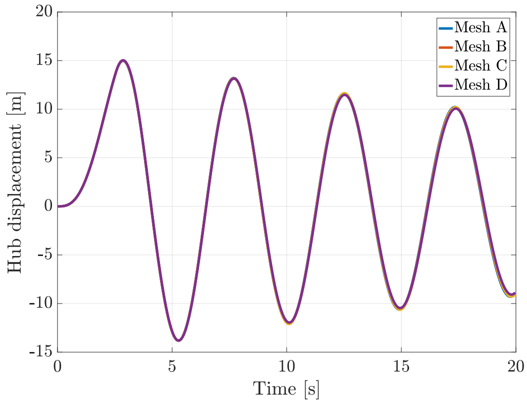

(b)

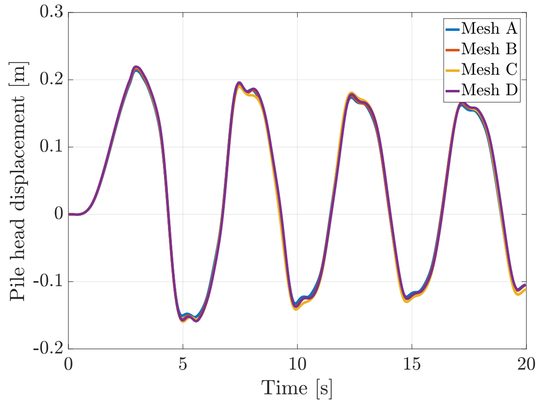

(c)

Figure 31: Domain size sensitivity analysis: (a) applied load (b) hub and (c) monopile head displacement at sensitivity analysis load case.

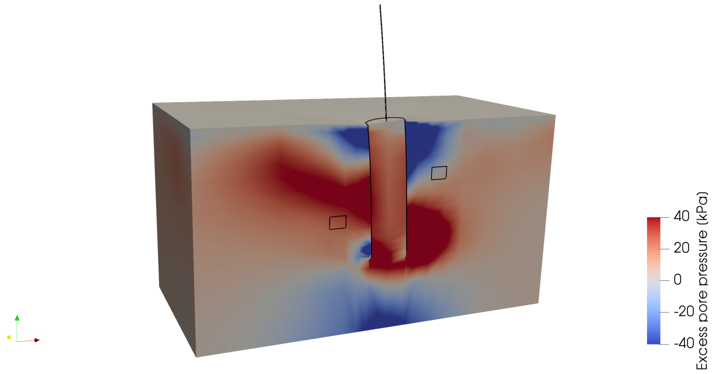

(a) $MeshA$

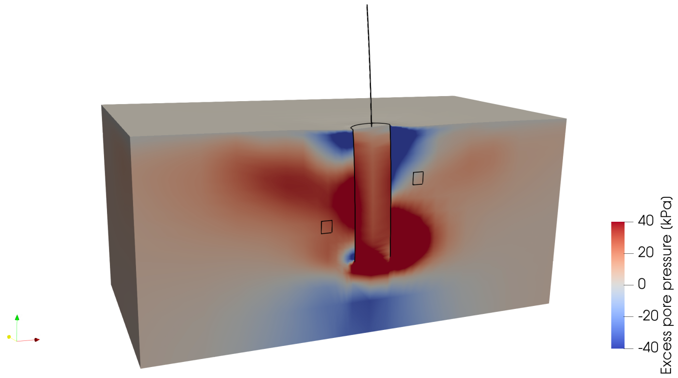

(b) $MeshB$

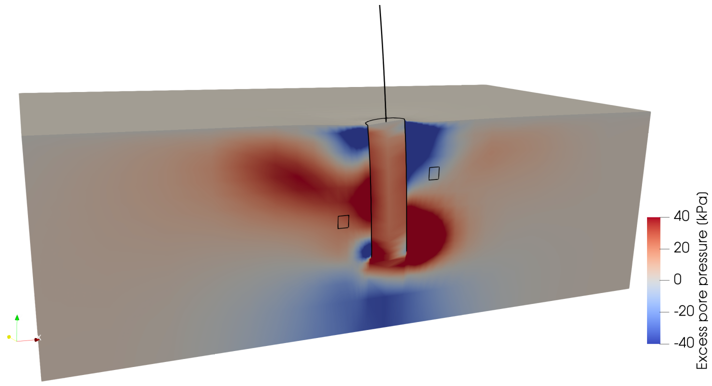

(c) $MeshC$

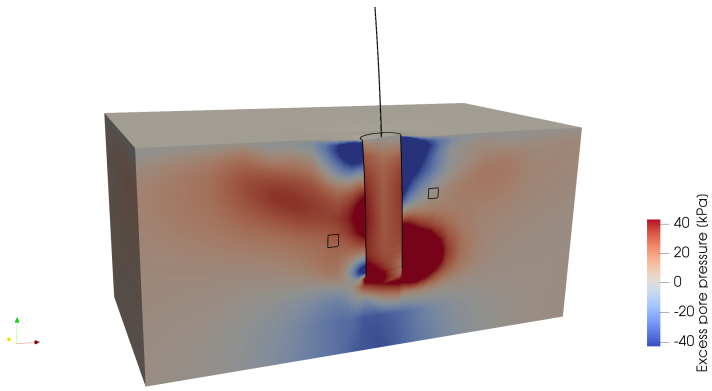

(d) $MeshD$

Figure 32: Mesh discretization sensitivity analysis: excess pore pressure Δu at leftward 2^{nd} cycle. Boxes denote control elements for which response is recorded.

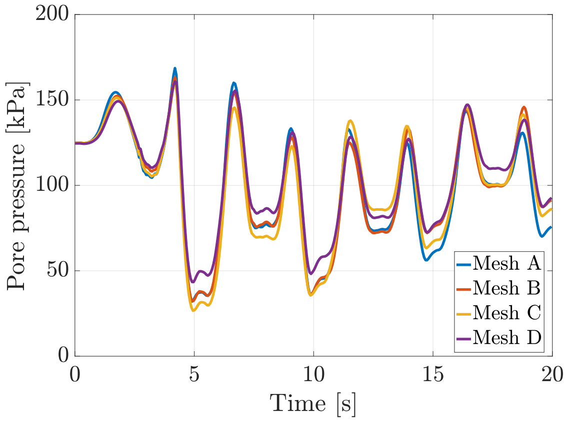

(a) Control point A

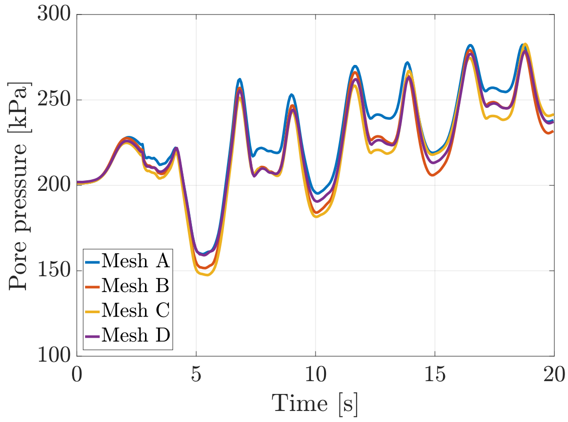

(b) Control point B

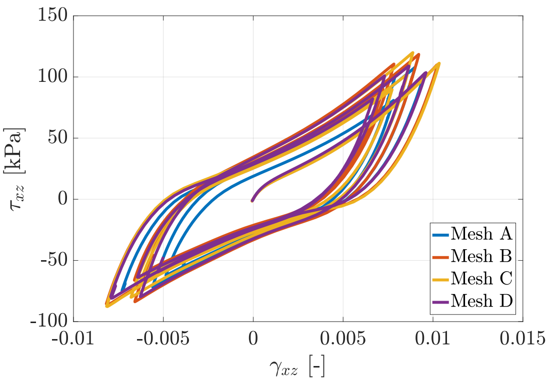

(c) Control point A

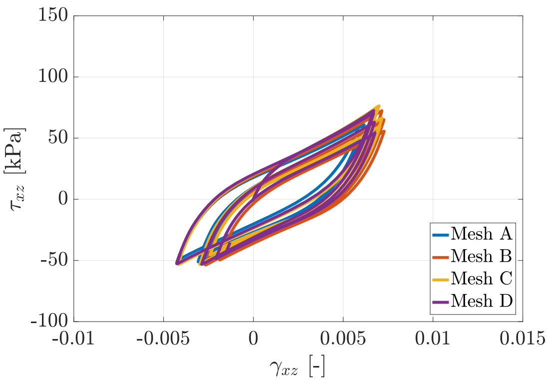

(d) Control point B

Figure 33: Mesh sensitivity analysis: (Top) pore pressure versus time (Bottom) stress strain response recorder at the control points. (Figure 29).

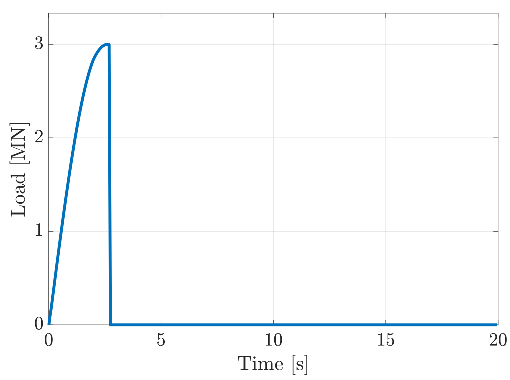

Figure 34: Load for timestep and stabilization parameter α sensitivity analysis.

coefficient and f_{FB} is the fixed base (cantilever) natural frequency of the tower. By calculating the effect of the substructure flexibility and the f_{FB} of the tower numerically we obtain:

$$f_{FB} \times C_S = 0.218Hz \tag{11}$$

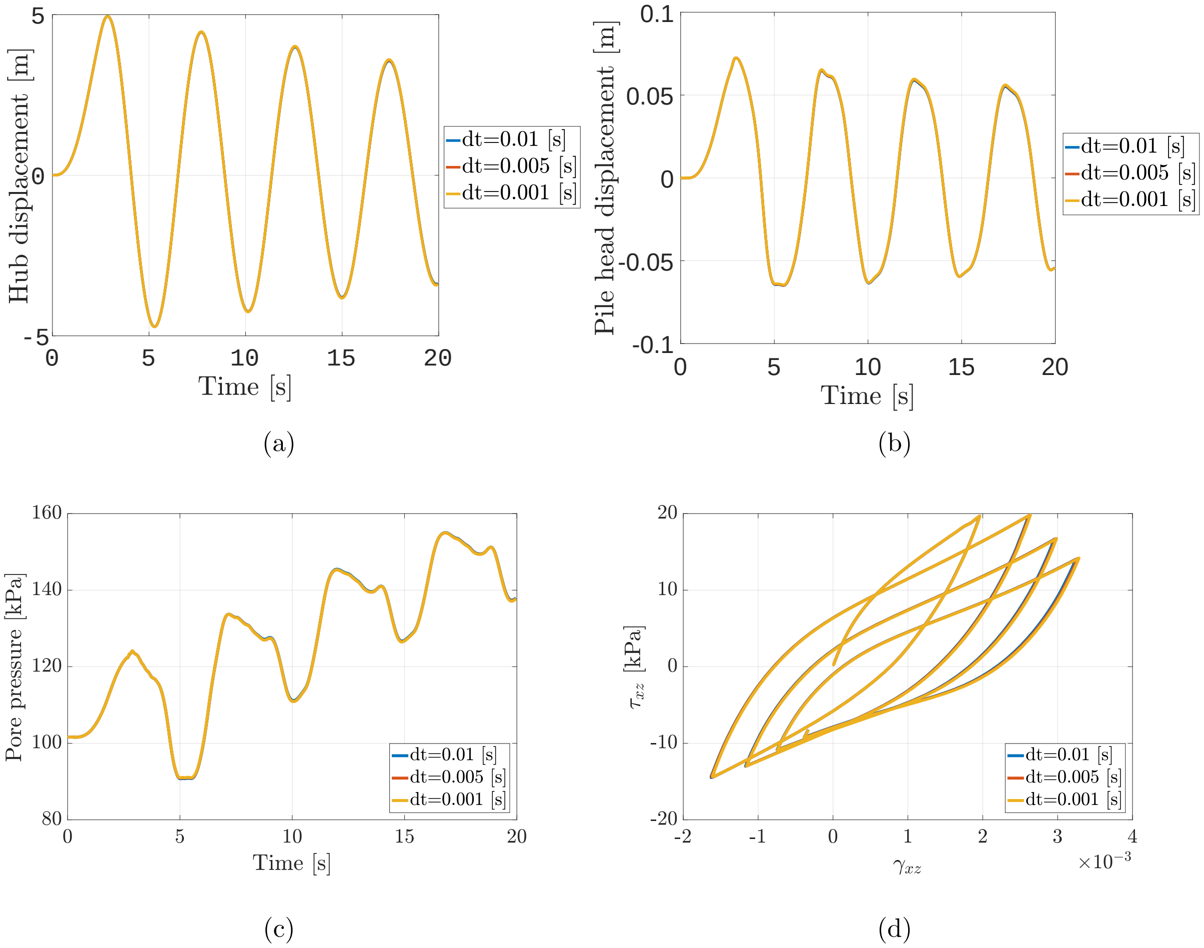

Figure 35: Timestep sensitivity analysis: (a) Hub displacement time history, (b) pile head displacement time history, (c) pore pressure time history and (d) $\tau_{xz} - \gamma_{xz}$ at control point located just north of control point A, (Figure 29).

In order to conclude then the natural frequency of the system, the lateral and rotational foundation flexibility coefficients must be estimated.

$$C_R = 1 - \frac{1}{1 + \alpha\left(\eta_R - \frac{\eta_{LR}^2}{\eta_L}\right)} \tag{12}$$

$$C_L = 1 - \frac{1}{1 + b\left(\eta_L - \frac{\eta_{LR}^2}{\eta_R}\right)} \tag{13}$$

where,

$$\eta_L = \frac{K_L L_T^3}{EI_\eta} \qquad \eta_{LR} = \frac{K_{LR} L_T^2}{EI_\eta} \qquad \eta_R = \frac{K_R L_T}{EI_\eta} \tag{14}$$

K_L, K_R, K_{LR} are the stiffness parameters that come as an input from (Shadlou and Bhattacharya, 2016), $L_T = 85m$ is the tower length and EI_η is the equivalent bending stiffness of the tower calculated as:

$$EI_\eta = E_T I_T f(q) = 1.27 \times 10^3 [GPa] \tag{15}$$

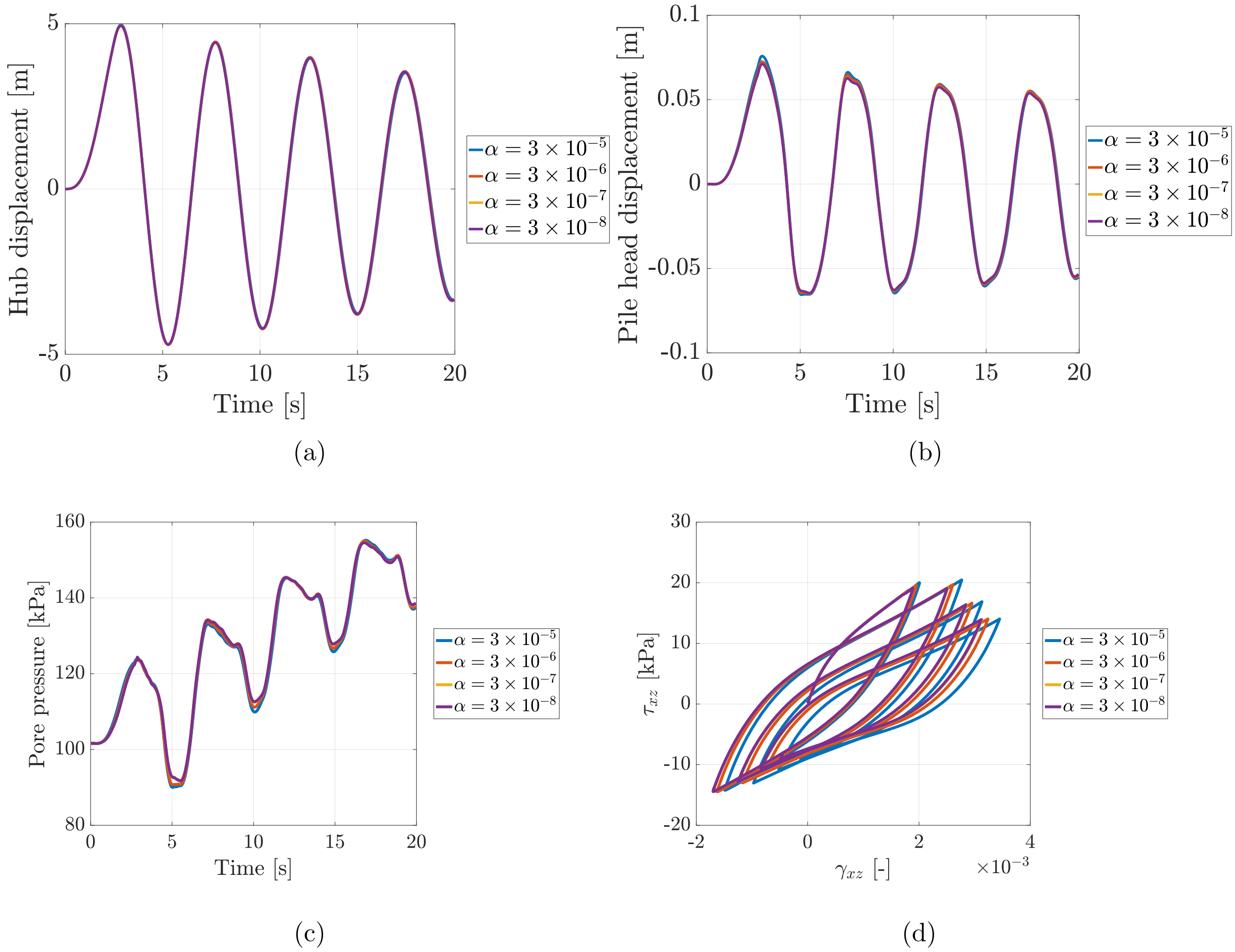

Figure 36: Stabilization parameter α discretization sensitivity analysis: (a) Hub displacement time history, (b) pile head displacement time history, (c) pore pressure time history and (d) $\tau_{xz} - \gamma_{xz}$ at control point located just north of control point A, (Figure 29).

with

$$E_T = 210GPa \quad I_T = 1.7[m^4] \quad q = \frac{D_b}{D_t} = 1.63 \tag{16}$$

$$f(q) = \frac{1}{3} \times \frac{2q^2(q-1)^3}{2q^2lnq - 3q^2 + 4q - 1} = 2.32 \tag{17}$$

with D_b=6.5m being the diameter at the base of the tower and D_t=4m the diameter at the tower top. The contribution of the foundation stiffness remains and according to (Shadlou and Bhattacharya, 2016), for rigid monopiles in homogeneous soil the stiffness is calculated as:

$$K_L = \frac{1.45E_{S0}D_p}{f_{vs}}\left(\frac{E_{eq}}{E_{S0}}\right)^{0.186} \quad K_{LR} = -\frac{0.3E_{S0}D_p^2}{f_{vs}}\left(\frac{E_{eq}}{E_{S0}}\right)^{0.5} \quad K_R = \frac{0.18E_{S0}D_p^3}{f_{vs}}\left(\frac{E_{eq}}{E_{S0}}\right)^{0.73} \tag{18}$$

$$E_{eq} = \frac{64E_pI_p}{D_p^4\pi} = 12.6[GPa] \tag{19}$$

L_p=27m is the monopile length, D_p=8m is the pile diameter, $I_p = 12[m^4]$ is the cross-sectional moment of inertia, E_{S0} is the soil stiffness at 1 D_p below the mudline and $f_{vs} = 1+|v-0.25| = 1.05$, is a formulation that includes the effect of soil's Poisson ratio on the calculated stiffness. The soil stiffness was described via the small strain stiffness. By using the SaniSand 2004 model, the small strain stiffness results from:

$$G(e,p) = G_0 p_{at} \frac{(2.97-e)^2}{1+e}\left(\frac{p}{p_{at}}\right)^{0.5} \quad E_{S0} = 2G(e, p_{(z=D_p)})(1+v) \tag{20}$$

where p_{at} is the atmospheric pressure used for normalization, G_0 is a constant, e is the sand void ratio and p is the mean effective confinement stress at the considered location, here at $1D_p$. The small strain stiffness for the different void ratios can be seen in 5. For the case of Dr=80% these result in:

$$K_L = 2.06[GN/m] \quad K_{LR} = -17.32[GN] \quad K_R = 273.5[GN/rad] \tag{21}$$

so,

$$\eta_L = 1950 \qquad \eta_{LR} = -178 \qquad \eta_R = 30.6 \tag{22}$$

$$C_R = 0.877 \qquad C_L = 0.998 \tag{23}$$

and

$$f_0 = 0.877 \times 0.998 \times f_{FB} = 0.191Hz \tag{24}$$

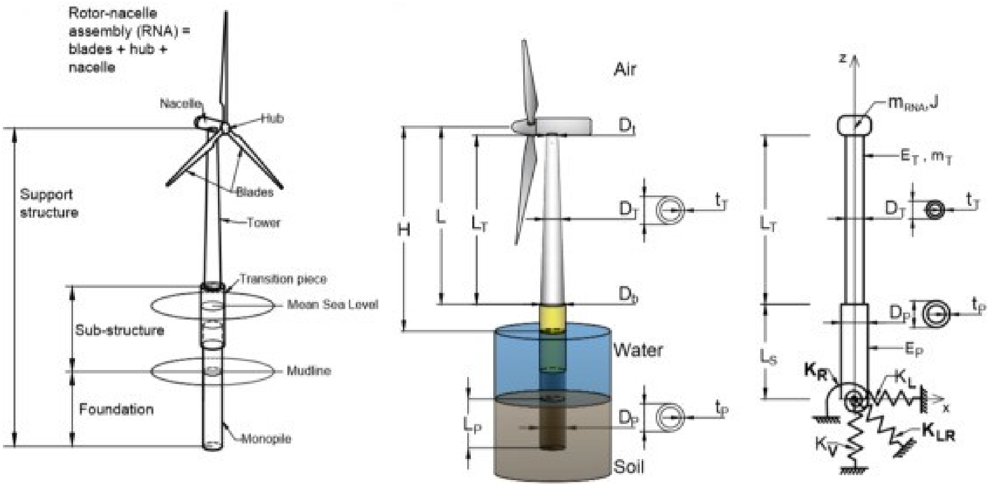

Figure 37: Basic model of an OWT depicting main components (left), dimensions (middle) and the mathematical model (right), (Arany et al., 2016).

A.6 Void ratio effects for Case A

As discussed before, the SaniSand2004 model by accounting the critical state theory of soils, allows the simulation of sands behaviour over a range of stresses and relative densities. That said, it is of interest to track changes on relative density so that changes in soil behaviour can be attributed to eventual evolution of the state of the soil. Changes in relative density over time for *Case A* can be seen in (Figures 38, 39, 40). As it can be seen, introducing the structure even with the wished-in place approach, affects the void ratio of the sand. As expected at control points located at the same depth at mirror distance from the monopile center, the void ratio is the same, as the effect of installation is symmetric along the z axis (Figure 7). Void ratio changes are slightly more pronounced at $A_{L,R}$ control points which are closer to the mudline. Overall void ratio does not seem to be drastically affected in the time analysed, as probably the permeability of $k = 10^{-5} m/s$ does not allow for consolidation and thus changes in volume over such a short period. This implies that the turbine response over a short storm would be dominated more from pore pressure evolutions than changes in the state of sands.

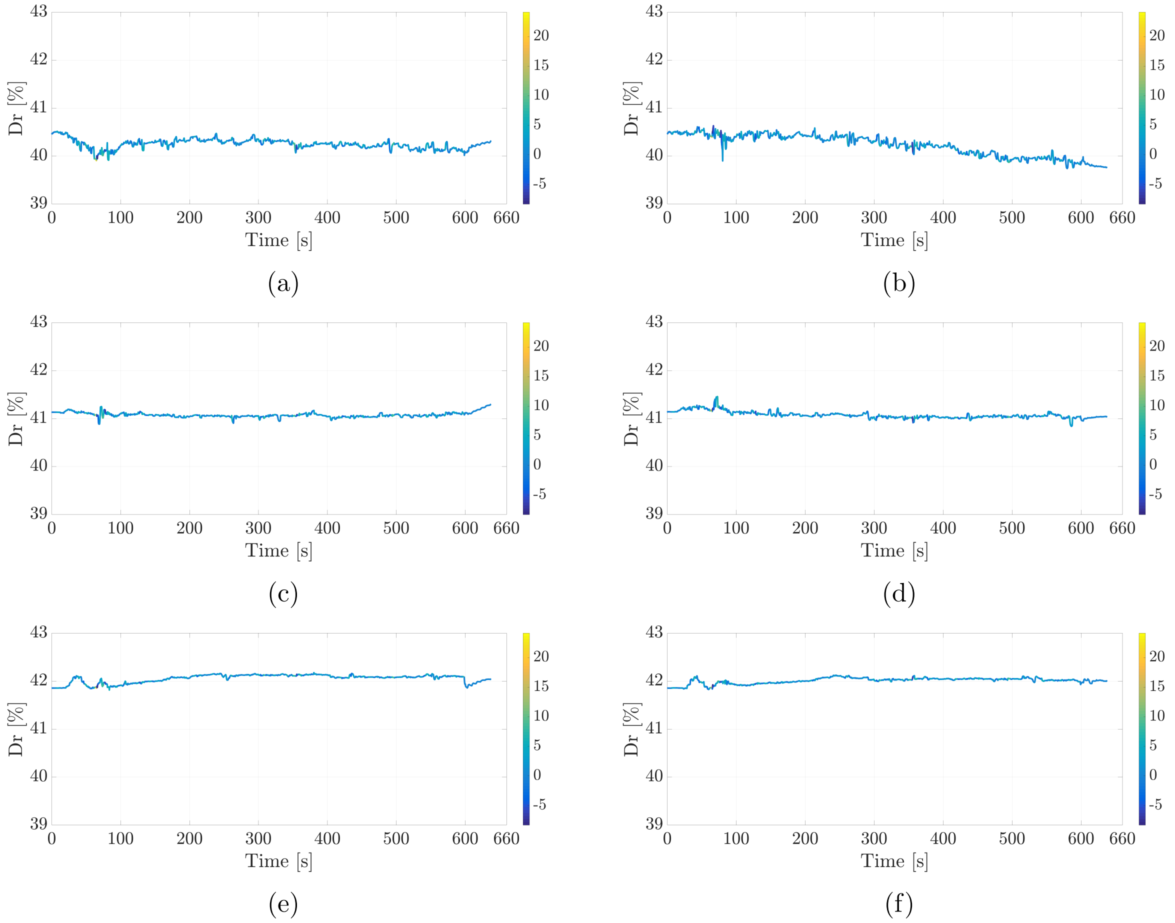

Figure 38: Relative density over time for all control points, Dr=40% : (a) A_L, (b) A_R, (c)B_L, (d) B_R, (e)C_L, (f) C_R. The colorbars indicate acting force.

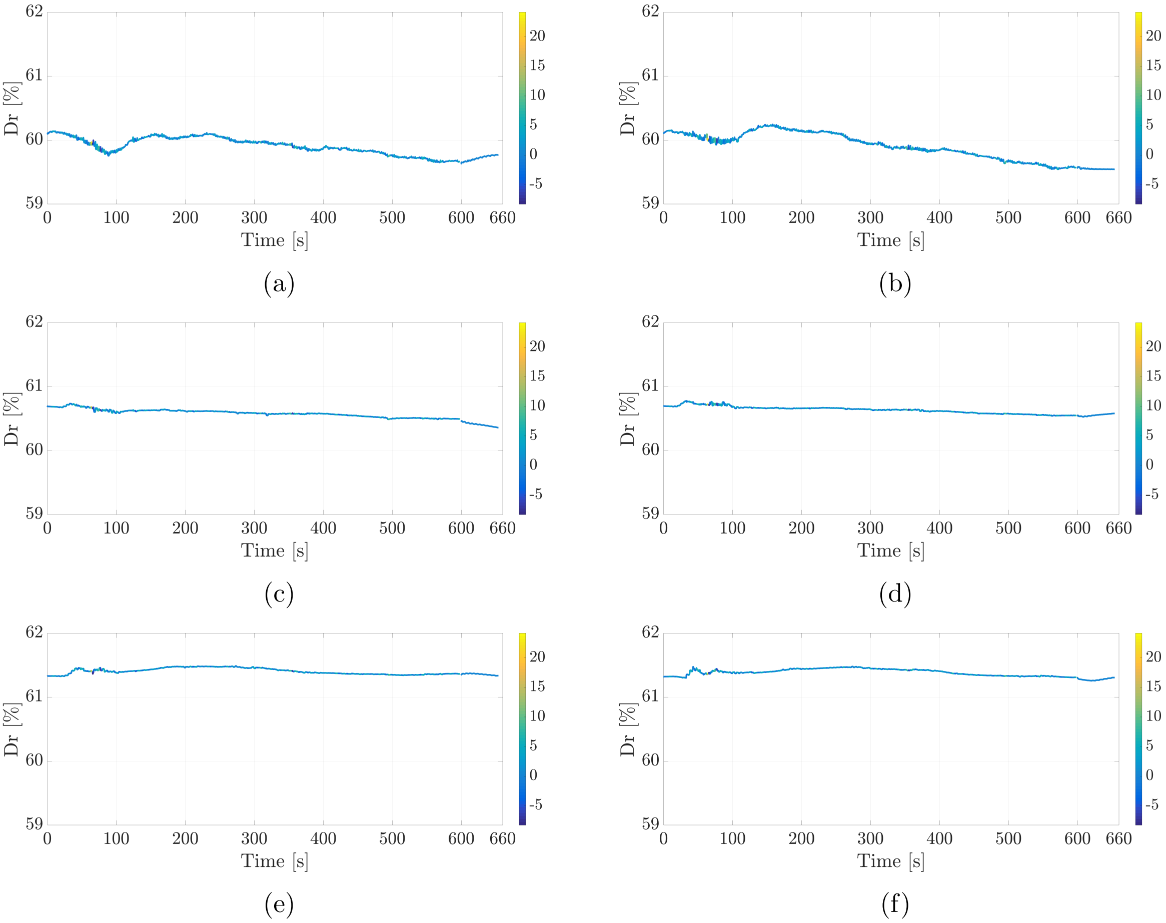

Figure 39: Relative density over time for all control points, Dr=60% : (a) A_L, (b) A_R, (c)B_L, (d) B_R, (e)C_L, (f) C_R. The colorbars indicate acting force.

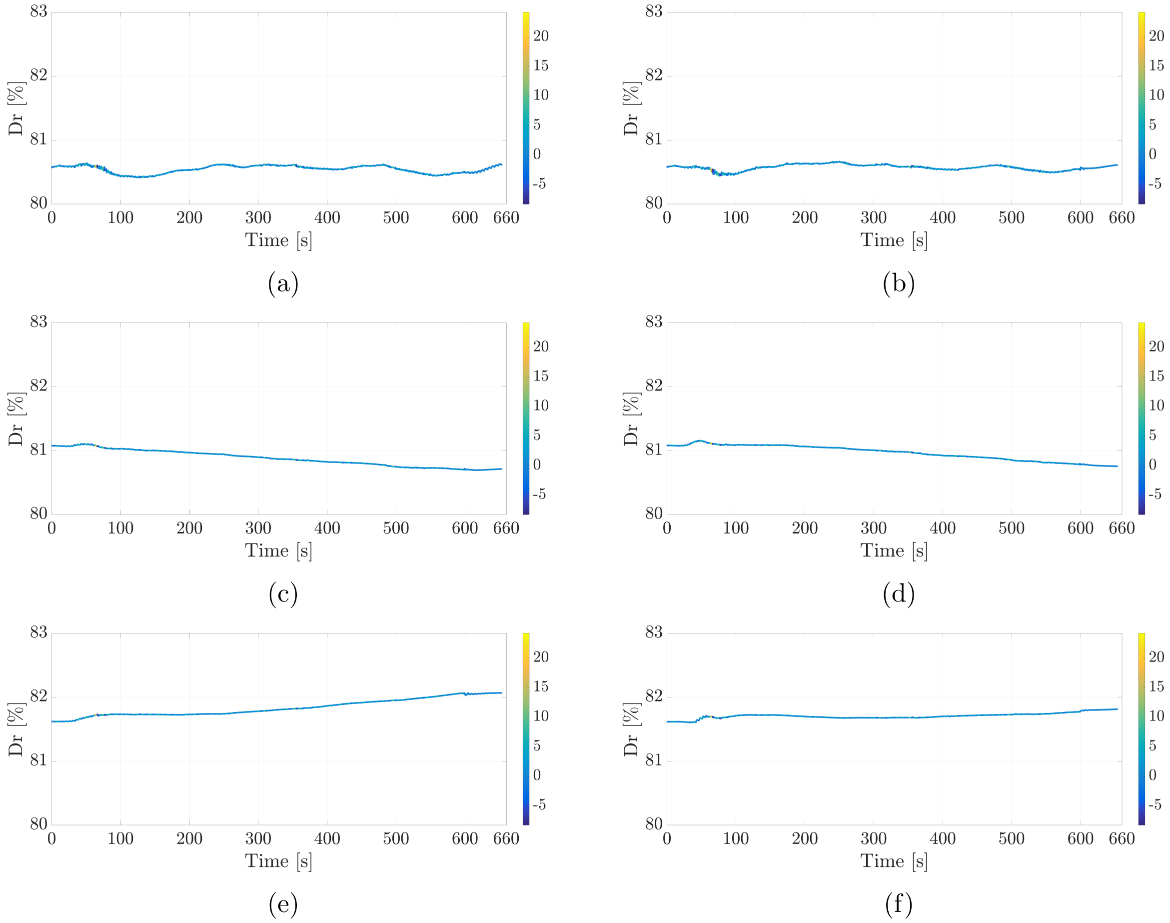

Figure 40: Relative density over time for all control points, Dr=80% : (a) A_L, (b) A_R, (c)B_L, (d) B_R, (e)C_L, (f) C_R. The colorbars indicate acting force.

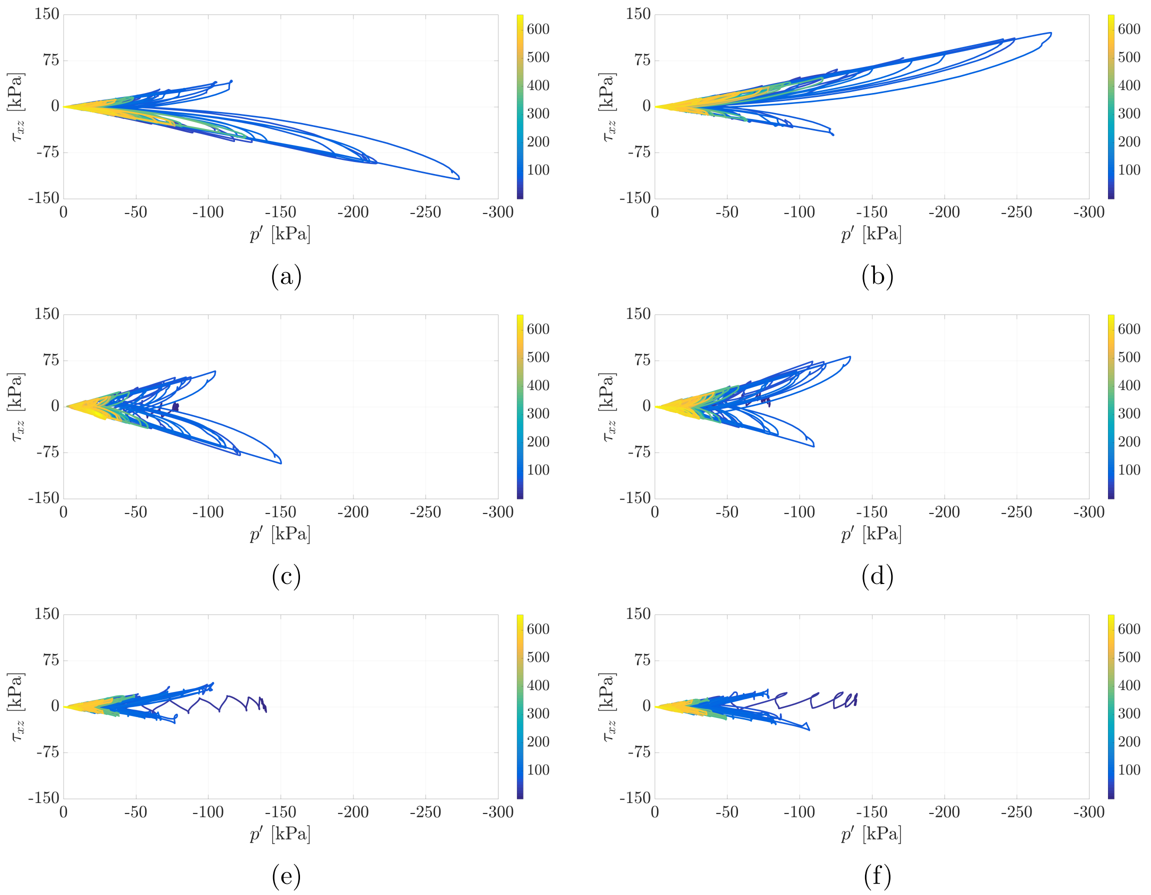

Figure 41: Stress paths of $\tau_{xz} - p'$ for all control points, Dr=60% : (a) A_L, (b) A_R, (c)B_L, (d) B_R, (e)C_L, (f) C_R. The colorbars indicate time.

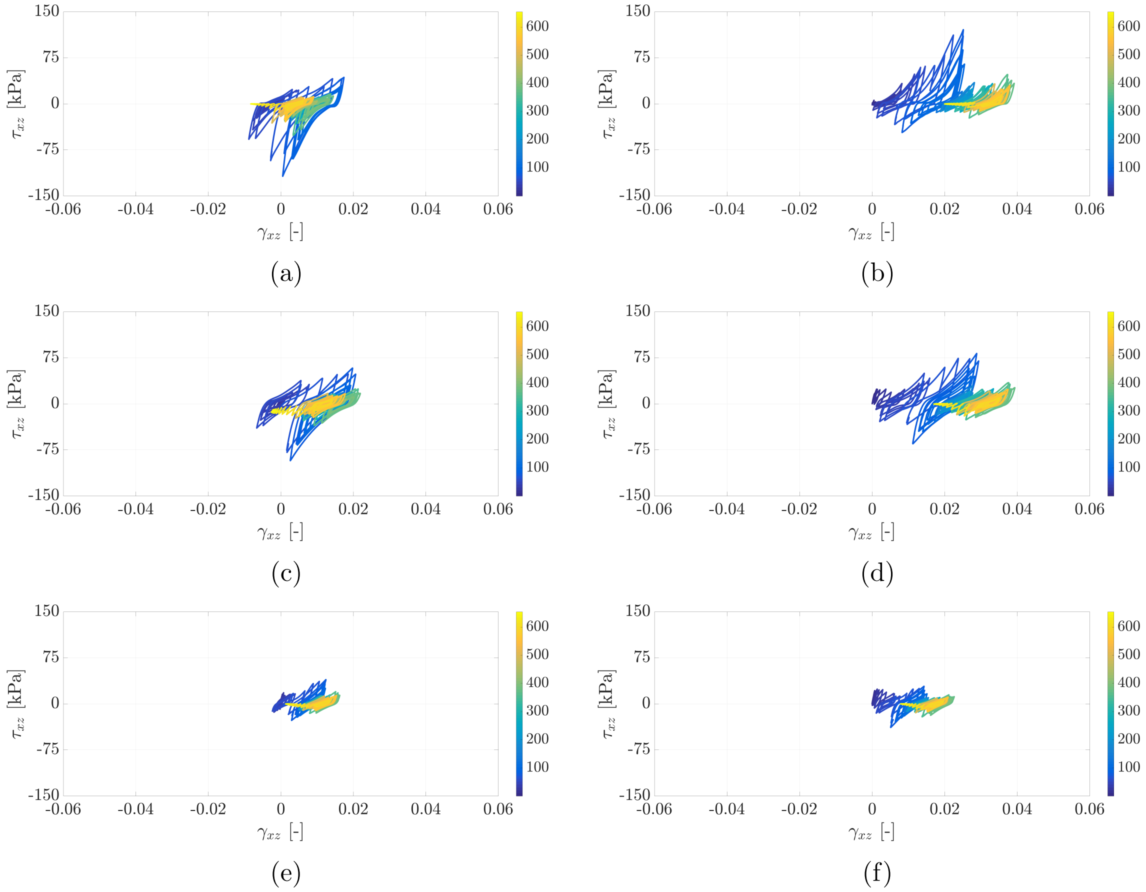

Figure 42: Stress-strain $\tau_{xz} - \gamma_{xz}$ for all control points, Dr=60% : (a) A_L, (b) A_R, (c)B_L, (d) B_R, (e)C_L, (f) C_R. The colorbars indicate time.